The Morphology and Equilibration of Levitated Secondary Organic Particles Under Controlled Conditions

Submitted in partial fulfillment of the requirements for

the degree of

Doctor of Philosophy

in

Environmental Management and Science

Kyle J. Gorkowski

B.S., Physics, Michigan Technological University
M.S., Civil and Environmental Engineering, Carnegie Mellon University

Carnegie Mellon University
Pittsburgh, Pennsylvania, USA
September, 2017

Dedicated to my Mom and Dad.

Acknowledgements

Being at the Center for Atmospheric Particle Studies in Carnegie Mellon University has been a great experience for me. I would like to thank my undergraduate advisor Claudio Mazzoleni for starting me down the path of atmospheric aerosols at Michigan Technological University. Claudio also introduced me to Manvendra Dubey who I had the pleasure of working with at Los Alamos National Laboratory along with Bradly Flowers, Allison Aiken, Ben Klein, and Curt Dvonch. My time at Los Alamos was an invaluable experience where I learned a substantial amount of research skills.

Ryan Sullivan and Neil Donahue have been very supportive advisors during my time spent at CMU. I am grateful for the for the opportunity I had to work with them and will continue to follow their research with great interest. I have benefited from their experience and I am a better scientist because of their guidance.

I would like to thank my thesis committee composed of Peter Adams, Greg Lowry, Neil Donahue and Ryan Sullivan. Your astute questions and feedback on my proposed research and results presented here have been invaluable. I would like to thank Neil and Ryan for being my committee co-chairs.

This research was funded by the National Science Foundation through the continued support of the American Taxpayer (National Science Foundation Award Number CHE-1213718 & CHE-1554941). I am thankful for the Dean's Fellowship from the College of Engineering that supported the first year of my PhD. I also thankful for the

support of John and Claire Bertucci for their generous Fellowship that supported part of my PhD.

I would also like to thank my long-distance collaborators from the University of Bristol Jim Walker and Jonathan Reid. Your thoughtful guidance in the early stages of the research have help shape the resulting thesis for the better.

The Center for Atmospheric Particles Studies (CAPS) is one of the best collaborative spaces I have been a part of. The high quality and diverse research makes this community truly special. The other principle investigators and scientists in CAPS (Albert Presto, Satbir Singh, Allen Robinson, Peter Adams, Spyros Pandis, Eric Lipsky, Rawad Saleh, and R. Subramanian) helped broaden my interests and shape my research questions. When I started at CAPS the startup office was my home, and a great home it was. The open and collaborative nature of the startup office is a reflection of CAPS in general. I would like to thank everyone that has come into the startup office and hallway outside it to discuss research and life, especially Nasser, Pablo, Xiang, Marguerite, Shayak, Ningxin, Yunliang, Andrew, Victoria, and Elina.

Ellis and Rawad have been with me since the beginning and I cannot thank them enough for their well-reasoned opinions and discussion. Hassan and Adam you are impeccable people and it was a pleasure to work with you. Hassan, you and I shared in the ups and the downs of the optical tweezers and I wish you all the best. Michael and Leif thank you for your thoughtful couch discussions and your chemical expertise. Thank you to the rest of the startup office occupants (Lydia, Meredith, Bob, and Xiang) who put up with the lively discussions that meant you could not do much work. For the times when it was not a useful discussion then blame Tom. Thank you, Tom for contributing to the startup office distractions it has been a lot fun and I doubt I will find another desk neighbor and friend like you.

Qing and Georges thank you for talking about your research and listening to my ramblings as I try to square your results with mine. It was always a pleasure to hear about similar aerosol studies, tackled using a few more particles than I do. Thank you to the daily lunch group (Wayne, Tom, Hugh, Rishabh, and Dip) for your non-scientific discussions and candor. CAPS is a great community and could never be replaced.

Lastly, I would not be here without the love and support of my parents and siblings, who taught me the skills to weather any storm. Only through your implicit support was I able to take these giant leaps without the fear of utter ruin.

Abstract

I advanced the understanding of particle morphology and its implications for the behavior and effects of atmospheric aerosol particles. I have developed new experimental methods for the Aerosol Optical Tweezers (AOT) system and expanded the AOT's application into studying realistic secondary organic aerosol (SOA) particle phases. The AOT is a highly accurate system developed to study individual particles in real-time for prolonged periods of time. While previous AOT studies have focused on binary or ternary chemical systems, I have investigated complex SOA, and how they interact with other chemical phases, and the surrounding gas-phase. This work has led to new insights into liquid-liquid phase separation and the resulting particle morphology, the surface tension, solubility, and volatility of SOA, and diffusion coefficients of SOA phases.

I designed a new aerosol optical tweezers chamber for delivering a uniformly mixed aerosol flow to the trapped droplet's position. I used this chamber to determine the phase-separation morphology and resulting properties of complex mixed droplets. A series of experiments using simple compounds are presented to establish my ability to use the cavity enhanced Raman spectra to distinguish between homogenous single-phase, and phase-separated core-shell or partially-engulfed morphologies.

I have developed a new algorithm for the analysis of whispering gallery modes (WGMs) present in the cavity enhanced Raman spectra retrieved from droplets trapped in the AOT. My algorithm improves the computational scaling when analyzing core-shell droplets (i.e. phase-separated or biphasic droplets) in the AOT, making it computationally practical to analyze spectra collected over many hours at a few Hz.

I then demonstrate for the first time the capture and analysis of SOA on a droplet suspended in an AOT. I examined three initial chemical systems of aqueous NaCl, aqueous glycerol, and squalane at ~ 75% relative humidity. For each system I added α-pinene SOA – generated directly in the AOT chamber – to the trapped droplet. The resulting morphology was always observed to be a core of the initial droplet surrounded by a shell of the added SOA. By combining my AOT observations of particle morphology with results from SOA smog chamber experiments, I conclude that the α-pinene SOA shell creates no major diffusion limitations for water, glycerol, and squalane under humid conditions.

My AOT experiments highlight the prominence of phase-separated core-shell morphologies for secondary organic aerosols interacting with a range of other chemical phases. The unique analytical capabilities of the aerosol optical tweezers provide a new approach for advancing the understanding of the chemical and physical evolution of complex atmospheric particulate matter, and the important environmental impacts of aerosols on atmospheric chemistry, air quality, human health, and climate change.

Table of Contents

List of Figures

1 Introduction

Atmospheric aerosols play an important role in Earth's climate system and are linked to adverse health effects[1,2]. Aerosols are a complex mixture of organic carbon, elemental carbon, and inorganic, metallic, and mineral components, all mixed with a variable amount of water[3,4]. Organic aerosols arise from direct emissions of primary organic aerosol (POA) and from oxidation of precursors – volatile organic compounds and evaporated POA – that generates less-volatile secondary organic aerosol (SOA)[5,6]. Complex SOA is a major component of atmospheric organic aerosol, constituting between 30-70% of the total aerosol mass[6,7]. It is composed of thousands of individual organic compounds[8–10].

One key property that often impedes thorough experimental or ambient investigations of organic aerosols is the presence of distinct thermodynamic phases in a particle, and the particle's resulting morphological state (or internal structure) in complex multicomponent aerosols[11–33]. Liquid particles are common under atmospheric conditions and they can adopt three main types of particle morphologies[21,27–30,30,34–45]. These can be broadly categorized as a homogeneous mixed single-phase structures, and two heterogeneous or liquid-liquid phase separated (LLPS) structures[40,42,46]. For a phase-separated particle, the two predominant morphological states are a core-shell or partially-engulfed arrangement of the two phases[36,46–48].

In experiments addressing the formation or properties of organic aerosol, if the compounds are not observed to or are expected not to mix then they are usually assumed to adopt a core-shell morphology where one phase "coats" the other[9,49–51]. The occurrence and importance of partial-shell morphologies to the timescales of physical and chemical evolution of aerosols has recently come to the forefront[44,47,48,52–56]. For a core-shell morphology the diffusion through the shell dictates the rate at which gas-phase components partition into similar aerosol components as the system re-equilibrates[50,51,57,58]. The self-diffusion coefficients though secondary organic aerosol matter have been estimated to be up to 7 orders of magnitude smaller than through pure liquids[50,51,59,60]. This mass-transfer limitation could lead to a retardation of the kinetics of water equilibration with the gas phase environment[60,61]. Thus the particle's morphology after liquid-liquid phase separation would play an important role in determining the future evolution of the aerosol, its environmental interactions and effects, and its lifetime[62].

The composition at the air-particle interface also dictates the particle's ability to undergo chemical reactions with gas-phase reactants, and the rates and mechanisms of those reactions[59,63–65]. The importance of the air-particle interface is demonstrated through the reactive uptake coefficient of $\gamma(N_2O_5)$, which acts to remove N_2O_5 from the atmosphere at night. The reactive uptake is highly dependent on the water content at the particle surface; $\gamma(N_2O_5)$ has a reported range of 0.015 to 0.2[66–77]. So, if a particle has an aqueous core and a hydrophobic shell, this will reduce the efficiency of the uptake reaction[14,70]. Reactive uptake can also be a mechanism to increase aerosol mass loadings, as is the case with isoprene SOA[6,78–90]. When an isoprene-derived epoxydiol encounters a particle surface, the epoxide ring-opening reaction can be promoted by the presence of water and an acid or nucleophile. These hydrolysis reactions drive the epoxydiol to the aerosol phase, increasing the aerosol mass burden[78,91,92]. This uptake efficiency is dependent on the particle surface composition and the availability of water, so if there is phase separation, that needs to be accounted for[91,93,94]. It may also be self-limiting; epoxydiol hydrolysis products can be surface-active and salted out to the surface, and thus impede the heterogeneous hydrolysis of further isoprene oxidation products.

The Raoult effect does enhance SOA yields when compared to inert SOA seeds[9,95–97]. Ye et al.[97] showed that the Hansen solubility framework could inform the miscibility of α-pinene SOA onto pure component seeds. The general result from their mixing experiments is that highly polar and nonpolar phases do not mix with α-pinene SOA, while α-pinene SOA does dissolve into phases of intermediate or mixed polarity. The techniques used in smog chamber experiments can infer phase separation from changes in the aerosol mass yield, aerosol size distribution, or the mixing state of components measured using single-particle analysis. However, smog chamber experiments cannot determine the critical information regarding the resulting particle morphology. For a core-shell morphology, diffusion through the shell could dictate the equilibration rates of molecules partitioning into or out of the particle-phase[50,51,57,58,98]. This shell effect would not be present in a partially-engulfed morphology.

The morphology of liquid-liquid phase separated particles representing typical atmospheric aerosol components has been studied using optical microscopy, aerosol optical tweezers, Raman spectroscopy, scanning electron microscopy, cryo-transmission electron microscopy, and aerosol mass spectrometry[29,30,32,37,41,42,45–48,53,54,99]. The direct observational studies rely on microscopy where particles are placed on a hydrophobic substrate, which may affect the resulting morphology[39,41,42]. An issue arises from the fact that a core-shell morphology is not a unique solution to the observed 2-D image under the microscope; a partially-engulfed structure may appear as core-shell through optical microscopy.

Studying individual suspended particles allows us to observe the dynamics of aerosol chemistry while trapping and observing the evolution of the same individual particle sample. In the AOT, aerosol properties are tracked in real time and can be compared to any previous time point to understand how perturbations to the particle's composition or surrounding gas-phase environment in turn change the particle's properties.

1.1 Methods of Particle Levitation

1.1.1 Aerosol Optical Tweezers

The AOT utilizes radiation pressure exerted by photons of light to suspend and trap a droplet in 3-dimensions. This traditional AOT setup uses a single Gaussian laser beam passing through the back aperture of a 100x microscope objective, above which the optical trap is formed[100]. Other types of optical traps can study absorbing particles (e.g. a hollow beam trap), and the Bessel beam trap can probe submicron particles[57,101,102]. In a traditional AOT droplets typically range from 4 to 14 microns in diameter. The main measurement recorded is the Raman spectrum, which is induced by the trapping laser and collected from the droplet using the same microscope objective. In the AOT the data collection optics and the trapping optics are one in the same. At discrete wavelengths, whispering gallery modes (WGMs) form in the droplet as it acts a high finesse optical cavity where the WGMs form a standing wave on the droplet surface[103–105]. The WGMs are then superimposed on top of the broader Stokes shifted vibrational modes in the droplet's Raman spectrum. These WGMs positions are then fitted to a homogeneous Mie scattering model to retrieve the droplet's diameter, d_{p}, and refractive index, n[106,107]. The diameter (d_p) can be determined to an accuracy of ±0.05% and the refractive index (n) to ±0.11%[106,107]. Recent work has extended the WGM analysis to liquid-liquid phase separated droplets utilizing a core-shell Mie scattering model[108,109].

The WGMs can be used to distinguish between the three predominant morphologies: phase-separated core-shell or partial-engulfed structures, and homogeneous single-phase droplets[44,48,52,110]. Furthermore any changes in the droplet morphology as composition or environment surrounding changed are directly assessed[111,112]. The AOT can also study SOA collected onto an individual micron sized probe droplet and does not require the SOA to first be collected on a substrate, and then extracted in solvent as is the case with other methods[113–115].

This AOT method and subsequent analysis has been used in detailed studies of aerosol thermodynamics and kinetics of surrogates of atmospheric aerosol by tracking the size and composition in real-time with high accuracy[111,116–120]. Precise assessment of diffusion coefficients and equilibration timescales of water in vicious mediums has helped probe the applicability of the classic Einstein-Stokes relation for diffusion and viscosity for glassy aerosols[121].

1.1.2 Electrodynamic Balance and Acoustic Levitation

The electrodynamic balance (EDB) uses charged particles and balances the particle in an electric field achieving a stable trap. This stable trap requires a feedback loop between the electrodes and the particle's position, as the droplet position is sensitive to changes in its mass. The droplets studied in the EDB are typically greater than 10 microns in diameter. The EDB can be combined with a Raman spectrograph to attain WGMs similar to the AOT setup, provided they are of a small size (10-20 microns)[122]. Unlike the traditional AOT, crystalline droplets are reliably trapped making the EDB ideal for phase transition experiments such as salt efflorescence and the freezing of water[123,124].

Acoustic levitation utilizes the pressure of ultrasonic waves to trap a single particle in the nodes of a standing sound wave. This trap relies on air pressure and as such the trapping is limited to larger particles that are on the order of millimeters in diameter[125]. Due to the smaller droplet sizes and existing analysis frame work the AOT was my preferred system for subsequent experimental investigations.

1.2 Thesis overview

I present new experimental and data analysis methods for the AOT. In Chapter 2 I present my work designing a new AOT chamber to facilitate trapping and stable coagulation of additional material to a tweezed droplet. This chapter provides a background to liquid-liquid phase separation and how surface tension plays the key role in the resulting morphology. Chapter 2 then presents experiments on pure compounds showing the possible morphologies I would likely observe with SOA. Chapter 2 was published in *Aerosol Science & Technology*[108].

In Chapter 3 I present my advances in the inverse problem of fitting WGM positions to a droplet's diameter and refractive index. Using these insights, I developed a new algorithm that was needed to fit WGMs from a core-shell droplet. My algorithm improves the computational scaling when analyzing core-shell droplets (i.e. phase-separated or biphasic droplets) in the AOT, making it computationally practical to analyze spectra collected over many hours at a few Hz. This chapter is in preparation for submission.

In Chapter 4 I used the new core-shell fitting algorithm and the new AOT chamber to add *in situ* generated α-pinene SOA to a trapped droplet. This was done at ~75% humidity for an aqueous NaCl, aqueous glycerol and squalane droplet. In all cases I observed a core-shell morphology with α-pinene SOA as the shell. I found that the SOA shell did not limit the diffusion of species between the core and the surrounding gas phase. This chapter is currently under review in *Environmental Science & Technology*.

In Chapter 5 I present work on the morphologies of SOA at low relative humidities (~12% RH). This chapter focuses on the viscosity and surface tension properties of α-pinene SOA. I discuss the possible atmospheric morphologies using the bounds I determined for the surface tension of SOA, a key property that is difficult to determine using other techniques. In this chapter I also present evidence for a RH dependent phase-separation for glycerol with α-pinene SOA. This chapter is in preparation for submission.

In Chapter 6 I conclude summarizing the major points of this thesis and discuss future work in this area. I discuss new SOA systems to study in the AOT as well as the results I could expect. For example, isoprene SOA has a high O:C which would mean homogeneous morphology but its products are also surface active leading to core-shell morphology.

2 Advanced Aerosol Optical Tweezers Chamber Design to Facilitate Phase-Separation and Equilibration Timescale Experiments on Complex Droplets

This is an Accepted Manuscript of an article published by Taylor & Francis Group in Aerosol Science and Technology 08/15/2016, available online at http://www.tandfonline.com/doi/full/10.1080/02786826.2016.1224317

Gorkowski, K., Beydoun, H., Aboff, M., Walker, J. S., Reid, J. P. and Sullivan, R. C.: Advanced aerosol optical tweezers chamber design to facilitate phase-separation and equilibration timescale experiments on complex droplets, Aerosol Sci. Technol., 50(12), 1327–1341, doi:10.1080/02786826.2016.1224317, 2016. Copyright 2016

2.1 Abstract

The phase-separation of mixed aerosol particles and the resulting morphology plays an important role in determining the interactions of liquid aerosols with their gas-phase environment. I present the application of a new aerosol optical tweezers chamber for delivering a uniformly mixed aerosol flow to the trapped droplet's position for performing experiments that determine the phase-separation and resulting properties of complex mixed droplets. This facilitates stable trapping when adding additional phases through aerosol coagulation, and reproducible measurements of the droplet's equilibration timescale. I demonstrate the trapping of pure organic carbon droplets, which allows us to study the morphology of droplets containing pure hydrocarbon phases to which a second phase is added by coagulation. A series of experiments using

simple compounds are presented to establish my ability to use the cavity enhanced Raman spectra to distinguish between homogenous single-phase, and phase-separated core-shell or partially-engulfed morphologies. The core-shell morphology is distinguished by the pattern of the whispering gallery modes (WGMs) in the Raman spectra where the WGMs are influenced by refraction through both phases. A core-shell optimization algorithm was developed to provide a more accurate and detailed analysis of the WGMs than is possible using the homogenous Mie scattering solution. The unique analytical capabilities of the aerosol optical tweezers provide a new approach for advancing my understanding of the chemical and physical evolution of complex atmospheric particulate matter, and the important environmental impacts of aerosols on atmospheric chemistry, air quality, human health, and climate change.

2.2 Introduction

Atmospheric aerosols play an important role in Earth's climate system and are linked to adverse health effects[1,2]. Organic carbon-based aerosol particles are a major component of ambient aerosol and can make up between 30-70% of the total fine aerosol mass[6,7,126,127]. Thus it is important to understand the chemical processes that generate or modify organic aerosols, and their key physicochemical properties[61,62]. One key property that often impedes thorough experimental or ambient investigations of organic aerosols is the presence of distinct thermodynamic chemical phases in a particle, and the particle's resulting morphological state (or internal structure) in complex multicomponent aerosols[11–13,20,29–31,128]. Liquid particles are common under atmospheric conditions with three main types of particle morphology[21,27,29,34,37–39,43,109,129]. These can be broadly categorized as a homogeneously mixed single-phase structure, and liquid-liquid phase-separated (LLPS) structures[40,42,46,54,55,109]. For the phase-separated particles, the predominant morphological states are a core-shell or partially-engulfed structure[36,46–48].

A phase-separated morphology is important in experiments addressing the formation or properties of oxidized secondary organic aerosol (SOA) mixed with a hydrocarbon or aqueous phase. In the cases where the phases are not expected or observed to mix the resulting phase-separation is usually assumed to adopt a core-shell morphology where one phase "coats" the other[9,49–51]. The occurrence of partial-shell morphologies and their importance for the timescales of physical and chemical evolution of aerosols has recently come to the fore requiring novel analytical techniques to fully assess their occurrence and impacts[47,48,52–56,109]. For a core-shell morphology, diffusion through the shell dictates the rate at which gas-phase components partition into similar aerosol components as the system re-equilibrates[50,51,57,58]. The composition at the air-particle interface also dictates the particle's ability to undergo chemical reactions with gas-phase reactants, and the rates and mechanisms of those reactions[59,63–65,76].

The simplest type of phase separation occurs when a particle contains two immiscible components. An example would be oil and water in which the phase separation is easy to observe at the macroscale. To understand the resulting morphology of a suspended oil-water particle, the interfacial tensions ($\sigma_{phase\ A\,|\,phase\ B}$) between each of the three phases (oil, water, and air in this case) must be known[54]. In adopting an equilibrium structure, the total surface free energy is minimized; if the change in surface areas are small then I can simply use the spreading coefficients to directly predict the morphology. This assumption was shown to hold for systems studied using the aerosol optical tweezers, for example, oleic acid added to aqueous NaCl produced a partially-engulfed morphology[52,54]. For the 3-phase systems studied here, only the liquid spreading coefficients (S_{L1} and S_{L2}, Eqn. 2.1 and 2.2) are of interest as generally the spreading coefficient of the gas phase will be negative.

$$S_{L1} = \sigma_{L2|air} - \sigma_{L1|air} - \sigma_{L1|L2} \tag{2.1}$$

$$S_{L2} = \sigma_{L1|air} - \sigma_{L2|air} - \sigma_{L1|L2} \tag{2.2}$$

L_1 and L_2 are the two liquid phases. If both S_{L1} and S_{L2} are negative, then the particle adopts a partially-engulfed morphology, where the two phases lie side-by-side and in contact with each other at equilibrium. If either S_{L1} or S_{L2} is positive, then the particle exhibits a core-shell morphology and the phase with the positive spreading coefficient forms the shell. Note both S_{L1} and S_{L2} cannot be positive as then I get the impossible result of negative interfacial tension for $\sigma_{L1|L2}$. Aqueous phases always have a negative spreading coefficient, meaning it always costs energy to spread the aqueous phase over another phase. This is why the organic phase will always form the shell around the aqueous phase, if a LLPS core-shell morphology occurs. A partial-engulfing or homogeneous morphology is also possible for different combinations of aqueous and organic phases, depending on their miscibility and spreading coefficients.

The morphology of liquid-liquid phase-separated particles representing typical atmospheric aerosol components has been studied using optical microscopy, aerosol optical tweezers, confocal Raman spectroscopy, scanning electron microscopy, cryo-transmission electron microscopy, and aerosol mass spectrometry[29,30,32,37,41,42,46–48,53,54,99,109,129]. The direct observational studies rely on optical microscopy where particles are placed on a hydrophobic substrate, and this can affect the resulting morphology[39,41,42].

A major advantage of the aerosol optical tweezers (AOT) technique is that there are no surface contact points because the droplets are suspended in air by radiation pressure[130–132]. This contactless aspect of the AOT, combined with the surface resonant whispering gallery modes (WGMs) retrieved in the cavity enhanced Raman spectrum, provides a unique direct and real-time assessment of the droplet's morphology, size, and refractive index[106,107]. The WGMs can be used to distinguish between the three predominant morphologies: phase-separated core-shell or partial-engulfed structures, and homogeneous single-phase droplets[48,52,54,109,110]. Furthermore any changes in the droplet's morphology as its composition or the surrounding relative humidity are changed are directly assessed[111,112]. The AOT can also be used to study individual micron-sized droplets and does not require the aerosols to first be collected on a substrate, and then extracted in solvent as is the case with other methods[113–115].

2.3 Experimental Methods

2.3.1 Aerosol Optical Tweezers System

The AOT consists of three main components: the aerosol generation system, the droplet trapping system, and the trapping chamber. The design and evaluation of the new trapping chamber was the focus of my work presented here. The droplet trapping system is described in the supplement as I follow the same approach as Hopkins et al. (2004). Briefly, a 532 nm laser is passed through a set of expansion lenses so that the resulting beam overfills the back aperture the 100x (NA 1.25) oil immersion objective. The objective is pressed against the bottom of a thin glass coverslip, and an optical gradient force trap forms approximately 40 microns above the coverslip inside the trapping chamber.

The aerosol generation system creates droplets of sufficient size ($d_p > 4$ µm) and passes them into the chamber. A medical nebulizer (PARI TREK S) is used to generate aerosol from aqueous solutions that have low viscosity similar to water. To trap organic carbon based droplets the condensation monodisperse aerosol generator (CMAG; TSI, Inc.) is used for compounds that can grow droplets large enough by vapor condensation.

2.3.2 Chamber System Design

To apply the AOT system in studies of liquid-liquid phase separation, droplets composed of immiscible compounds must be trapped. I achieve this by adding the second phase to a tweezed droplet either by coagulation of small particles, or by vapor condensation. my chamber design goal was then to produce stable trapping under conditions of variable air flow rates, and during collisions of small droplets with the tweezed droplet.

When adding a second component to the trapped droplet through coagulation, the total flow field of conditioned air plus the additional aerosol flow should have the same uniform flow velocity as the conditioned air by itself. In this way the aerosol addition does not significantly affect the air flow around the droplet which can destabilize the trap. Condensation of vapors from the oxidation of gases is the second method that I designed for, which requires the ability to add organic aerosol vapor precursors to the conditioned air flow. The ability to add a second component by either condensation or coagulation will allow us to simulate the formation and chemical evolution of atmospheric aerosol particles mimics frequently studied using smog chamber or aerosol flow tube reactors[9,133–136], while allowing us to investigate the resulting morphology and properties of the individual multicomponent droplet. I used an iterative design process with computational fluid dynamic (CFD) simulations using Solidworks software, and rapid prototyping using 3D printing to optimize the final aluminum chamber design. The new chamber achieves a uniform and predictable fluid flow around the droplet's position that is an improvement over previous AOT chamber designs[113,115].

The AOT chamber must deliver the droplets reliably to the trapping region just above the coverslip, and establish the conditioned airflow that controls the relative humidity (RH) and vapor concentration surrounding the droplet. The trapped droplet only resides approximately 40 microns above the coverslip and lies within the surface boundary layer of the coverslip. The best chamber design I can achieve is to reliably and controllably deliver the droplets and the conditioned air to the boundary layer above the trapping location. I show the final design in Figure 2.1. It consists of three main sections: an upper mixing volume for conditioning the incoming air flow, a droplet trapping volume, and a vacuum volume for the exhaust air flow.

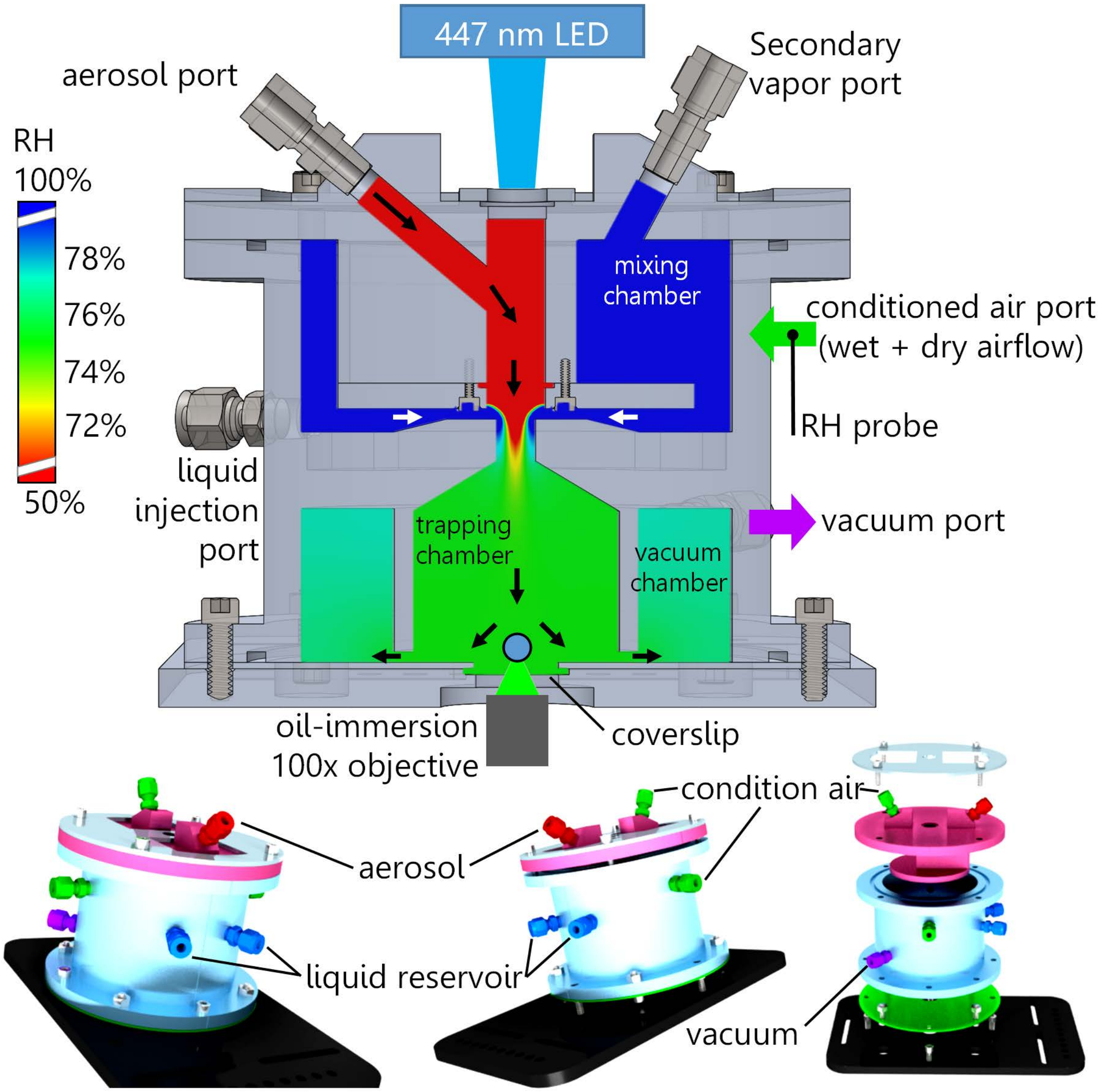

Figure 2.1. The interior design and external gas and aerosol ports of my aerosol optical tweezers chamber, designed in SolidWorks. The blue dot at the chamber bottom just above the coverslip represents the position of an oversized trapped droplet. The color scale displays the relative humidity field from computational fluid dynamics simulations of the humid conditioned airflow mixing with the drier aerosol airflow, in the chamber. The simulation shows the mixing of the various flows at the top of the trapping chamber. The mixing chamber flow is 0.15 L/min of 100% RH air and the vacuum exhaust flow is 0.3 L/min, resulting in 0.15 L/min coming in from ambient pressure at the aerosol port at 50% RH. The black and white arrows show the direction of the characteristic airflows. The lower images display three different rotations of the outer chamber design, with each machined part having a separate color.

The top of the chamber contains the mixing volume, where humidified and dry air are mixed to produce the RH conditioned air. This air flow can also be mixed with other gases injected into the mixing volume or with vapors evaporating from liquids contained in two wells at the bottom of the mixing chamber. The well-mixed air flow then travels radially inwards to the central shaft where the aerosol flow is also introduced, and the combined flow continues down into the trapping chamber. The radial introduction of the conditioned flow through a concentric slit surrounding the shaft is a key design feature I identified through CFD simulations for producing a uniform gas-phase flow before it reaches the droplet.

The expansion of the flow into the bottom trapping chamber slows its velocity while maintaining a central downward flow towards the trapping region. The result is a uniformly mixed downward airflow over the trapping region delivering conditioned air and droplets to the optical trap position under small fluid velocities (< 0.005 m/s, for 0.25 Lpm vacuum air flow and 0.35 Lpm conditioned air flow). After passing over the trapping region the gas flows out radially from the center trapping chamber to the surrounding vacuum chamber. The concentric exit slit surrounding the trapping region is important for maintaining a uniform gas-phase composition around the droplet because it produces uniform flow velocities and thus minimizes concentration gradients. These three chamber sections combine to generate a uniform airflow around the droplet, resulting in stable trapping during coagulation of additional aerosol particles to the trapped droplet, and a uniform gas-phase flow. I have stably trapped droplets in this system for more than 24 hours with no user intervention.

Control of the RH around the droplet is important for stable trapping of aqueous droplets, to perform hygroscopic growth and equilibration timescale experiments, and also for *in situ* production of secondary organic matter in future experiments through oxidation of precursor vapors directly in the chamber. Large variations in RH cause significant changes in the size of hygroscopic droplets, such that they are no longer stable in the optical trap and are lost. The desired RH is achieved using mass flow controllers whose flow rates are controlled via a custom LabVIEW program. Using a computer controlled RH system facilitates performing longer experiments over many hours to investigate hygroscopic growth and droplet equilibration timescales during RH cycles. Experiments can be replicated multiple times on the same droplet. Lastly, using the volumes of the mixing (0.38 L) and trapping (0.089 L) chambers I can calculate the theoretical equilibration timescale, τ, for changes in the gas phase using Eqn. 2.3.

$$\tau = \frac{0.38\ L}{conditioned\ airflow\ L/min} + \frac{0.089\ L}{vacuum\ airflow\ L/min} \tag{2.3}$$

τ is calculated as the sum of the residence times (volume/air flow rate) of the trapping and vacuum chambers. For a typical experiment this calculated timescale is 1.44 minutes (0.25 Lpm vacuum air flow and 0.35 Lpm conditioned air flow) and the shortest timescale I can achieve with this setup is 0.55 minutes (0.35 Lpm vacuum air flow and 1.25 Lpm conditioned air flow). Below I will compare this calculated timescale to the measured equilibration timescale by studying an aqueous salt droplet equilibrating to different step changes in RH.

2.3.3 Raman Spectrum Analysis

The analysis of the droplet's retrieved Raman spectrum involves first finding the whispering gallery modes (WGMs) in the raw spectrum and then fitting the wavelength positions of these peaks to a homogeneous Mie scattering model to retrieve the droplet's diameter, d_p, and refractive index, n[106,107]. At the wavelength of each WGM the droplet acts as a high finesse optical cavity where the WGMs form a standing wave on the droplet surface – this greatly amplifies the Raman scattered signal at that discrete wavelength[103–105]. The WGMs are thus superimposed on top of the broader Stokes shifted vibrational modes in the droplet's Raman spectrum. I show example droplet Raman spectra in Figure 2.2. The spectrum is reported as a Raman shift in units of wavenumbers (cm^{-1}) that accounts for the excitation laser's wavelength (532 nm).

My previous WGM peak finding method for Raman spectral analysis relied on a smooth spline fitting of a single spectrum (to capture the broad Raman mode) with a Gaussian fit to the WGM peaks above the smoothed spline[107,113]. Although this method works well for WGM peaks with a signal-to-noise ratio > 20, it produces many false positives when used to find WGM peaks at a S/N < 10. This posed a problem for the analysis of my pure organic droplets where there are fewer large WGM peaks with S/N > 10 in the narrow C-H Raman mode to constrain the fit. Aqueous droplets have a broad O-H Raman water stretch mode that supports a larger number of intense WGM peaks, facilitating the fitting. To find the less intense WGM peaks in the Raman spectrum I developed a signal processing method using a non-local means denoising algorithm and wavelet transforms, which is described in Appendix A. This signal processing allows us to find WGMs that have peak intensities with S/N > 2.4, and can find even weaker WGM peaks (S/N = 1.2-1.6) depending on the noise level of the data.

Once I identify the WGM positions, I use the Mie scattering algorithm developed by Preston and Reid (2013) to independently determine both the size and refractive index of a homogeneous droplet. The diameter (d_p) can be determined to an accuracy of ±0.05% and the refractive index (n) to ±0.11%[106,107]. When I apply this homogeneous algorithm to a core-shell droplet I can use the plausibility of the retrieved refractive index and diameter parameters as well as an abnormally high fit error to identify a droplet with a core-shell morphology[109]. This method of determining whether the droplet has a homogeneous or phase-separated core-shell morphology will be important for the interpretation of my results.

2.3.4 Direct Detection of Phase Separation

The WGMs generated by the droplet are the crucial evidence constraining the assignment of morphology[48,52]. I show examples of Raman spectra for a homogeneous, a core-shell, and a partially-engulfed droplet in Figure 2.2. The easiest morphology to observe is the partial-engulfing structure because it breaks the spherical symmetry and thus quenches any WGMs, leaving only the broad Stokes Raman vibrational modes [52].

The partially-engulfed morphology can sometimes also be observed in the bright-field visual image[47].

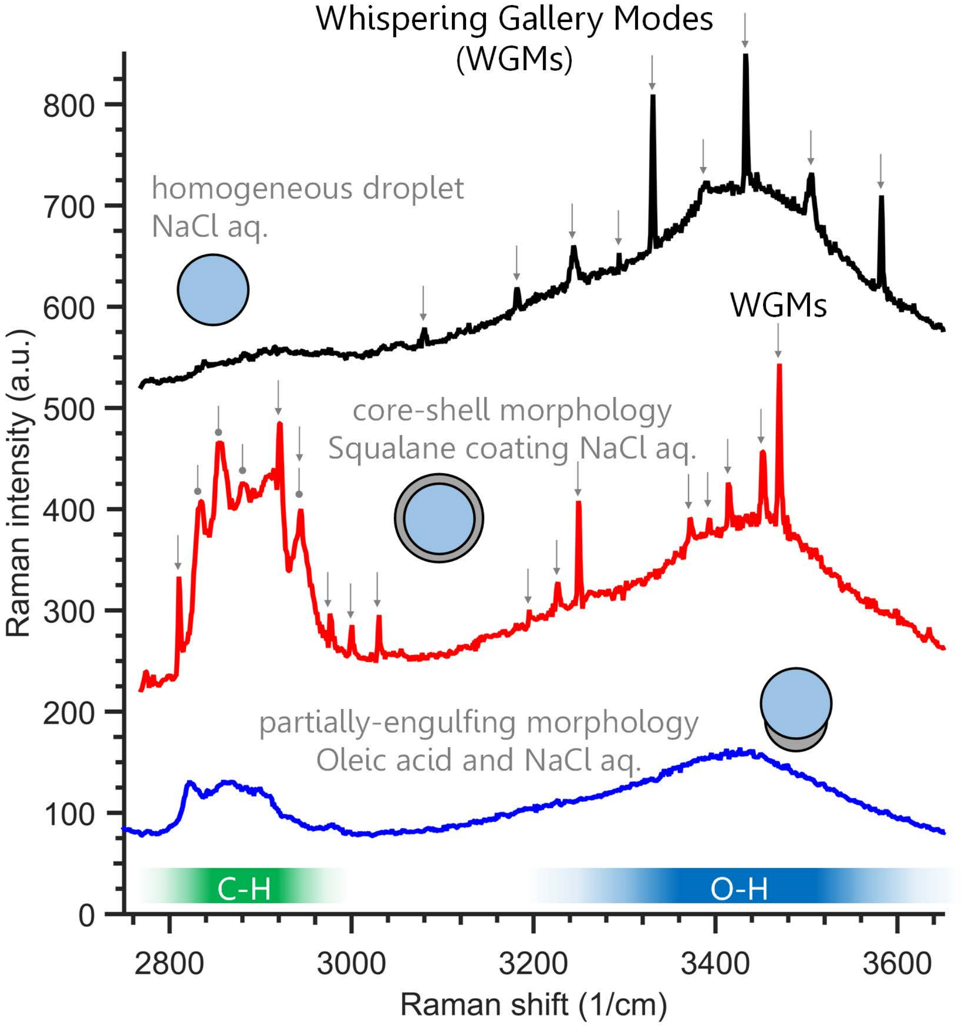

Figure 2.2. Example Raman spectra from tweezed droplets with WGMs indicated by arrows. Top: A homogenous, aqueous NaCl droplet has only the broad O-H Raman band (spectral range indicated by the bottom right blue bar). Middle: The squalane coated aqueous NaCl droplet has both the O-H and C-H Raman bands, where the C-H Raman band is caused by the squalane (spectral range indicated by the bottom left green bar). Both broad modes support WGMs. Note the circular tipped pointers indicate narrower Raman features indicative of squalane, on top of which WGMs can also form. Bottom: A spectrum from a partially-engulfed morphology of oleic acid and aqueous NaCl, where both the broad C-H and O-H modes are observed, but no WGMs are present.

The core-shell morphology is characterized by WGMs that are influenced by both the core and shell phases. Prior identification of a core-shell morphology relied on the interpretation of the WGMs and the retrieved homogeneous fit parameters and fit error[109]. This determination is different from the partially-engulfed situation that lacks WGMs, as the WGMs generated in the shell can travel in and out of the core, depending on the shell's thickness.

The main effect observed for core-shell droplets is an increase in fit error and/or unphysical refractive index and diameter changes; a homogeneous single-phase model simply will not fit the WGMs positions accurately. Another piece of evidence to support a core-shell formation is a change in the peak separation between adjacent transverse electric (TE) and transverse magnetic (TM) WGM peaks[109]. To use that method requires a relative humidity induced phase separation going from a core-shell to homogeneous morphology and back where the size does not vary significantly but the apparent refractive index retrieved from a homogeneous fit would suggest otherwise. The systems studied here do not experience RH induced phase separations. Instead I rely on the interpretation of the homogeneous fit error, droplet refractive index, and size to identify if a homogeneous Mie scattering model is valid.

2.3.5 Core-Shell WGM Fitting Algorithm

To conclusively demonstrate my ability to distinguish the morphology of a core-shell versus a homogeneous droplet, and to recover meaningful physical parameters from core-shell droplets, I have developed a fitting algorithm for the Mie scattering of a core-shell morphology. A previous core-shell algorithm could fit for the diameter, refractive index, and chromatic dispersion $\left(\frac{dn}{d\lambda}\right)$ for the core and shell but required WGM labels *a priori*, which I do not have[137]. WGM labels are mode number, mode order, and EM wave type (either transverse electric (TE) or transverse magnetic (TM)) for each WGM. In another recently published core-shell algorithm they assigned the refractive index and chromatic dispersion of the core and shell *a priori*, and then determined the diameter of the core and shell, and the WGM labels[109].

The core-shell optimization problem involves finding the global minimum on a non-convex error space, just as in the case of the homogeneous algorithm. I used a gridded search over the six droplet parameters: the diameters, refractive indices, and chromatic dispersions for both the core and shell phases. Then for each parameter set I also need to optimize for the WGM labels, which have discrete values for the mode number (30 to 80), mode order (1 to 3), and EM wave type (TE or TM). For the optimization of the WGM labels I search possible combinations to find the combination with the lowest error for each set of droplet parameters. I sample the droplet parameter space using a gridded search with a specified resolution for each parameter. This algorithm locates the minimum in one spectrum in > 24 hours when running on a 4 core 2.60 GHz CPU. The optimization results of the first spectrum can then be used to constrain the optimization of the next spectra, decreasing subsequent computation time. Applying my core-shell algorithm to the phase-separated experiments will allow us to retrieve more details regarding the solubility, volatility, and diffusion coefficients of the components in the two phases.

2.4 Results

2.4.1 Assessment of Trapping Chamber Performance

The chamber design was first prototyped by 3D printing out of ABS polymer to test the validity of the design before the final version was machined from aluminum. I were able to successfully tweeze droplets within the 3D printed chamber but it had one important drawback. The porous nature of the 3D printed polymer structure made humidity control impractical as the chamber walls acted as a capacitor for changes in relative humidity (RH). Thus, with minor modifications the final design presented here was fabricated out of aluminum in the Mechanical Engineering machine shop at Carnegie Mellon University. The experimental data shown here were all obtained using the aluminum chamber.

To assess the equilibration timescale of my chamber I tweezed a saturated aqueous NaCl droplet as a responsive probe to humidity changes. An NaCl droplet has a low viscosity, similar to that of water, and equilibrates promptly with changes in the relative humidity of the surrounding gas phase. This equilibration is much faster than the calculated bulk equilibration timescale of the chamber (1.44 min). Thus by fitting the size of a rapidly responding droplet to an exponential decay after a step change in RH I can determine the actual equilibration timescale of the chamber.

I nebulized droplets from a saturated solution of NaCl in water because this produces the largest droplet sizes and facilitates trapping. Once I trapped the droplet I ramped the RH up and down in approximately 4% RH steps from 65% to 88% RH, holding the RH constant for 20 min at each step. I cycled RH up and down 6 times, for a

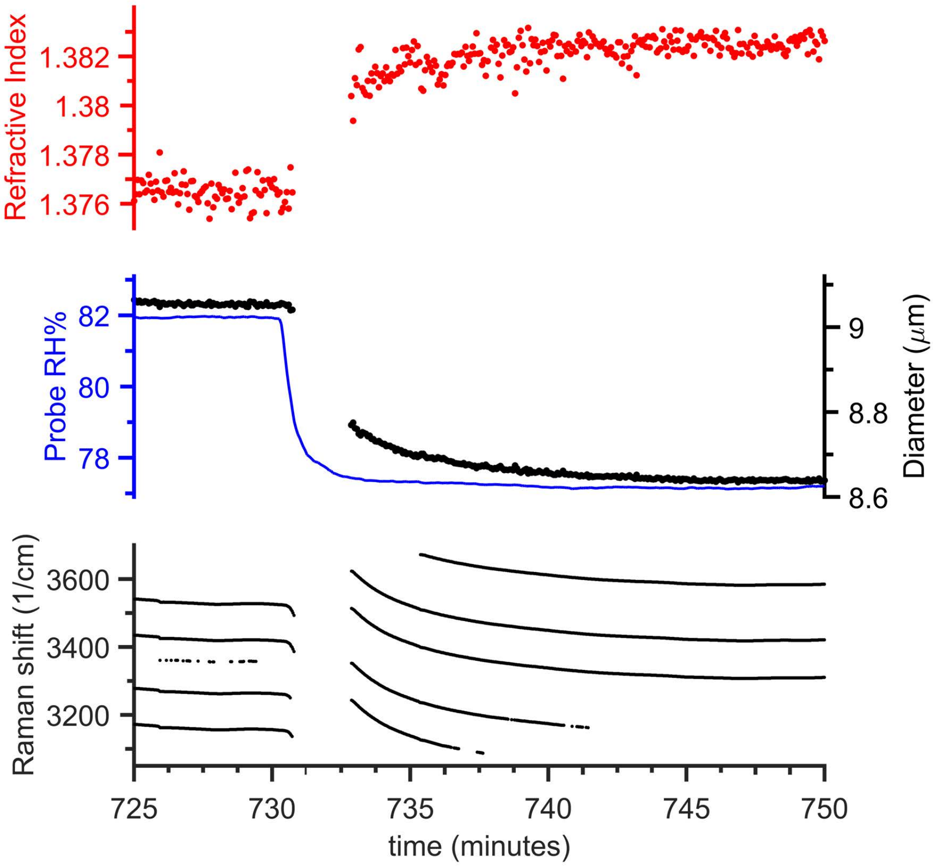

Figure 2.3. Timescale of changes in droplet size and refractive index, determined from fitting the Raman shift positions of the WGMs, as the chamber RH was stepped, to determine the chamber's equilibration timescale. An aqueous NaCl droplet was used, nebulized from a saturated solution of 0.4 g/mL. An excerpt of the experiment is shown here – see the Supplemental Information for the full 20 hour experiment. The RH steps were in increments of 5% in the humid air flowrate, while holding the total conditioned air flow at 0.35 Lpm. Each RH condition was held for 20 minutes before stepping to the next. At each RH step the droplet diameter rapidly changes causing the observed WGMs to become blurred, which results in a gap of WGMs and retrieved fits.

total experimental length of almost 20 hrs. I show a segment of the experimental data in Figure 2.3. This figure is also a good reference for the typical scatter in the retrieved refractive index and size from the Mie fitting of a homogenous droplet as the droplet's size and composition changes in response to changes in its surrounding gas-phase. Note that the WGMs are sometimes lost in the initial portion of an RH step change as the rapid change in droplet size blurs the wavelength positions of the WGMs. I isolated the retrieved droplet diameter for each RH step and performed an exponential fit to the change in diameter to determine the equilibration timescale as the e-folding decay time. The average equilibration timescale was 1.83 ± 0.36 min for RH below 82% (the uncertainty is the standard deviation of 36 timescale measurements, see the supplemental for the full 20 hour dataset). Above 82% RH I observed an increase in the measured timescale, which I attribute to partial wetting of the chamber walls and a consequent slow equilibration of water with the walls. I typically performed equilibration experiments at less than 80% RH to avoid this lag.

I applied the same exponential decay fit to the measured RH of the conditioned airflow immediately before it entered the mixing chamber; this yielded an average equilibration timescale for the RH probe (Vaisala) of 0.50 min. The same exponential fit can be applied to the slope of the Raman shift positions of the WGMs instead of to the retrieved d_p. This resulted in an equilibration timescale of 2.08 ± 0.85 min for RH below 82% (the uncertainty is the standard deviation of 28 timescale measurements). This method has an increased uncertainty as I fit the derivative of the WGM wavelength position, which amplifies the scatter in the data. I use this equilibration timescale estimation method for core-shell droplets where the complete diameter time series is not retrieved. Finally, from the middle panel in I can see there is a 30 s delay between onsets of changes in the droplets radius and when the RH probe responded. Therefore, when analyzing the data, onset delays of changes in droplet diameter (or WGM Raman shift) following a step change in RH should be greater than 2 minutes before I consider that the delay may be caused by droplet equilibration limitations, such as caused by low particle-phase diffusivity that impedes the rate of mass transport.

2.4.2 Determination of Partial-Engulfing Morphology for Mixed Droplets Composed of Simple Hydrocarbons

I used dioctyl sebacate (DOS) to test my ability to trap pure organic particles produced with the CMAG. Dioctyl sebacate is a long-chain 26 carbon molecule with two internal ester groups. It is a hydrophobic liquid and thermally stable with a boiling point of 256 °C; these thermal properties make it suitable for use in the CMAG. To demonstrate my AOT system's ability to create phase separated droplets by the addition of a second phase through coagulation, aqueous glycerol aerosol was generated using the medical nebulizer and allowed to coagulate with the tweezed DOS droplet. Based on bulk phase observations of phase separation when DOS and aqueous glycerol were mixed in a beaker, and the known hydrophobic properties of dioctyl sebacate, it would be expected that phase-separation would occur in the aerosol phase but the specific morphology cannot be predicted from these bulk phase observations alone. The surface and interfacial tensions required to predict the resulting morphology are not known.

The experiment started by trapping a dioctyl sebacate droplet which then slowly evaporated into the conditioned airflow. The evaporation is evident by the negative slope in the WGM traces in Figure 2.4a indicating decreasing droplet diameter as the WGM positions blue shift to shorter wavelength, apparent in the reported spectrum from the shift to smaller Raman shifts. As the WGMs are only created from Raman scattered

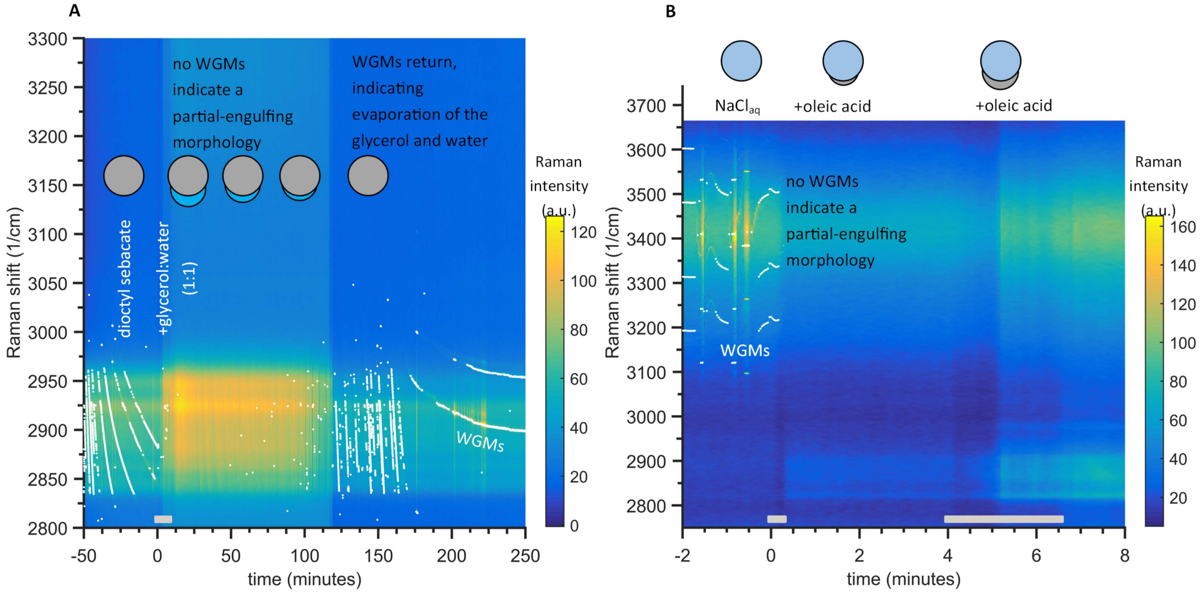

Figure 2.4. A) Raman spectra time series for a tweezed dioctyl sebacate droplet that was then coagulated with small droplets produced from a 1:1 solution of glycerol and water. The C-H Raman mode appears in the spectra between 2825-2975 cm^{-1}, and the color scale indicates the intensity of the Raman signal at that Raman shift position. The bright white points indicate the positions of the WGMs. Negative slopes (decreasing Raman shift) indicate decreasing droplet size. The glycerol:water aerosol was added at 0 min., indicated by the gray bar; the RH was 75%. This caused an almost immediate disappearance of the WGMs, indicating a partially-engulfed morphology was present between 5 min and 115 min. A faint O-H mode from water also appeared between ~3000 and 3300 cm^{-1}. After 115 min. the O-H Raman band faded and the WGMs appeared, indicating the loss of the aqueous phase and the restoration of a homogenous droplet morphology. The evaporation of the glycerol:water phase explains these observations. **B)** Raman spectra for a tweezed NaCl(aq) droplet being coagulated with small droplets of oleic acid, at an RH of 77%. A short 25 second coagulation at 0 min. resulted in a partially-engulfed morphology. The oleic acid addition is also evident by the increase in the C-H Raman mode between 2850-3000 cm^{-1}. After a longer 145 second coagulation period at 4 minutes the partially-engulfed morphology was still present.

photons this presents some unique challenges for fitting d_p and n to the WGMs when a pure organic droplet is trapped. The hydrocarbon C-H stretch mode is much narrower than the broad O-H water stretch mode observed in aqueous systems. Therefore, there are fewer WGM peaks present in the C-H mode to fit droplet diameter (d_p) and n, as few as two WGMs in some cases as seen in the WGM traces in Figure 2.4a. As such only a few frames could be fit for d_p and $n_{650\,nm}$ for the pure DOS droplet.

At zero minutes in Figure 2.4a, ne bulized droplets of the glycerol solution (50% DI water and 50% glycerol) were flowed into the chamber, coagulating with the DOS droplet. Immediately after the coagulation began the WGMs were no longer observed. This indicates that the liquid droplet phase separated into a partially-engulfed morphology, where the non-spherical structure and presence of phase inclusion quenches the surface-resonant WGMs. The aqueous glycerol phase of the droplet then appeared to slowly evaporate over a 115 minute period, after which the WGMs returned indicating the restoration of a homogeneous droplet. The return of the WGMs indicates evaporation of the aqueous glycerol phase and thus the droplet composition returning to the original dioctyl sebacate. Before the glycerol(aq) addition, the average diameter of the DOS droplet was 8.281 µm and $n_{650\,nm}$ was 1.4441. The refractive index is similar to refractometer measurements for DOS of $n_{650\,nm}$ = 1.4463 [138]. After the evaporation of the glycerol(aq) the average d_p was 7.97 µm and $n_{650\,nm}$ was 1.4453, indicating the droplet's composition had returned to that of primarily dioctyl sebacate. I determine $n_{650\,nm}$ from the dispersion $\left(\frac{dn}{d\lambda}\right)$ retrieved from the WGM fit, and report n at 650 nm (see the supplemental for the full WGM fit results). This is the wavelength where n is typically reported from AOT experiments as it corresponds to the center of the aqueous O-H Raman mode (3412 cm^{-1}) where most of the WGMs reside in aqueous droplets[106,107,109,139]. Small amounts of water and/or glycerol may have also been partitioned into the DOS phase when the WGMs returned. However, the similarity of the droplet's refractive index of $n_{650\ nm}$ = 1.4441 before versus 1.4453 after the WGMs disappeared indicates that the composition was still that of DOS, as the small change in n is within the uncertainty of the fit ($n_{650\ nm}$ = 1.4441 ± 0.0016).

This experiment demonstrates the phase separation of dioctyl sebacate and aqueous glycerol into a partially-engulfed morphology, and also showcases the simplicity of determining this type of morphology. It also demonstrates the successful tweezing and retrieval of the diameter and refractive index of a pure hydrocarbon droplet. Organic droplets present new challenges due to the smaller number of WGM peaks available in the narrow C-H Raman mode to use in fitting the droplet's parameters.

The second experiment I conducted to explore a partially-engulfed morphology was the addition of oleic acid to a trapped aqueous NaCl droplet. I show in Figure 2.4b that the coagulation of oleic acid to the NaCl(aq) droplet formed a partial-engulfing morphology, quenching the WGMs due to interference from the lens of oleic acid on the surface of the aqueous droplet. This resulting morphology was also observed using AOT for the same system by Dennis-Smither et al. (2012), and this similar result helps to validate the successful performance of my new tweezing chamber and the proper interpretation of the acquired Raman spectra. After a second longer oleic acid coagulation period, the droplet still remained in a partially-engulfed morphology. This was performed to test the trapped droplet's stability during prolonged aerosol coagulation, and also to explore if the addition of a large amount of immiscible oleic acid might produce a uniform film around the aqueous droplet and a core-shell morphology. The droplet remained stably trapped during the 2 minute coagulation period, with no user intervention (such as adjusting the trapping laser power) required. The lack of WGMs clearly indicates that the morphology remained partially-engulfed. The addition of oleic acid during both coagulation events is observed by the increase in the signal in the hydrocarbon mode's C-H stretch region between 2850-3000 cm^{-1}. From the spreading coefficient framework described above, the morphology will not change simply due to the addition of more mass of one of the phases[48,52,54]. This partially-engulfed structure minimizes the Gibbs free energy of this system through reducing the interfacial surface energy, and thus the partially-engulfed morphology would be expected to persist despite the addition of more organic phase.

2.4.3 Determination of Core-Shell Morphology for Mixtures of Simple Aqueous and Hydrocarbon Components

Hydrophobic squalane (a saturated long-chain 30 carbon triterpene, purity 99%) droplets produced by nebulization of the pure liquid were added by coagulation to a trapped aqueous NaCl droplet. This mixed system was observed to produce a core-shell morphology, and it is used to distinguish from the previous experiment using a DOS droplet mixed with aqueous glycerol that exhibited a partially-engulfed morphology. This experiment was also used to confirm that my new core-shell fitting algorithm

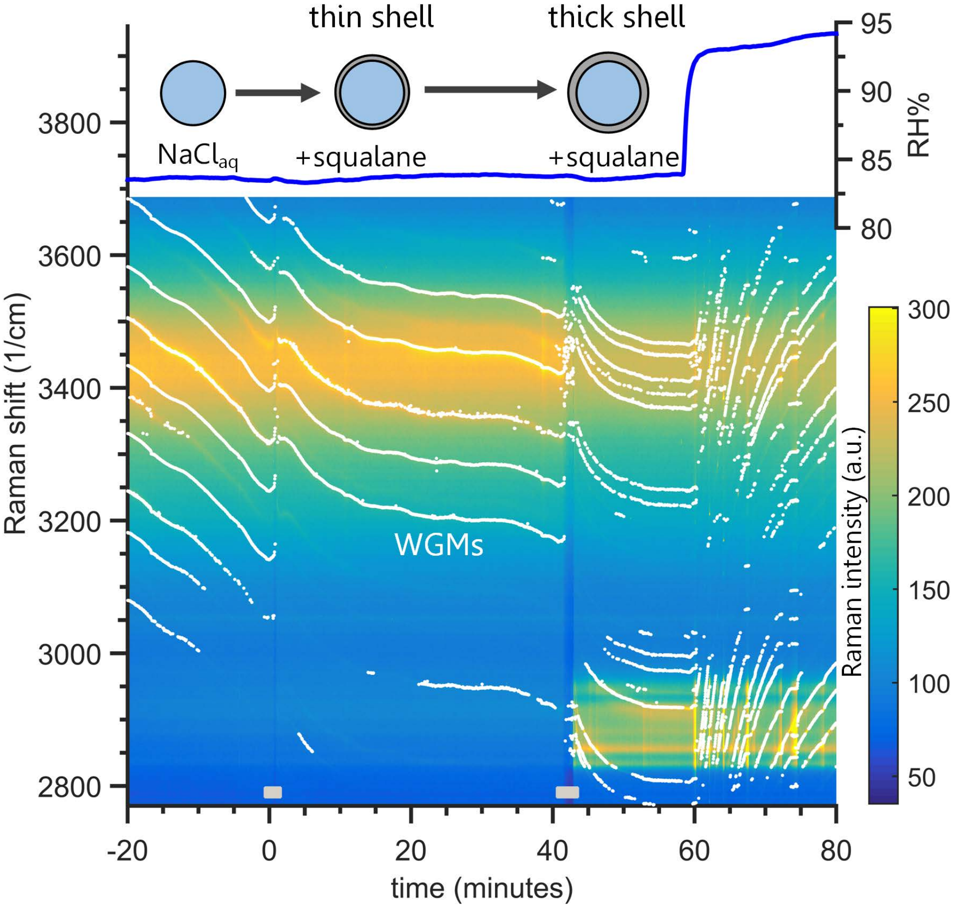

Figure 2.5. Raman spectra time series for a tweezed aqueous NaCl droplet coagulated with squalane aerosol. A NaCl(aq) droplet is shown at -20 minutes, and at 0 minutes squalane droplets were coagulated for the period indicated by the gray bar at the bottom. WGMs are still observed, indicating the squalane formed a thin shell coating. Following the second coagulation period of squalane at 42 minutes a strong C–H Raman band is observed between 2800-3000 cm^{-1}, and WGMs are present in this hydrocarbon mode. This indicates the addition of significant amounts of squalane, which formed a homogenous shell surrounding the aqueous core. A negative trend in the WGM location (bright white points/lines) indicates droplet shrinkage while a positive trend indicates growth. The chamber humidity is plotted on the top, and WGMs have a positive trend after the RH is increased. That indicates the aqueous NaCl core still can uptake water through the hydrophobic squalane shell.

produced valid fits. An aqueous NaCl droplet was trapped and stabilized at 75% RH for 20 minutes to assess the starting droplet size before a short pulse of nebulized squalane aerosol was injected. Figure 2.5 shows the progression of the WGMs and the Raman spectrum after the first squalane pulse was added at 0 minutes.

Note that after 0 minutes the WGMs were still present, and there was almost no change in the background intensity of the broad C-H Raman band. The hydrocarbon immersion oil used with the microscope objective does cause a weak background C-H Raman signal. That rules out a partially-engulfed morphology, and the small signal for the C-H band suggests very little squalane was added compared to the amount of water in the droplet (observed from the O-H Raman band).

As the homogenous fit produced an unrealistic refractive index and high fit error after the first squalane addition, the morphology was likely core-shell (Figure 2.6). A thicker squalane coating was produced by adding more squalane aerosol at 42 minutes and then a clear increase in the C-H Raman band was observed, with prominent WGMs in both the aqueous O-H and hydrocarbon C-H stretch modes. The retrieved refractive index and size from the homogeneous fit are now even more unphysical, as the scatter in the diameter and refractive index and a high fit error demonstrate in Figure 2.6. Taken together these observations indicate the presence of a phase separated droplet with a core-shell morphology.

To confirm that a core-shell morphology was formed, a one spectrum frame at 60 minutes was fitted with the new WGM core-shell algorithm. The derived parameters at

60 minutes indicate a core of aqueous NaCl ($n_{650\ nm} = 1.3715, d_p = 8.41\ \mu m$) and a shell of squalane ($n_{650\ nm} = 1.4450, d_p = 10.26\ \mu m$). The core and shell refractive indexes, and the different fit diameters, confirm that the squalane was coating the NaCl(aq) phase. Pure squalane has $n = 1.4474 \pm 0.0002$ at 589.3 nm [140]. After 60 minutes the relatively humidity was increased from 83% to 93% and I observed droplet growth from the positive slope of the WGMs. The equilibration timescale I retrieved from the slope of the WGMs was 4.11 ± 0.10 min, which is within the 1.5 to 5.1 min range observed for an uncoated NaCl(aq) droplet at a RH greater than 82% (see Appendix A for more details). This water uptake response indicates that the aqueous NaCl core still responds promptly to gas-phase humidity changes even though it is coated by a hydrophobic shell, and the squalane has no measurable effect on the equilibration timescale. Prior AOT experiments have used an increase in the RH equilibration timescale to assess diffusion limitations of water through viscous droplet phases[110,141].

To further support this proposed squalane shell on NaCl(aq) core morphology I can use the surface active nature of the WGMs to explain why the homogeneous fit performed poorly and gave unphysical changes in n and d_p. I use the fractional radial penetration depth of the WGMs, which is approximately one minus the inverse of refractive index, $\left(1 - \frac{1}{n}\right)$[142]. For most materials, I can use an upper bound of 30% of the droplet radius. This means that the WGMs do not probe the droplet from its center to 70% of its radius and only exist in the outer 30% of the radius. Therefore, the refractive index retrieved from fitting the WGMs corresponds to the composition of the droplet in the outer 30% layer of its radius. Taking this into account, and considering the small amount of squalane that was added to the droplet initially, the squalane must have formed the coating, and not the core of the droplet. In other words, for squalane to have

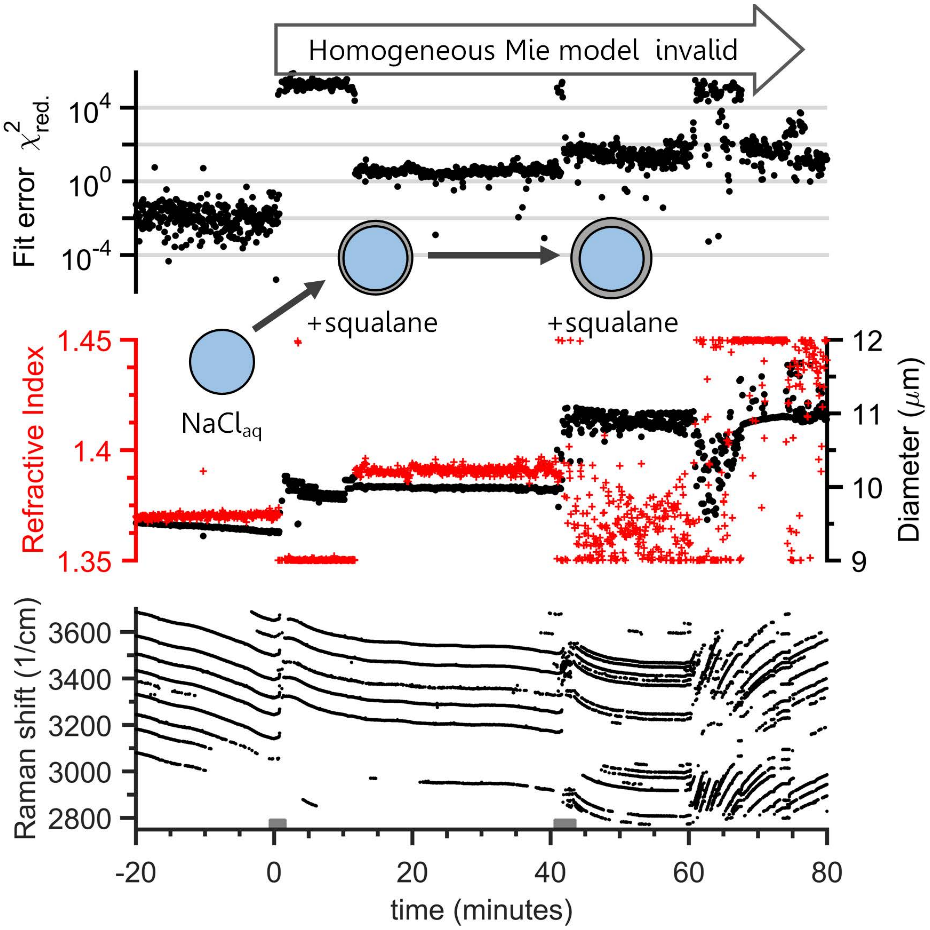

Figure 2.6. Homogeneous Mie fit parameters for the tweezed aqueous NaCl droplet that was then coagulated with squalane aerosol from Figure 2.5. Top panel shows the reduced χ^2 fit error from fitting the WGM positions to a homogenous Mie scattering model – note the log scale. The middle panel plots the fitted droplet refractive index (+) and diameter (o) from the Mie fit. The bottom panel shows the wavenumber position of the WGMs. The gray bars at the bottom indicate periods of squalane addition. After the first squalane addition at 0 min the fit error increased and an unrealistic change in diameter and refractive index are observed. This indicates that the WGMs do not represent a homogenous droplet. This result was further confirmed after the second squalane addition at 42 min. where the fit error increased and the retrieved parameters change unrealistically. This is explained by the formation of a shell of squalane around the aqueous core.

formed the core phase it would have to compose a volume equal to greater than 70% of the droplet's radius, which would require adding the equivalent of a 7.7 µm droplet of squalane. This logic chain can be used in future phase-separation experiments to determine which phase is the shell coating versus at the core, along with the retrieved values of *n*. The results from the new core-shell fitting algorithm discussed above provide additional information that further validates the determination of a core-shell morphology.

2.5 Discussion of Results

I have demonstrated how the uniformly mixed gas phase flow delivered to the trapped droplet's position in my new AOT chamber design facilitates trapping and stability during the addition of a second phase through aerosol coagulation. This enables AOT experiments on more complex aerosol systems that more realistically mimic atmospheric aerosol compositions. Additional material can also be added through vapor condensation. The chamber is also designed to facilitate the *in situ* production of secondary organic matter inside the tweezing chamber through the oxidation of precursor vapors; I will demonstrate these new capabilities in Chapter 4 & 5. The drawback to the chamber's current large size is the long equilibration timescale of the tweezers chamber's air volume to changes in RH and gas-phase composition. The shortest timescale I can theoretically achieve by adjusting the airflow rates is 0.55 minutes. For future tweezing chambers based on this design where shorter equilibration timescales are desired, the whole height of the chamber could be compressed by at least half. The only limitation with that change is the airflow fields around the droplet must be stable and uniform so as to not push the droplet out of the optical trap. This would be largely determined by the height of the trapping chamber and providing enough distance for the airflow to expand and relax as it enters the lower tweezing chamber so it achieves a symmetrical and low velocity as it approaches the droplet.

Using three liquid-liquid phase separation experiments I demonstrated that my chamber can reliably and stably combine two immiscible phases by coagulation of a second phase to the initial aqueous or hydrocarbon droplet and subsequently determine the resulting morphology. The analysis and precise interpretation of the Raman spectra and their WGMs is limited by the use of a homogenous Mie scattering model to fit the WGM positions. I have demonstrated that my core-shell Mie fitting algorithm can retrieve physically realistic properties of both the core and shell phases, when the experimental evidence indicates that a core-shell morphology exists. The algorithm is currently computationally expensive, requiring 24+ hours to analyze a single Raman spectrum frame, and thus was only used to analyze isolated periods of the experiments. The details and capabilities of my new algorithm will be fully described and explored in Chapter 3. From these fits of both the core and shell phase properties (diameter and refractive index) I am now able to proceed in determining important quantitative properties from complex mixed aerosol experiments such as component vapor pressures, hygroscopicities, and diffusion coefficients.

2.6 Conclusions

My study of the morphology of immiscible aerosol systems has assembled the advanced methodology that enables future experiments on more complex atmospherically relevant droplets. I show that a squalane shell creates no measurable impedance on the uptake of water by the underlying aqueous NaCl core, determined from its measured prompt growth following a humidity ramp. I also highlight the need for an algorithm to fit unlabeled whispering gallery modes to a core-shell Mie model, and my preliminary results that fulfill that need. Through the improvement and assessment of my core-shell algorithm these same phase separation experiments would reveal more details about the solubility, volatility, and diffusion coefficients of the components in each of the two phases. This facilitates the analysis of more complex and realistic aerosol systems, which often adopt a core-shell morphology following phase separation.

Future experiments will investigate secondary organic matter produced *in situ* in the tweezing chamber and determine if the SOM mixes or does not mix with different trapped core droplet compositions. I can then determine key properties of the secondary organic matter using the core-shell fitting of tweezed droplets that are difficult to determine using other methods such as are applied to large aerosol chamber reactor experiments[9,50,51]. I have highlighted the importance and common occurrence of phase separation and its resulting morphology, and presented a methodology for using the aerosol optical tweezers to determine critical properties of complex aerosols following the addition of new material through coagulation.

3 Determination of the core and shell properties in biphasic droplets analyzed using aerosol optical tweezers

3.1 Abstract

I have developed a new algorithm for the analysis of whispering gallery modes (WGMs) present in the cavity enhanced Raman spectra retrieved from droplets trapped in an aerosol optical tweezers (AOT). My algorithm improves the computational scaling when analyzing core-shell droplets (i.e. phase-separated or biphasic droplets) in the AOT, making it computationally practical to analyze spectra collected over many hours at a few Hz. This enables the determination of the size and refractive index of both the core and shell phases with high accuracy, at 2 Hz time resolution. I present in detail how my approach can reduce the number of parameters directly searched for and how I sort WGMs into series; thus reducing the computational demands. I assess the accuracy of my fitting for the diameters and refractive indices (including dispersion) of the droplet's two phases using simulated data. This was performed for both a homogeneous droplet and a core-shell droplet. Two experimental datasets are presented, the first showing how the formation of a shell coating causes adjacent WGMs to split from each other. This was

done through the addition of alpha-pinene secondary organic aerosol to a NaCl(aq) droplet. The second experiment demonstrates the new core-shell fitting on experimental data from a droplet of aqueous glycerol coated by squalane. Using the independently retrieved refractive indexes of each phase I then assess the solubility of the two chemical phases in each other. My new algorithm paves the way for more in-depth physiochemical experiments into liquid-liquid phase separation and their consequences for interfacial chemistry – a topic with growing experimental needs for understanding the dynamics and chemistry of atmospheric aerosol particles.

3.2 Introduction

The aerosol optical tweezers (AOT) has become a valuable instrument to understand aerosol properties including viscosity, diffusion coefficients, hygroscopic growth factors, and heterogeneous chemistry[47,48,52,53,57,107,108,111,112,116,123,139,143–150]. In a typical AOT system, a droplet is optically trapped by a focused laser beam, which also induces a cavity enhanced Raman spectrum (CERS). Accurate values for the droplet's size and refractive index are retrieved from the positions of the resonant Raman, commonly called Whispering Gallery Modes (WGMs), in the droplet[106,107]. The WGMs arise as Raman scattered light is amplified in a spherically symmetrical droplet at discrete combinations of size, refractive index, and wavelength as the optical trap holds the droplet in air, acting as a low-loss resonating cavity. These two basic measurements of size and refractive index combined with the stable trapping of a particle enable studies of aerosol physical properties with unprecedented precision and accuracy[145,146,151]. Most studies thus far have focused on homogeneous droplets so that the existing data analysis algorithms developed by Preston and Reid[106,107] can be employed. However, there is evidence that a core-shell morphology is common in many aerosol systems[19,39,42], creating the need for an effective way to retrieve physical properties from spherically symmetrical core-shell droplets[44,108]. Core-shell morphologies dramatically change the particle's interfacial chemistry and properties, thus altering its interactions with radiation and reactive gases, it's equilibration timescale with the gas-phase, and its ability to uptake water that is a critical component of the activation of particles into cloud droplets and ice crystals[152–155]. Here I present an effective computational approach that expands upon the methods briefly described in Gorkowski et al. (2016) (Chapter 2), and tests the accuracy of this algorithm.

WGMs are morphological resonances inside a spherical droplet that form a standing wave around the droplet's circumference. Since WGMs depend on the morphology of the droplet they can be used to distinguish between a homogeneous droplet and a core-shell droplet, and the lack of WGMs can indicate a non-spherical partially-engulfed morphology[47,48,52,108,109]. However, studies of core-shell droplets have to date been limited to select cases with additional constraining information. A previous algorithm required *a priori* WGM labels specifying the mode number, mode order, and EM wave type (either transverse electric (TE) or transverse magnetic (TM)) for each WGM[137]. Another way to constrain the fit is to assign the refractive index and chromatic dispersion of the core and shell *a priori*, and then fit the diameter of the core and shell, and the WGM labels[109].

Lastly, in my previous work I implemented an exhaustive direct search approach that could fit an isolated set of WGMs with no additional constraints but which took 24 to 48 hours for each Raman spectra frame measured every 2 seconds. This approach is too computationally expensive to analyze AOT experimental datasets that are often acquired over many hours. Here I present an improvement upon my earlier algorithm that can fit an individual set of WGMs in one Raman frame in less than 10 minutes using a personal computer. However, a typical AOT experiment lasting 6 hours generates 11,000 individual spectra, and so treating the entire experiment as a set of independent spectra would still require approximately of 51 days to analyze. Since the spectra are not independent, I use comprehensive fits on a small subset of the spectra to assign the WGM labels for the rest of the spectra collected, reducing the total computation time to a day or less.

3.3 Whispering Gallery Mode Theory

The solutions for Mie light scattering from homogeneous droplets and core-shell droplets have been studied and used extensively[106,107,137,156–162]. Using Lorenz-Mie scattering theory, I numerically solve for the whispering gallery modes, which are sharp resonances in the broader Mie scattering band. I follow the solution form presented in Bohren and Huffman[163] and shown in the Appendix B. The WGM resonances correspond to standing electromagnetic waves with an integral number of wavelengths around the circumference of a spherically symmetrical droplet. When the spherical symmetry is broken, the standing waves do not exist.

The WGM resonances occur when the denominator of the Mie scattering coefficient vanishes. Therefore, to find the resonance position, I set the denominator equal to zero and solve for the Mie size parameter (*x*) given a refractive index (*m*), mode number (*n*), and mode order (*o*). The Mie size parameter is a dimensionless number relating the circumference of the particle ($\pi\ d_p$) to the wavelength (λ) of the light; $\chi = \pi\ d_p/\lambda$. The homogeneous case has an approximate analytical solution; however, I use this only as a starting point for my numerical solution, as Preston and Reid[107] showed it to have significant errors in the resulting resonance position. However, the analytical solution is sufficient to constrain the mode order. Given the mode order, I then solve Eqn. (3.1) for the transverse magnetic and Eqn. (3.2) for the transverse electric resonances for a homogeneous sphere. The solution utilizes Riccati-Bessel functions ξ_n, ψ_n, and χ_n – a prime indicates the first derivative with respect to the argument.

$$0 = m\psi_n(mx)\,\xi_n'(x) - \xi_n(x)\,\psi_n'(mx) \tag{3.1}$$

$$0 = \psi_n(mx)\,\xi_n'(x) - m\xi_n(x)\,\psi_n'(mx) \tag{3.2}$$

For a core-shell system the standing wave propagates in two distinct dielectric materials, and the solution is very sensitive to both materials when the thickness of the shell is comparable to the wavelength of the resonating light. For the core-shell solution I again set the scattering coefficient's denominator equal to zero. I then derive Eqn. (3.3) for the transverse magnetic resonance and Eqn. (3.4) for the transverse electric resonance. In the core-shell notation I added subscripts for the shell (s) and core (c) refractive index and core radial fraction (f_c), and the Mie size parameter (χ) is defined by the shell diameter. The influence of the core is folded into two additional terms A_n and B_n which are defined in Eqns. (3.5) and (3.6).

$$0 = \xi_n(x)[\,\psi_n'(m_s x) - A_n\,\chi_n'(m_s x)] - m_s\xi_n'(x)[\,\psi_n(m_s x) - A_n\,\chi_n(m_s x)] \tag{3.3}$$

$$0 = m_s\xi_n(x)[\,\psi_n'(m_s x) - B_n\,\chi_n'(m_s x)] - \xi_n'(x)[\,\psi_n(m_s x) - B_n\,\chi_n(m_s x)] \tag{3.4}$$

$$A_n = \frac{m_s\psi_n(m_s x f_c)\psi_n'(m_c x f_c) - m_c\psi_n'(m_s x f_c)\psi_n(m_c x f_c)}{m_s\chi_n(m_s x f_c)\psi_n'(m_c x f_c) - m_c\chi_n'(m_s x f_c)\psi_n(m_c x f_c)} \tag{3.5}$$

$$B_n = \frac{m_s\psi_n(m_c x f_c)\psi_n'(m_s x f_c) - m_c\psi_n(m_s x f_c)\psi_n'(m_c x f_c)}{m_s\chi_n'(m_s x f_c)\psi_n(m_c x f_c) - m_c\psi_n'(m_c x f_c)\chi_n(m_s x f_c)} \tag{3.6}$$

To initialize the numerical solution for the core-shell WGMs I start with a core fraction of one and use the homogeneous solution. Then I incrementally decrease the core fraction in variable step sizes of 10^{-4} to 10^{-8}. I decrease the step size when the numerical solution results in a non-smooth change from the previous result.

Using the numerical solutions to Eqns. (3.1-6) I generate a database of Mie resonances for both droplet morphologies. The homogeneous database returns a Mie resonance given a refractive index (*m*) and WGM label (*l*), which corresponds to a specific transverse electric or transverse magnetic resonance, mode number, and mode order. The mode number corresponds to the number of standing wave nodes that are along the interior surface of the droplet. The mode order corresponds to the number of standing wave nodes as you move in radially from the surface of the droplet – these are essentially higher order resonances. Either the electric or the magnetic field can be transverse, which denotes which field of the electromagnetic wave is propagating parallel to the droplet's surface. The core-shell database returns a Mie resonance given a shell-refractive index (m_s), core-refractive index (m_c), core-fraction (f_c) and WGM label. The core-fraction denotes where along the droplet's radial axis the refractive index changes between the core and the shell. Refractive indexes change as a function of wavelength, therefore to constrain the refractive index dependence on wavelength I use a chromatic dispersion relation, Eqn. (3.7) following Preston and Reid[107], where m_0 is the refractive index at a specified wavelength (typically 650 nm) and m_1 is the dispersion term which accounts for the wavelength dependence. This refractive index dependence on wavelength is also used in the inverse fitting to constrain the fit as the WGM positions are measured across a range of wavelengths.

$$m_\lambda = m_0 + m_1\left(\frac{1}{\lambda} - \frac{1}{\lambda_0}\right) \tag{3.7}$$

Using the database for the homogeneous case, I can generate WGM values simulating different experimental conditions. Shown in Figure 3.1 is a simulation of particle growth at a constant refractive index. As the droplet grows, the WGM resonant frequencies increase in wavelength (Raman shift) in parallel. Nearly overlapping WGMs will result in merged peaks in the measured data, but this is not detrimental to the fitting. While for any given pair of indices the WGMs progress in sequence (i.e. TM^1_{62}, TM^1_{63} TM^1_{64},...), the overall sequence of all of the WGM labels at a given diameter is not universal as the relative positions depend on refractive index. I show a similar plot to Figure 3.1 in the Appendix B for refractive index and chromatic dispersion dependencies. For a homogeneous droplet, the diameter is the most sensitive parameter to WGM

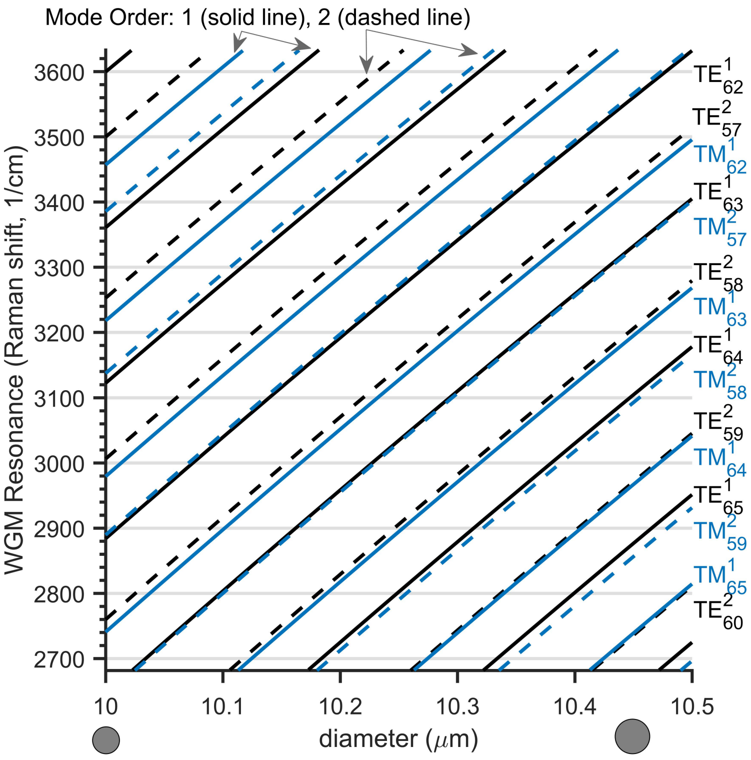

Figure 3.1. Homogeneous droplet growth by 500 nm in diameter, at a constant refractive index of 1.37. The WGM resonance wavelength is converted to a Raman shift from 532 nm incident light, consistent with AOT experiments. Select WGM labels are indicated by TE for transverse electric (black) and TM for transverse magnetic (blue). The superscript is the mode order and subscript is the mode number. Solid lines are mode order 1 and dashed lines are mode order 2.

position, with a change of 0.66 nm in the retrieved d_p per 1 cm^{-1} change in the WGM's Raman shift, with less sensitivity to refractive index at 0.000095 (m_0) per 1 cm^{-1} and a chromatic dispersion sensitivity of 0.004 µm (m_1) per 1 cm^{-1}. These sensitivities are the average slopes of the WGMs across droplets of typical size and composition; see the Appendix B for more details.

The parallel nature of the homogeneous WGM solutions shown in Figure 3.1 does not translate to the core-shell WGMs. I generated core-shell WGM values simulating the addition of a shell phase onto a core phase, shown in Figure 3.2. The WGM series do not

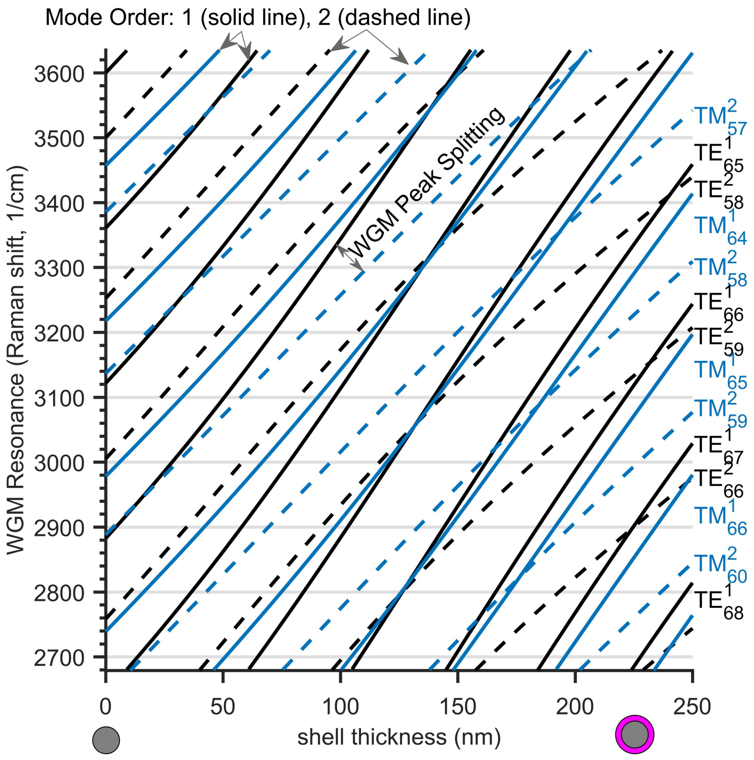

Figure 3.2. Core-shell droplet growth for a 10 μm core with a refractive index of 1.37, as in Figure 3.1. Growth adds a shell with refractive index 1.45 and the indicated thickness. The WGM labels follow the same notation as Figure 3.1.

evolve in parallel because the different mode orders of the standing wave have a different radial penetration depth and thus a different relative sensitivity to the dielectric properties of the shell and the core. Mode order 1 is more sensitive to changes at the droplet's outer surface where the shell resides than mode order 2 is, as this mode order traverses more deeply into the droplet. The transverse electric WGMs have a sharper radial intensity distribution than the transverse magnetic modes, which also contributes to the non-parallel evolution. From Figure 3.2 I also identify that WGMs that were overlapping in the homogeneous spectrum become resolvable because they split when the shell grows. This WGM peak splitting and non-parallel WGM evolution with changing size are qualitative patterns that can be used to distinguish core-shell WGMs from homogenous WGMs. More broadly, the non-parallel evolution indicates a radial gradient in properties near the droplet surface with a length scale of 10s to 100s of nm.

3.4 Inverse Algorithms for WGM analysis

3.4.1 Overview

I developed an inverse optimization algorithm that applies to both the homogeneous and the core-shell morphology. The goal of the algorithm is to efficiently and accurately match the WGM positions identified in the Raman spectrum to a specific combination of diameter and refractive index using Mie theory. In this inverse problem I am optimizing the diameter (d_p), the refractive index (m_0) along with dispersion (m_1) as described in Eqn. 3.7, and the specific WGMs labels (l) as displayed in Figure 3.1 and 3.2. I first describe the previous algorithms and how the problem scales geometrically as the number of parameters increases. I then precede to outlining the optimization of a single spectral frame of data, starting with how to internalize optimization of d_p and therefore decrease the parameters directly searched for by one. I then discuss how the combinations of discrete WGM labels are found. Lastly, the procedure for optimization of the refractive index parameters (m_0, and m_1) is presented. I then take another step back and discuss how I can use a full time series of WGMs to further constrain the WGM label (l). As finding the optimum set of WGM labels is a large fraction of the computational time, not having to do that for every single frame of data significantly speeds up the analysis of experiments.

3.4.2 Optimization Algorithm Description

The current algorithms in the literature for homogeneous droplets are a combination of direct search and least-squares minimization[106,107,164]. In a direct search the computation scales as the number of parameters (d_p, m_0, m_1, and l); for a homogeneous droplet that is n^4 for a single spectral frame (n_{frame}). An improvement to this was first proposed by Preston and Reid[106]. Their algorithm used a low-resolution search and subsequent refinement using an R-squared minimization. This results in a scaling of approximately $(n^3+1)n_{frame}$, resulting in a one-second fit time per frame. To extend to a core-shell parameter space using a fully direct search across all the fit parameters would result in a $(n^7)n_{frame}$ scaling (d_p, f_c, m_{C0}, m_{C1}, m_{S0}, m_{S1}, and l). My initial implementation of this direct search resulted in a fit time of 24 to 48 hours per frame depending on step size and parameter ranges, making this aproach unrealistic even if I went from using a single CPU to a cluster. This geometric scaling of the direct search algorithm makes the core-shell implementation unfeasible to analyze experimental data sets routinely, as n_{frame} can typically exceed 11,000.

My algorithm overcomes this computational challenge through three innovations. First, I internalize the d_p search via the Mie size parameter so that it is now an internal constraint, thus decreasing the scaling by one factor. Second, I employ a random search (n_{rand}) over f_c, m_{C0}, m_{C1}, m_{S0}, and m_{S1} to find possible sets of WGM labels (n_{pWGM}). Third, I take the individual WGMs and group them temporally into WGM series (n_{series}), such that each series has a single WGM label (see Appendix B, Figure 8.3, for an example). This results in an approximate single-frame scaling for a homogeneous droplet of

$(n_{\text{rand}}n_{\text{series}}+n^2)n_{\text{pWGM}}$ and for a core-shell droplet of $(n_{\text{rand}}n_{\text{series}}+n^5)n_{\text{pWGM}}$. Once the labels are known for each of the n_{groups} then the scaling for the time series is n^2n_{frame} for homogeneous droplets and n^5n_{frame} for core-shell droplets. The resulting fit time for the homogeneous case is 2.6 seconds per frame for unlabeled WGMs and 9 ms per frame for labeled WGMs. For the core-shell case it is 6.8 minutes per frame for unlabeled WGMs and 0.57 seconds per frame for labeled WGMs. The outline of the algorithm is shown in Appendix B, Figure 8.5.

3.4.3 Fitting a Single Raman Spectrum

My first efficiency gain was to convert d_p into an internal constraint. This uses the Mie size parameter (x) to relate the given WGM positions to each other. As d_p can be assumed to be constant in a single spectral frame the positions of the first WGM (λ_1) can be related to another WGM (λ_i) as shown in Eqn. (3.8), where x_i is the Mie resonance for the i^{th} WGM and x_1 is a possible Mie resonance for the first WGM.

$$x_i = \frac{\lambda_1}{\lambda_i}x_1 \tag{3.8}$$

The possible values for x_1 are determined by my search space of WGM labels (l); in this way I constrain the range of possible d_p. This approach is very sensitive to the accuracy of the initial λ_1, which can be the location of any of the observed WGMs. Consequently, I initialize the search with several λ_i values, up to the full set of observed WGMs. In practice, a comprehensive search showed no systematic improvements over using only the first WGM, but to be cautious I initialize the search with the three largest amplitude WGMs. This method of relating one Mie resonance to another internalizes the diameter constraint so that I only need to search across the possible WGM label combinations.

The number of possible WGM labels combinations does not need to be an exhaustive search as I only need to track the best possible combinations. This was where the random search was implemented in guessing a value for m_0 and m_1 for a homogeneous droplet, or for m_{S0}, m_{S1}, m_{C0}, m_{C1} for core-shell droplets, and using a direct search for f_c. Then for each random guess I start with all possible WGM labels for the first WGM, l_1, and then sequentially find the best label for the next WGM in my measured spectrum. The minimization for the next l_i follows by calculating the squared error for each possible l by setting Eqn. (3.8) equal to zero and squaring the result to get Eqn. (3.9). To account for neighboring WGM peaks I keep the 3-5 closest WGM labels that minimize the squared error. This process is then repeated for the next WGM. Then after each i^{th} WGM I remove a fraction (0.5 to 0.8) of the poorest WGM label sets to reduce the computational load, but keep a minimum of 100 WGM label sets. In this step the WGM sets that result in a high error are rapidly removed and are not propagated through the rest of the computation. This process results in the 100 best possible WGM-label sets for that given random guess. The random guess is then repeated until the probability of finding a new and unique WGM-label set is less than 0.25%. For a homogeneous system I averaged 213 unique WGM-label sets and for a core-shell system 488 unique WGM-label sets.

The possible WGM label sets are then each globally optimized across their droplet properties of m_0 and m_1 for a homogeneous droplet and core-shell properties of m_{S0}, m_{S1}, m_{C0}, m_{C1}, and f_c. The global optimization proceeds in two steps. The first is a gridded minimization finding the minimum based on the squared error of the Mie-size parameter:

$$squared\ error = \sum_{i=2}^{WGM\ count} \left(\frac{\lambda_1}{\lambda_i}\chi_1 - \chi_i\right)^2 \tag{3.9}$$

The gridded search is used as the error landscape is non-smooth and non-convex with multiple local minima. Multiple gradient descent and global search algorithms were tested, but to achieve reliable results they required more computational time than the simpler gridded search algorithm. I achieved an efficient gridded search for the many WGM-label combinations and higher dimensional parameter space in the core-shell fit using GPU computations instead of CPU computations as I found that a 4-core CPU desktop with a GPU was 39% faster than a cluster of 32 CPUs.

After an initial global search was completed a local refinement of the optimum using a gradient decent algorithm optimizing the reduced chi-squared value (χ^2_{red}) of the retrieved diameters (d_i) calculated from the Mie size parameter, shown in Eqn. (3.10). The optimal diameter ($\overline{d_p}$) is found by taking the average of each d_i calculated from each Mie size parameter. I propagated the measurement error (σ_i) from the Gaussian fit of the WGM resonance peak in the spectrum.

$$\chi^2_{red.} = \frac{1}{WGM\ count - variable\ count} \sum_{i=1}^{WGM\ count} \left(\frac{d_i - \overline{d_p}}{\frac{\chi_i \sigma_i}{2\pi}}\right)^2 \tag{3.10}$$

The optimum WGM-label set can now be found by ranking the retrieved χ^2_{red} for each WGM-label set. From simulations results shown in Figure 3.3 I found that the optimum WGM-label set is not always the correct one. To account for that I used multiple Raman spectral frames that contain the same WGM series, which is described below, or I take an average result of the multiple minimum. This averaged result is the mean of all WGM-label sets that have a χ^2_{red} error that is lower than the lowest χ^2_{red} error plus a 1σ critical value. This 1σ critical value is based off the degrees of freedom and the cumulative probability of a chi-squared distribution. For a homogeneous optimization, this 1σ critical value is 3.5 and for a core-shell optimization this 1σ critical value is 7.0. I call this type of fitting the 1σ WGM labeled fit. This final averaging step in the 1σ WGM labeled fit increases the error in the fit but tends to gain a more robust result as it averages the degenerate solutions caused by overlapping WGM labels.

3.4.4 Fitting a full Raman spectral time series

The last improvement to the optimization algorithm is the sorting of the individual WGMs into series. This process starts with the first frame of WGMs and places neighboring WGMs in the next frame into series based on the previous frame. If there are no series within the variable threshold (typically 0.2 nm), then that individual WGM creates a new series. This process is then repeated for the full experiment resulting in between 100s to 1000s WGM series; an example is shown in the Appendix B Figure 8.3. The labeling of the WGM series follows the same random search process as described above, but now I averaged the χ^2_{red} value across multiple Raman spectra that contain the same set of WGM series, and therefore the same WGM-label sets. This averaging of the

χ^2_{red} helps resolve which WGM within the 1σ WGM labeled fit has a consistently low error across multiple frames and thus more likely the correct label. For this averaging to be effective I typically use 10 frames for a homogeneous system and 50 frames for a core-shell system. Even with this averaging of multiple frames there are sometimes still multiple WGM-label sets within the 1σ critical value – this is where my algorithm can misidentify a WGM label due to it being too close to another WGM. Further work in incorporating additional information into the algorithm is being pursed, such as using the peak amplitude to constrain the possible WGM labels (TM peaks tend to be smaller than TE peaks) and using the initial fit to find additional WGMs of lower amplitude in the Raman spectrum.

Once the WGM series all have a WGM label then the full time series is fit using the previously discussed global optimization of m_0, m_1, and d_p for a homogeneous droplet and of m_{S0}, m_{S1}, m_{C0}, m_{C1}, d_p and f_c for core-shell properties. Since fitting a set of core-shell WGMs is much faster if the WGM labels are known, fitting the full time series can be achieved when the WGMs are grouped into series. Using the WGM series results in fewer unlabeled fits that need to be completed.

3.5 Results

3.5.1 Algorithm Assessment

To assess my new inverse fitting algorithm I generated WGM positions for a simulated droplet and then added random Gaussian noise to the individual WGM positions. I used a sigma of 0.01 nm, shown by Preston and Reid[107] to be typical for measured WGMs and consistent with the uncertainty of my Raman spectrograph (Princeton Acton) used on my AOT[108]. I simulated all possible WGM labels up to mode order two between 620 nm and 660 nm, which is representative of my typical Raman spectrum acquisition using a 532 nm trapping laser. After finding all possible WGMs, I randomly selected a subset to use in the fit. I progressively added WGMs to the initial random set to probe how the uncertainty changes with the number of WGMs used in the fit. I then repeated this by randomly sampling a new set of droplet properties. For this assessment, I used the algorithm to fit a single Raman spectrum (frame) and did not incorporate any time evolution in the assessment. I describe the details of the simulation bounds as well as a comparison of computation times in the Appendix B Table 7.1.

Using my results from the simulation I compared if the calculated (presumably global) minimum fit captured the known correct WGM-label set. I also tested if the correct WGM label set is within the 1σ critical value of the global χ^2_{red} minimum (defined in section 3.4.3). I show these two cases in Figure 3.3 for both a homogeneous and a core-shell droplet. The solid lines in Figure 3.3 indicate that the correct WGM label is not always at the minimum depending on the number of WGMs used in the fit. This result is less of concern for a homogeneous droplet as there are usually more than 4 WGMs in a typical spectrum, reaching an accuracy of over 95%. However, this is not the case for the core-shell droplet where the additional fit parameters increase the degeneracy in fitting incorrect WGM labels. The increased probability for the minimum of a core-shell droplet to have the incorrect labels is why I implemented the 1σ critical range of the global χ^2_{red}

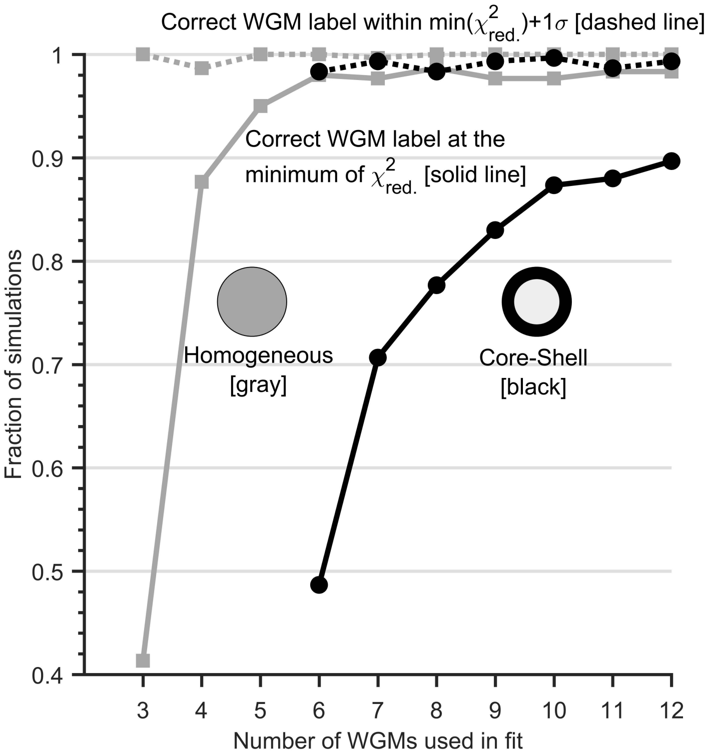

Figure 3.3. WGM labeling results for simulated droplets for a homogeneous (gray) and core-shell (black) morphology. The fraction of simulated fits that had the correct WGM-label set at the minimum is shown with a solid line. The fraction of simulated fits that had the correct WGM-label set within the minimum plus 1σ is shown with a dashed line.

minimum. Figure 3.3 also shows that the correct WGM-label set is near the minimum even if it is not at the minimum due to noise added and the inherent flexibility in the model. That is one reason why I implemented WGM grouping as it helps resolve which WGM label is consistently the minimum across multiple measured spectra.

Using the simulated WGMs and their resulting fits I assessed the error in the resulting droplet parameters retrieved by the algorithm: diameter (d_p) and refractive index (n). I examined two cases: (1) if I know the correct WGM labels then what is the global minimum (solid lines); and (2) what is the mean of all fit results that are within the

1σ critical range of the global χ^2_{red} minimum (dashed lines) The former assumes that by using multiple measured spectra, I can resolve which WGM label set is the most consistent, and therefore correct. The latter is used to assess the variability in the 1σ range of the global χ^2_{red} minimum. I report the error of the fitting as the standard deviation of the difference between the simulated parameter and the resulting fitted parameter. The error in droplet diameter as a function of WGMs used in shown in Figure 3.4. The error in the homogeneous droplet is consistent with the algorithm developed by Preston and Reid[107], which achieved ±2.2 nm with 12 WGMs. The new contribution I added is the error assessment of the core and shell diameters. My error in the shell diameter is similar

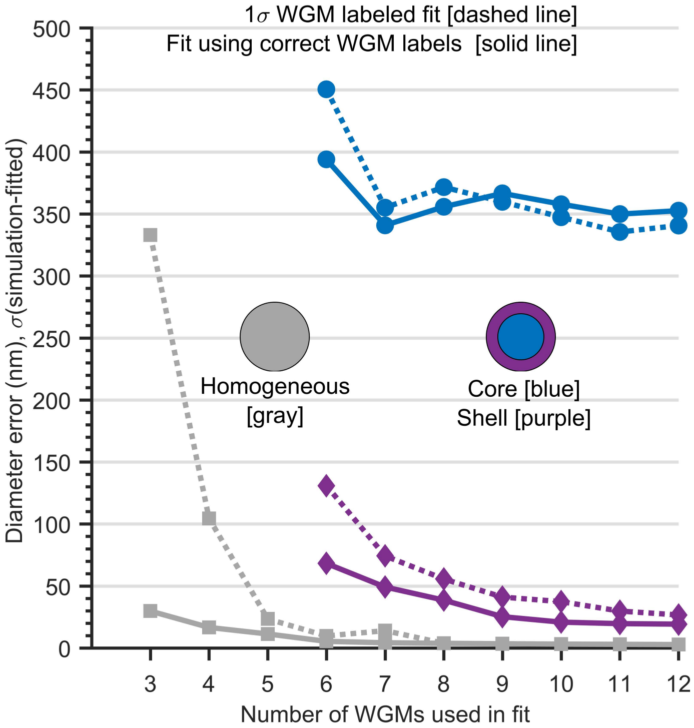

Figure 3.4. The fit error of a homogeneous and core-shell WGMs versus the number of WGMs used in the fitting. The standard deviation is for 300 simulated droplets at each set of WGMs used. The dashed line represents the mean radius of all the fits within 1σ of the global minimum. The solid line is the minimum using the correct WGM labels.

in magnitude to the homogeneous case, but the error in my core diameter (= total diameter – shell thickness) is significantly higher. I attribute the increased error to the additional flexibility in the core-shell model. When I fit experimental data the initial homogeneous droplet fit is used to constrain the possible diameters of the core-shell fit.

I evaluated the error in retrieving the refractive index using the same algorithm to retrieve the diameter. The fitting of the refractive index dispersion model uses two terms to account for the small change in refractive index as a function of wavelength. In Figure 3.5 the error in the first term m_0 is plotted, which for my simulation is equivalent to the

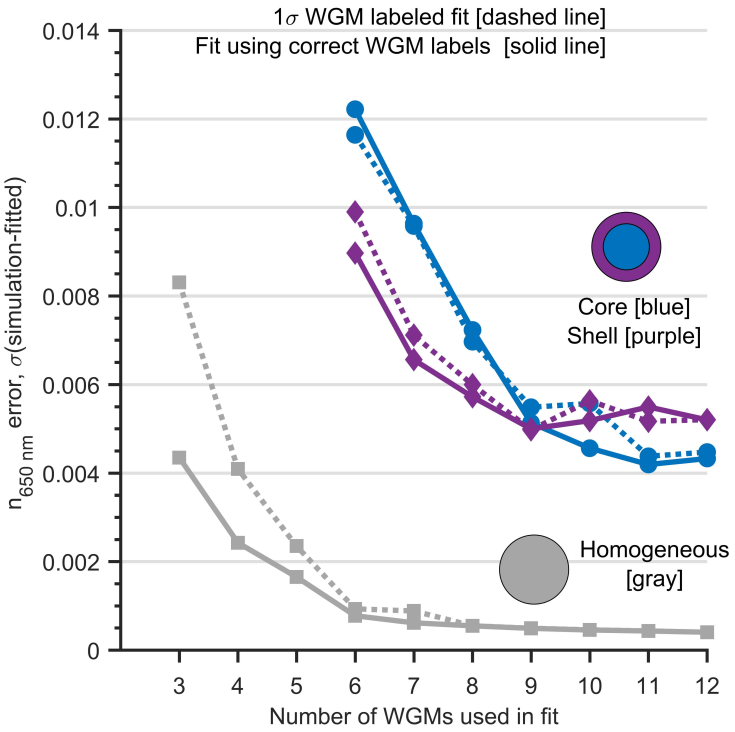

Figure 3.5. The refractive index fit error of a homogeneous and core-shell droplet's WGMs versus the number of WGMs used. The standard deviation is for 300 simulated droplets at each set of WGMs used. The dashed line represents the mean of all the fits within 1σ of the global minimum. The solid line is the minimum using the correct WGM labels.

refractive index at 650 nm, $n_{650\text{ nm}}$. The dispersion term (m_1) plays a necessary, yet minor influence compared to m_0 and d_p. A similar plot of the error for the dispersion term is provided in the Appendix B Figure 8.4. The error in the refractive index for the homogeneous droplet is consistent with Preston and Reid[107], which achieved ±0.00033 with 12 WGMs. In the case of the core-shell droplet, after nine WGMs the level of improvement in the fit with each additional WGM diminishes. I interpret this as reaching the error floor from my simulated noise added to the WGM positions. Some future improvements could incorporate the amplitude of the WGM as well as the width of the WGM, which may further improve the fit accuracy.

There are limitations to fitting of WGMs when only the C-H Raman scattering band is measured (much narrower than the O-H), leading to a fewer WGMs available for the fitting. To still gain some insight into the pure organic systems I use *a priori* information on the refractive index of the core phase to reduce the possibility space, but even then the fits are not as well constrained when compared to systems with the much broader O-H Raman signal. The simulations discussed here focused on the testing the measurements made on the O-H Raman scattering band.

3.5.2 Spectral Response from Adding a Shell of SOA to an Aqueous Inorganic Droplet

I use the addition of α-pinene secondary organic aerosol (SOA) (formed by gas-phase ozonolysis of α-pinene vapor) to an NaCl(aq) droplet to explore how the droplet's Raman spectrum and WGMs transition from a homogeneous droplet to a core-shell droplet as a second phase (the SOA) is added. This experiment, shown in Figure 3.6, clearly demonstrates how the homogeneous fit becomes unrealistic for a core-shell droplet after just a thin shell forms on the droplet. Figure 3.6 also shows the WGM peak

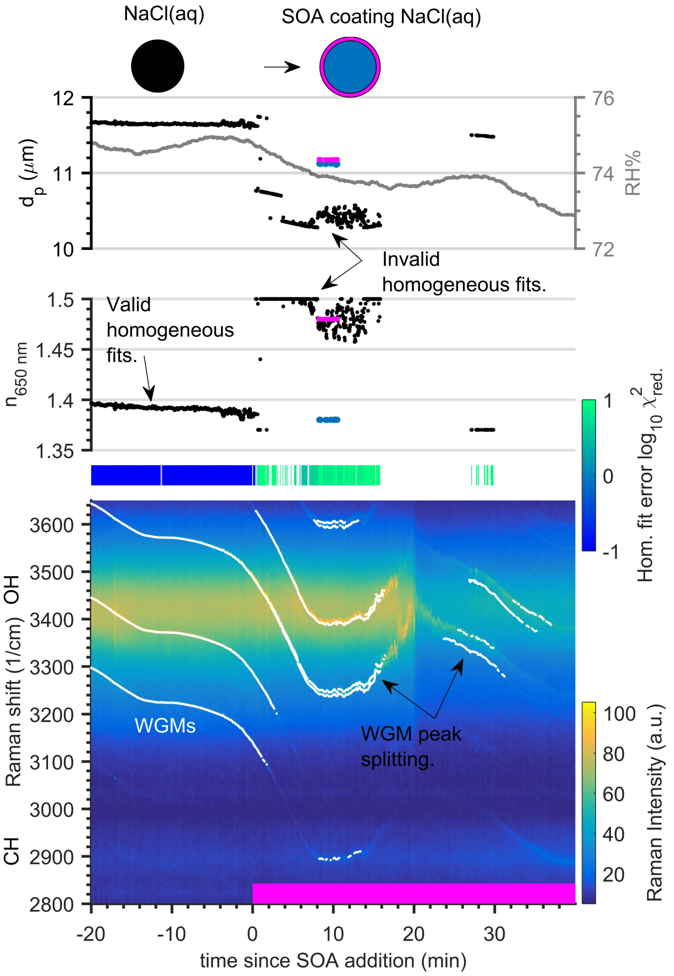

Figure 3.6. Raman spectral time series for a tweezed aqueous NaCl droplet with the addition of α-pinene SOA. Raman spectra are shown in the bottom graph, and the white points indicate the positions of detectable whispering gallery modes (WGMs). The decreasing slope of the WGM traces indicates the droplet is evaporating due to the RH decrease. The α-pinene SOA flow reaction started at 0 min, indicated by the pink bar. The droplet's refractive index and diameter retrieved every two seconds from the WGM analysis are shown in the middle and top panels. The RH is shown in the top right panel. The fit results of the WGM positions to a homogeneous Mie model are in the top two panel as black dots. The fit error for the homogeneous model is shown in the green/blue bar, where consistently blue indicates a valid fit and green indicates an invalid fit to the model. The core-shell fitting is then used to retrieve the properties of the NaCl(aq) core (blue points) and α-pinene SOA shell (pink points) at 10 min.

splitting caused by the growth of a shell on a previously homogeneous core as predicted from the theoretical results shown in Figure 3.2. The experiment began with a trapping NaCl(aq) droplet. I then flowed ozone (3.4 ppm) and α-pinene vapor (182 ppm) into the chamber, forming SOA at t=0 minutes. The majority of the SOA shell growth was caused by coagulation of submicron SOA particles onto the trapped NaCl(aq) droplet. The schematic and methods of my experiment are shown in Appendix B. A detailed assessment of this aerosol system is discussed in Chapter 4. I use the core-shell fit results as guides for this system due to the limited WGMs (6 per frame) and only 24 frames available to fit with the core-shell model. In Figure 3.6 I should also note that the decreasing trend in WGM position is also consistent with the decrease in size observed in the core-shell fit. Lastly, the decreasing intensity of the WGMs after 15 minutes is attributed to a formation of an emulsion of SOA in the aqueous NaCl core discussed in Chapter 4.

3.5.3 Evaporation of an organic core through an organic shell

The ability to measure phase-separated particles and the resulting partitioning between the two phases is investigated using the coagulation of squalane (a hydrophobic molecule) onto an aqueous glycerol droplet. I observed liquid-liquid phase-separation of these two compounds in beaker experiments, so I expect phase-separation in the AOT. The resulting phase-separation morphology remained unknown until in the AOT I observed it to be core-shell as the WGMs persisted[108,109]. In Figure 3.7 I show the core-shell fit results for an isolated part of the experiment after I coagulated the squalane and coagulated additional glycerol to grow the droplet. I used coagulational growth so that the droplet was large enough to identify more than 6 WGMs per frame. The fits shown in Figure 3.7 are for the 270 minutes (6603 data points) where the RH was stable, and therefore composition was constant.

Under these stable RH conditions the core of the droplet is predominantly glycerol, which continuously evaporates into the conditioned air due to its higher vapor pressure, and to a lesser extent the squalane shell also evaporates. This evaporation is reflected in the fit as the diameter of the particle continuously decreases. The average shell refractive index, $n_{650\ \mathrm{nm}}$, was 1.4359 ± 0.0042 which is lower than pure squalane ($n_{589\ \mathrm{nm}}$ = 1.4474 ± 0.0002[140]) meaning a measurable amount of the aqueous glycerol phase partitions to the shell/squalane phase. The refractive indexes are reported at different wavelengths but should still be comparable given that the difference in wavelengths is small and as such the dispersion would only decrease the refractive index by ~0.001 between 589 nm to 650 nm. The core is also not a pure glycerol(aq) solution, but has a higher refractive index with a $n_{650\ \mathrm{nm}}$ = 1.4076 ± 0.0128 whereas the pure glycerol(aq) at 87.3% RH has a $n_{589\ \mathrm{nm}}$ = 1.384 ± 0.008[165]. The higher uncertainty relative to the simulated assessment is likely due to averaging of the simulation results which cover a range of particle compositions and diameters whereas this is a single specific configuration.

Using the retrieved refractive indexes from the core-shell fitting, I can assess the solubility between the two phases. To assess the solubility, I used a volume fraction mixing rule for the refractive indexes[166–169] and assumed the aqueous glycerol component acted as a single phase. These two assumptions are used to simplify the interpretation as

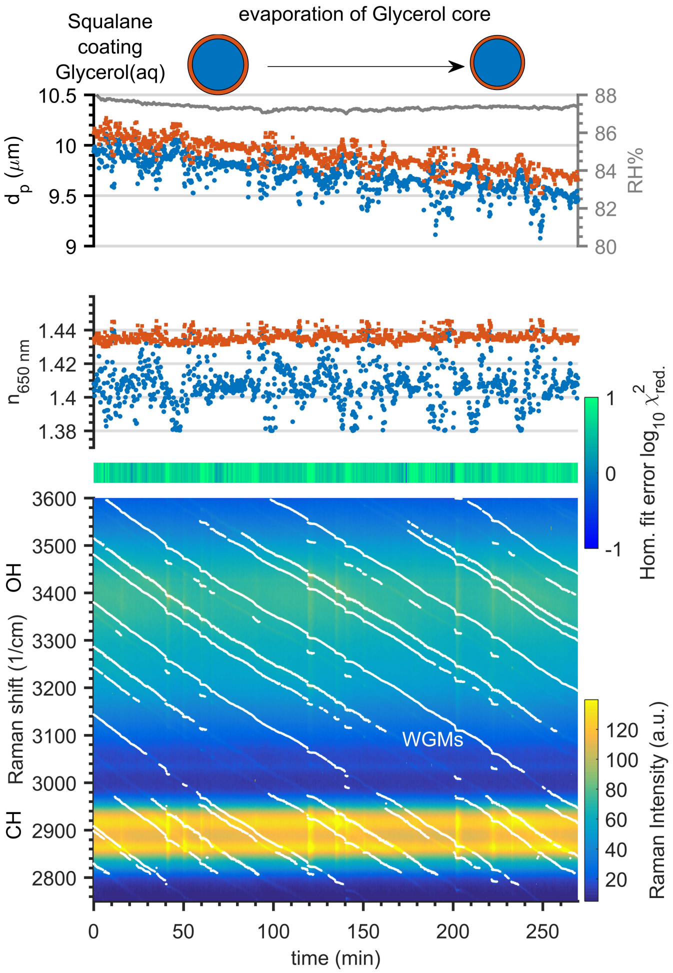

Figure 3.7. Raman spectral time series for a tweezed aqueous glycerol droplet coated with squalane. The panels follow the same format as Figure 3.6. The retrieved two-second data points are averaged to 15 seconds for clarity.

the mixing rules are not the focus of this work, but a more advanced method of treating the three compounds independently as well as using a more accurate mixing rule may be needed in the future. The glycerol(aq) volume fraction in the core was 63% (37% to 95%, range from error in $n_{650\ \mathrm{nm}}$) and in the shell, the glycerol(aq) volume fraction was 18% (10% to 28%). In developing aerosol models for liquid-liquid phase separation, like

AIOMFAC, these AOT experiments are a vital measurement as it informs on both the particle morphology as well as the equilibrium composition of the phases[153].

3.6 Conclusions

I have developed a practical and efficient algorithm for fitting WGMs for a core-shell biphasic droplet. In the process I have added to the understanding of how WGMs change as a second shell phase forms around a previously homogeneous trapped droplet. The major difference in the WGMs from a homogeneous to a core-shell droplet is the peak splitting of adjacent WGMs which was predicted in Figure 3.2 and demonstrated experimentally in Figure 3.6. I then tested my new fitting algorithm on simulated data for a homogeneous droplet achieving accuracies of ±5 nm in particle diameter (d_p) and ±0.00042 in refractive index (n). The same algorithm applied to a simulated core-shell droplets achieved accuracies of ±34 nm in shell d_p, ±359 nm in core d_p, and ±0.0064 in core and shell refractive indices. Using my new algorithm I analyzed an AOT experiment trapping a core-shell droplet of squalane coating glycerol(aq). The retrieved refractive indices of the core and shell phases were used to determine the chemical composition of each phase, finding that there is sparing solubility between each phase. This improved analysis method for core-shell droplets opens the door to future experiments that study the dynamics of phase-separated aerosol in the AOT.

4 Emulsified and liquid-liquid phase separated states of α-pinene secondary organic aerosol determined using aerosol optical tweezers.

Reproduced in part with permission from Environmental Science and Technology, submitted for publication. Unpublished work copyright 2017 American Chemical Society.

4.1 Abstract

I demonstrate for the first time the capture and analysis of secondary organic matter on a droplet suspended in an aerosol optical tweezers (AOT). I examine three initial chemical systems of aqueous NaCl, aqueous glycerol, and squalane at ~ 75% relative humidity. For each system I added α-pinene secondary organic aerosol (SOA) – generated directly in the AOT chamber – to the trapped droplet. I determined the droplet's resulting phase-separated morphology by analyzing the whispering gallery modes (WGMs) in the Raman spectrum. The resulting morphology was always observed to be a core of the original capture droplet's chemical phase surrounded by a shell of the added SOA. When starting with an aqueous NaCl droplet, I also observed a stable emulsion of SOA particles in the aqueous core phase, in addition to the shell of SOA. The persistence of the emulsified SOA particles suspended in the aqueous core suggests that

this metastable state may remain for a significant fraction of the aerosol lifecycle for mixed SOA/aqueous particle systems. By combining the AOT observations of morphology with results from SOA smog chamber experiments, I conclude that the α-pinene SOA shell creates no major diffusion limitations for water, glycerol, and squalane core phases under humid conditions. These experimental results support the current prompt-partitioning framework used to describe organic aerosol in most atmospheric chemical transport models. My AOT experiments also highlight the prominence of phase-separated core-shell morphologies for secondary organic aerosols on a range of core particle chemical phases.

4.2 Introduction

Atmospheric particulate matter is a complex mixture of organic carbon, elemental carbon, and inorganic, metallic, and mineral components, all mixed with a variable amount of water[3,4]. Organic aerosols arise from direct emissions of primary organic aerosol (POA) and from oxidation of precursors – VOCs and evaporated POA – that generates less-volatile secondary organic aerosol (SOA)[5,6]. Complex SOA is a major component of atmospheric organic aerosol, constituting between 30-70% of the total aerosol mass[6,7]. It is composed of thousands of individual organic compounds[8–10]. SOA is a major component of particulate matter, which affects human health and climate change[1,2]. Aerosol optical tweezers (AOT) provide a new analytical technique to explore the composition and the thermodynamic properties of this complex material using isolated suspended droplets and cavity-enhanced Raman spectroscopy.

Liquid particles are common under atmospheric conditions. Depending on the constituents, they can undergo phase separation into distinct chemical phases[29,30,34,35,39,42,109]. I broadly categorize these liquid particles as either homogeneously mixed single-phase structures or liquid-liquid phase separated (LLPS) structures[40,46,54,55,109]. For a phase-separated particle, the two predominant equilibrium states are a core-shell or partially-engulfed arrangement of the phases[36,46–48]. There is also visual evidence from optical microscopy that phase-separation can result in multiple inclusions forming on or in the aqueous phase, producing a complex morphology[26,41]. Recent work by Altaf and Freedman[170] has shown under atmospheric conditions there is a size dependent transition to a homogeneous morphology when particles are <50 nm [99,170,171]. Their observation supports applying the results of phase-separation studies, like this one, to atmospheric particles >50 nm. The cavity-enhanced Raman spectrum retrieved from a droplet trapped in an AOT instrument provides a unique and real-time morphology measurement that can distinguish between these three structures in mixed droplets[108,110,172].

Particle morphology is important. The composition at the air-particle interface dictates the particle's ability to undergo chemical reactions with gas-phase reactants and controls the rates and mechanisms of those reactions[59,63]. N_2O_5 is a key reservoir of nitrogen oxides that demonstrates the importance of this air-particle interface. The reactive uptake coefficient of N_2O_5, $\gamma(N_2O_5)$, governs the N_2O_5 nocturnal removal rate from the atmosphere *via* hydrolysis in aqueous aerosol phases, and a hydrophobic shell on an aqueous core substantially reduces the efficiency of the reactive uptake[14,76]. Reactive uptake also increases aerosol mass loadings through aqueous chemistry, for example with isoprene-derived SOA[78,91].

The Raoult effect can enhance SOA yields when compared to inert SOA seeds[9,95–97]. Ye et al.[97] showed that the Hansen solubility framework could inform the miscibility of α-pinene SOA onto pure component seeds. The general result from these mixing experiments is that highly polar and nonpolar phases do not mix with SOA, while SOA does dissolve into phases of intermediate or mixed polarity. The techniques used in smog chamber experiments can infer phase separation from changes in the aerosol mass yield, aerosol size distribution, or the mixing state of components measured using single-particle analysis. Smog chamber experiments are unable to determine the critical information regarding the resulting particle morphology. For a core-shell morphology, diffusion through the shell could dictate the equilibration rates of molecules partitioning into or out of the particle-phase[50,51,57,58,98]. This shell effect would not be present in a partially-engulfed morphology.

Here I report the first AOT experiments on complex SOA, extending my current understanding regarding the phase separation of SOA using the AOT's ability to distinguish between the three equilibrium morphologies: phase-separated core-shell and partially-engulfed structures, and homogeneous single-phase structures[48,52,54,108–110]. Furthermore, I can observe any changes in the droplet's morphology while its composition changes[108,111,112]. The AOT isolates individual micron-sized droplets freely suspended in air and avoids interference from contact with a surface. It does not require collection of the aerosol onto a substrate followed by solvent extraction required by other methods[19,35,108,173].

4.3 Experimental Methods

4.3.1 *In situ* Ozonolysis of α-pinene in the Aerosol Optical Tweezers

My AOT system was previously described and characterized in Chapter 2[108]. Briefly, a 532 nm laser passes through a set of expansion lenses overfilling the back aperture of a 100x (NA 1.25) oil immersion objective. The objective presses against the bottom of a thin glass coverslip, and an optical gradient force trap forms approximately 40 microns above the coverslip inside the AOT chamber. To generate glycerol and squalane droplets I used a Condensational Monodispersed Aerosol Generator (CMAG; TSI, Inc.) and to generate NaCl(aq) droplets I used a medical nebulizer (PARI TREK S). I control the relative humidity (RH) in the chamber by varying the flow ratio of dry to humidified air and I measure RH at the inlet using a hydrometer (Vaisala).

I used dark ozonolysis of α-pinene vapor to produce SOA directly inside the AOT chamber from the formation of less-volatile oxidation products, some of which homogeneously nucleated to form particles. The gas and particle-phase products then collided with the trapped particle, modifying its composition. A diagram of the experimental setup and a detailed description of the procedural methods are provided in Appendix C.

During a typical ozonolysis experiment, the ozone concentration in the AOT is 55 $\mathrm{ppm_v}$, and the α-pinene vapor concentration is 500 $\mathrm{ppm_v}$, based on the saturated vapor pressure of α-pinene and volumetric flow rates. The ozonolysis of α-pinene proceeds by addition of O_3 to the lone double bond and the reaction is ozone limited under these conditions[174]. This decomposition of the resulting Criegee intermediate goes on to produce ·OH radicals with a yield of ~0.8; under my conditions essentially all of the ·OH reacts with α-pinene[174]. Consequently, the SOA consists of an approximately 0.8:1 mixture of ·OH and ozone oxidation products. I occasionally observe nucleation of detectable particles from the α-pinene oxidation in the form of small-particle light scattering events in the tweezed droplet's visual image. The SOA vapors and particles are produced in the upper section of the AOT chamber and then flow down to the tweezed droplet at the bottom of the AOT chamber. The metal chamber walls do adsorb some of the less volatile SOA components, but these components by necessity are also present in the nucleated particles that coalesce with the tweezed droplet[175].

4.3.2 Raman Spectrum Analysis of Core-Shell Droplets

I use a spectrograph to record Raman scattering from the tweezed droplet, including resonant whispering gallery modes (WGMs). At the wavelength of each WGM, the droplet acts as a high finesse optical cavity where the WGMs form a standing wave near the droplet surface, amplifying the Raman scattering[103,104]. Any radial inhomogeneities in the droplet will weaken the amplification of the WGMs. For partially-engulfed morphologies the WGM amplification process is completely quenched[52,54]. The

WGM amplification process will remain for core-shell morphologies as it is radially symmetric[108,109].

To distinguish the morphology of a core-shell versus a homogeneous droplet, I use a Mie scattering algorithm (Chapter 3) based off the one developed by Preston and Reid[106,107]. When applied to a core-shell droplet I use the plausibility of the retrieved refractive index and diameter parameters as well as an abnormally high fit error to identify a droplet with a core-shell morphology[108,109]. Fitting WGMs of a core-shell droplet to a homogeneous Mie model results in a consistently high fit error. To assess whether the core-shell morphology is valid I have developed a fitting algorithm for the WGMs from a core-shell morphology that retrieves the diameter and refractive index of both the core and shell phases, separately. I provide an accuracy characterization for the core-shell fitting in Appendix C and fully describe the fitting algorithm in Chapter 3.

4.4 Results

4.4.1 Emulsions and Coatings of SOA on an Aqueous Inorganic Droplet

SOA and SOA mimics have been observed to phase separate from an aqueous inorganic phase in large droplets examined visually on microscope slides[37,39,42]. I performed experiments in the AOT on similar systems composed of SOA mixed with aqueous NaCl to determine the conditions under which SOA phase separates from an aqueous phases. I determined the resulting droplet morphology using the cavity-enhanced Raman spectrum retrieved by the AOT and thus avoided interference through contact with any surface. In Figure 4.1 I show an experiment where I added SOA generated *in situ* to a tweezed NaCl(aq) droplet beginning at 0 minutes. I observe typical WGM resonances in the Raman spectrum in the broad O-H water stretch region before the SOA addition (t ≤ 0 min); these correspond to a homogeneous morphology. The

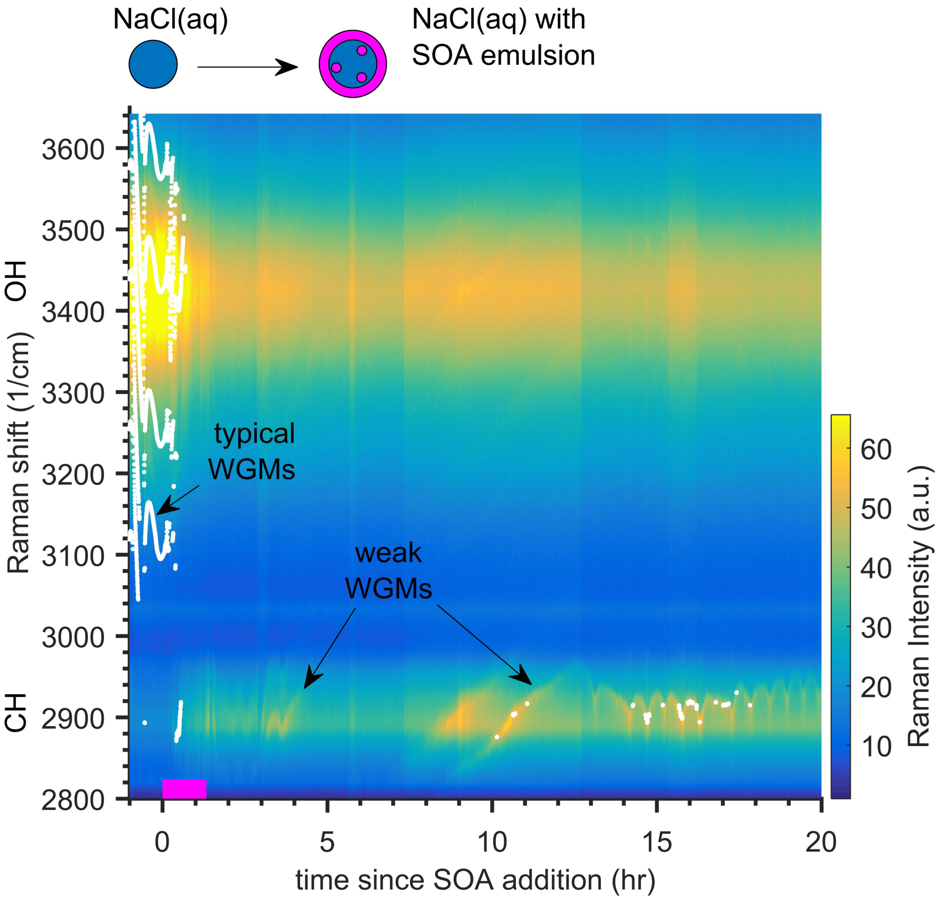

Figure 4.1. Raman spectral time series for a tweezed aqueous NaCl droplet before, during (pink bar at the bottom), and after α-pinene SOA was generated *in situ*, at 78% RH. The C-H hydrocarbon Raman mode center is at 2900 cm^{-1}, the O-H aqueous mode is at 3450 cm^{-1}, and the color scale indicates the intensity of the Raman signal at that Raman shift position. The bright white points indicate the positions of detectable WGMs. The SOA flow reaction started at 0 min and lasted for 1.3 hr, indicated by the pink bar. The weak WGMs following the SOA addition are visible by eye but remain below my peak detection limit for 48 hours; only the first 20 hours are shown here. The small waves (with a period of ~0.5 hr) in the WGMs after 14 hr are caused by small temperature/humidity fluctuations (~1% RH) due to the laboratory's HVAC system.

droplet's size was 7.308 ± 0.001 µm, and its refractive index (n_{650nm}) was 1.380 ± 0.0015 just before SOA addition. During and after the SOA addition, Raman scattering appears in the C-H hydrocarbon region due to the uptake of organic carbon, and weak WGMs are present in both the O-H and C-H Raman regions. The WGMs are weaker following SOA addition but still faintly visible in the Raman spectrum's time series; their intensity is diminished but not completely quenched.

The persistence of weak WGMs following addition of SOA to an aqueous NaCl drop means I cannot conclude that the mixed droplet formed a partially-engulfed structure, because that would completely quench the WGMs. Theoretical modeling of a spherical droplet with an emulsion showed that as the number of emulsified particles increased the WGMs are weakened and become broader, which would be consistent with my observations[176]. The heterogeneities in the radial path of the resonating wavelengths of light would scatter the resonating WGM and intermittently quench the WGM signal. Some possible configurations of these heterogeneities are shown in the Appendix C Figure 9.3; they are all classified as a type of emulsion. As I observe some WGM amplification, I propose that the droplet consists of a homogeneous SOA shell coating a supermicron aqueous NaCl core containing emulsified SOA particles retained during the coalescence of SOA particles onto the tweezed droplet. Along with the emulsion, the more polar compounds in the SOA are water soluble, so a small fraction of the SOA should also dissolve into the aqueous phase. Two-dimensional microscopy images in the literature support this proposed shell phase with an emulsion of SOA in an aqueous core[37,39,42]. However, it is difficult to resolve the 3-dimensional morphology from those microscopy images because they only show one viewing angle. This is not a limitation of the AOT. In the Appendix C, I demonstrate that radial heterogeneities can weaken the WGM amplification by coagulating NaCl crystals onto a trapped squalane droplet. This supports my SOA emulsion interpretation of the Raman spectrum in Figure 4.1.

To further test my emulsion hypothesis, I waited for 48 hours (the first 20 hours are shown in Figure 4.1) to see if the emulsion would relax (Ostwald ripening) since emulsified particles represent a metastable state[177]. I continued the flow of humidified clean air to maintain the aqueous phase, so semi-volatile SOA should have evaporated to some extent from the droplet. The relatively stable WGM positions with time (Figure 4.1, 10 to 20 hours) shows that the droplet diameter remained nearly constant, indicating the remaining SOA did not evaporate to a noticeable extent.

In a second experiment on the same SOA + NaCl(aq) aerosol system, I used an RH cycle on the emulsified core-shell droplet to test the effect of dehydrating the aqueous core (which presumably contained the emulsified particles), as this might promote demulsification. The initial aqueous NaCl droplet was 8.522 ± 0.001 μm with an $n_{650\text{nm}}$ of 1.376 ± 0.0015, after which I added the SOA. I subsequently cycled the RH from 80% down to 55% and then back up to 79%. After the RH decreased at 224 min, 4 or 6 relatively strong WGMs appeared in the spectrum. The spectra during the drier period also exhibit more typical WGM amplification. After I increased the RH back up to 79% at 235 min, the strong WGMs typical of a homogeneous spherical geometry intensified, with 6 or more strong WGMs visible in a 2-second frame. Isolated Raman spectra covering this transition period are provided in Appendix C Figure 9.2.

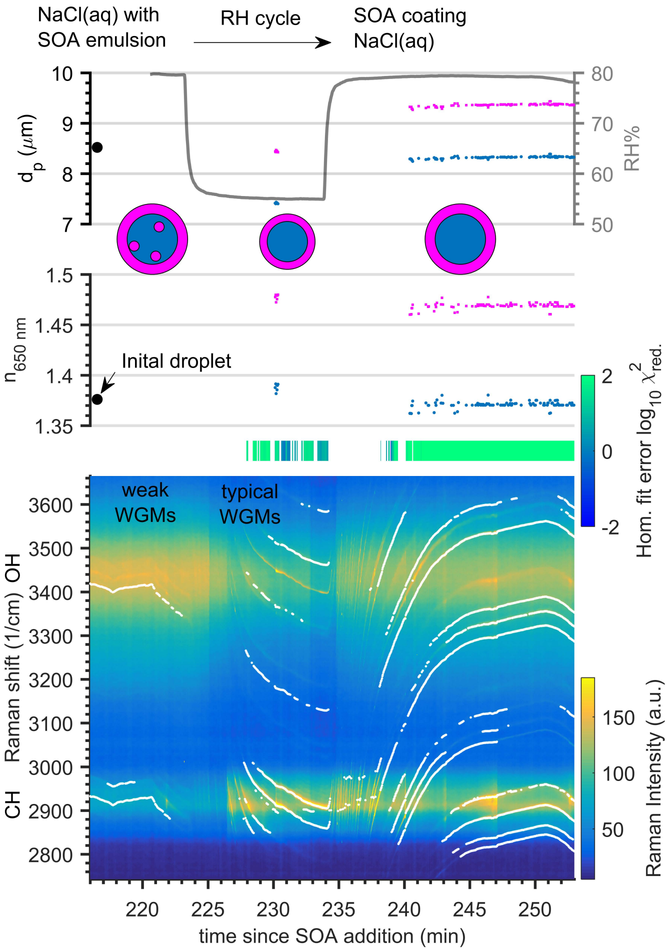

Figure 4.2. Raman spectra time series for a tweezed aqueous NaCl droplet after coagulation with α-pinene SOA, undergoing a relative humidity (RH) cycle. The bottom graph is the time series of the Raman spectra, the middle is the refractive index at 650 nm, and the top is the droplet diameter (left axis) and conditioning air's relative humidity (right axis). The time series started after the α-pinene SOA addition which happened at 0 min and lasted for 65 min. The initial homogeneous NaCl droplet fit results are shown as black circles. WGMs that meet the peak criteria are shown as white points/lines in the Raman spectral time series. The fit error for the homogeneous morphology model is shown in the green/blue bar, where consistently green indicates an invalid fit to the homogeneous model. The fitted core-shell droplet diameter and refractive index are shown above for both the core (blue dots) and shell (pink dots) phases. The retrieved $n_{650\mathrm{nm}}$ values are consistent with a core of NaCl(aq) and a shell of α-pinene SOA. The morphologies I infer during this experiment are displayed where an emulsion of SOA in the aqueous core is relaxed to a core-shell morphology via the RH cycle.

When I fit the WGMs after the RH cycle with the homogeneous Mie model appropriate for a single phase, the results are inconsistent and have high fit error, $\log_{10}(\chi^2_{red}) > 0$ (blue/green bar in). When I fit the WGMs using the core-shell Mie model the results are consistent with what I would expect based on the initial conditions, the RH cycling, and the starting droplet size, shown in Figure 4.2. The refractive index of the α-pinene SOA shell ($n_{650\text{nm}}$ = 1.469 ± 0.004) is well within the range reported in the literature ($n_{532\text{nm}}$ = 1.39-1.52); see Appendix C for a comparative table[178–182]. The core refractive index, $n_{650\text{nm}}$, of 1.372 ± 0.005 is within the error of the initial droplet ($n_{650\text{nm}}$ = 1.376 ± 0.0015), suggesting that no measurable SOA dissolved into the core. The solution has a NaCl mole fraction of 0.16, calculated via E-AIM[10,183]. By using a volume fraction mixing rule for the core refractive index this means the volume fraction of SOA in the core is less than 4.3%. The droplet size is quite stable, as shown in the; though the WGM positions after the RH cycle at 235 min do change with time, 3 cm^{-1} corresponds to roughly 1 nm in diameter, so the growth is a fraction of a micrometer. The core-shell fit results support a morphology where α-pinene SOA coats the NaCl(aq) core. Based on these results I conclude that coalescence of submicron SOA particles onto a high ionic strength aqueous NaCl droplet results in a droplet coated with a spherical shell but containing emulsified SOA particles as well. The subsequent RH cycle transitioned the droplet to an equilibrium core-shell droplet with an SOA shell, no residual emulsified SOA, and little dissolved SOA.

4.4.2 Morphology of an Aqueous-Organic Mixed Droplet

A natural extension of SOA coalescence to an aqueous inorganic core is SOA coalescence to an aqueous-organic core. In this way, I can isolate the role of water in the phase separation and remove the salting out effect of the relatively high ionic strength aqueous inorganic solution. I use glycerol as it is hygroscopic and is active in both the C-H and O-H Raman modes.

I trapped a glycerol droplet at 73% RH, finding $n_{650\mathrm{nm}}$ of 1.4314 ± 0.0013 with a homogeneous Mie model. In Figure 4.3 it is apparent that, before the α-pinene SOA addition at $t = 0$, the droplet was shrinking rapidly. The retrieved diameter and the negative slope of the WGM positions indicate evaporation of the glycerol (water volume fraction should remain constant because of the constant RH). When I added α-pinene SOA to the droplet, the homogeneous Mie fitting of the WGMs failed immediately, as indicated by the increased fit error of the homogeneous model. However, the core-shell Mie model could successfully fit the WGMs both during and after the SOA addition. The core-shell refractive index results indicate that a shell of α-pinene SOA ($n_{650\mathrm{nm}} = 1.474 \pm 0.005$) coated the glycerol(aq) core ($n_{650\mathrm{nm}} = 1.4325 \pm 0.007$). The refractive index of the SOA shell is consistent with the NaCl(aq) experiment described above and within the literature range (summarized in Appendix C). As with the high ionic strength NaCl(aq) droplet, I observed no measurable dissolution of the SOA into the aqueous organic core; the volume fraction of SOA in the aqueous glycerol solution was < 17% based on the measured $n_{650\mathrm{nm}}$. In contrast to the NaCl(aq) system, I do not observe evidence of an emulsion, as strong WGMs persisted throughout the experiment.

The continued evaporation of the core indicates that the α-pinene SOA did not prevent or retard evaporation of glycerol from the core. The measured evaporation rate for the glycerol(aq) core decreased by 22% after I added the α-pinene SOA. This decrease

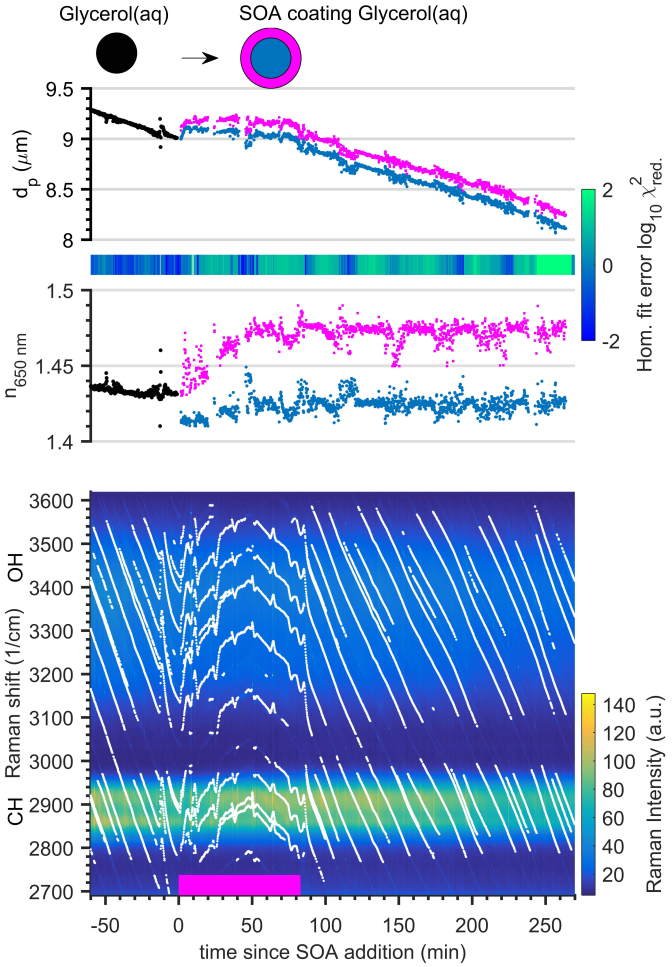

Figure 4.3. Raman spectral time series for a tweezed aqueous glycerol droplet with the addition of α-pinene SOA, at 73% RH. Raman spectra are shown in the bottom graph, and the white points indicate the positions of detectable whispering gallery modes (WGMs). The decreasing slope of the WGM traces indicates the droplet is evaporating. The α-pinene SOA flow reaction started at 0 min and lasted for 80 min, indicated by the pink bar. The droplet's refractive index and diameter retrieved from the WGM analysis are shown in the middle and top panels. The fit results of the WGM positions to a homogeneous Mie model are in the top two plots as black dots. The fit error for the homogeneous model is shown in the green/blue bar, where consistently blue indicates a valid fit and green indicates an invalid fit to the model. The core-shell fitting is then used to retrieve the properties of the glycerol(aq) core (blue points) and α-pinene SOA shell (pink points) after SOA generation started at 0 min.

could be due to Raoult's Law of SOA mixing in the glycerol(aq) core depressing the overall evaporation rate of the core. That decrease could also be due to a diffusion limitation of glycerol through the SOA shell. If the SOA dissolved in the core was at my upper limit of 17% by volume, Raoult's Law may explain the majority of the decrease in evaporation rate. I will systematically explore these confounding effects of mixing and diffusion limitations in the glycerol plus SOA system in future experiments by varying the amount of SOA added to the droplet. One thing that is clear from this experiment is that the SOA shell does not trap glycerol in the SOA phase and does not prevent glycerol from partitioning to the gas phase.

I can also use the evolution of the shell thickness, as shown in Figure 4.3, to calculate the evaporation rate and thus the effective vapor pressure of the SOA shell. To do this, I calculated the volume loss of the shell for the period between 160 min. and 260 min. and assumed an SOA molecular weight of 300 g/mol and a density of 1.4 g/cm^3 [88,184,185]. There was very little evaporation, and so the effective vapor pressure of the SOA shell was 5.2×10^{-6} Pa or equivalently a C^* of 0.64 μg/m^3 ($10^{-0.193}$ μg/m^3)[111,139,175,186].

This retrieved volatility is higher due to my high precursor conditions than the measurements made during the α-pinene SOA evaporation experiment described by Yli-Juuti et al.[187], with $C^* \simeq 10^{-3}$ μg/m^3 at 80% RH. Lastly, in contrast to typical SOA evaporation experiments, my shell phase does not appear to contain a large portion of intermediate-volatile organic carbon with higher C^* values as the evaporation rate I observed was constant. This could be due to additional aqueous chemistry of the SOA at the aqueous-core interface, leading to lower volatility SOA in the shell phase[188].

4.4.3 Morphology of SOA Added to a Hydrophobic Organic Droplet

Having studied two aqueous cores, next I studied the mixing of SOA with a tweezed hydrophobic squalane ($C_{30}H_{62}$) droplet. My objective was to replicate the chemical system studied in a smog-chamber mixing experiment conducted by Robinson et al.[9]. They studied the same particle system by condensing α-pinene ozonolysis SOA onto squalane seed particles and also condensing squalane vapors from a heated injector onto SOA particles. After increasing the chamber temperature by 22 °C, they observed rapid evaporation of the squalane and little evaporation of the SOA. They also found that squalane and α-pinene SOA remained phase-separated during a particle mixing experiment. Based on these experiments they concluded that the mixed particles formed a two-phase morphology, noting that if the particles had a core-shell morphology with the squalane forming the core, the evaporating squalane would have to diffuse relatively rapidly through the SOA shell. That single-particle smog-chamber experiment could not fully constrain the phase-separated particle morphology, leaving the hypothesis that squalane can diffuse rapidly through SOA unproven. If the morphology were partially-engulfed, then squalane would have direct access to the gas phase. The aerosol optical tweezers provide a unique way to determine the morphology of this complex system directly.

In Figure 4.4 I show spectra from an experiment starting with a pure squalane droplet, with an initial diameter of 8.492 ± 0.004 μm and a refractive index, $n_{650\text{nm}}$, of 1.447 ± 0.001, to which I added α-pinene SOA by coagulation. The WGMs were initially almost horizontal, with a slight negative slope due to the slow evaporation of squalane, which has an estimated vapor pressure of 1.93×10^{-6} Pa[189]. When I began to add α-pinene SOA, the WGM slopes became strongly positive, indicating that the particle was growing. The persistence of the WGMs also indicates that the SOA spread rapidly across the squalane surface as it condensed and coagulated, excluding a partially-engulfed morphology. After the α-pinene SOA addition at 70 min, I held the chamber static with all airflows off before turning on clean airflow at 80 min; the droplet then began to shrink, indicated by the negative slope of the WGMs. The fit results for the core-shell droplet are sparse because the droplet contains mostly C-H bonds, which have a narrow Raman band reducing the number of WGMs observed. However, the few fits are consistent with a squalane core coated by SOA. Moreover, the slope of the WGMs at the end of the experiment is similar to the slope at the beginning, suggesting that slow squalane evaporation (few nm per minute) dominates the particle evolution. The slightly higher slope soon after the SOA addition also suggests that some SOA evaporated from the shell.

Consistently high homogeneous Mie fit error following the addition of α-pinene SOA indicates that the droplet was not homogeneous, while the persistence of the WGMs rules out a partially–engulfed morphology. Based on this evidence I conclude that the droplet was phase separated, which is consistent with smog-chamber studies[9,97]. My AOT results add the additional insight that the particle morphology is core-shell with α-pinene SOA coating squalane. This direct measurement of the morphology is inaccessible from traditional smog chamber observations of a large ensemble of particles. The core

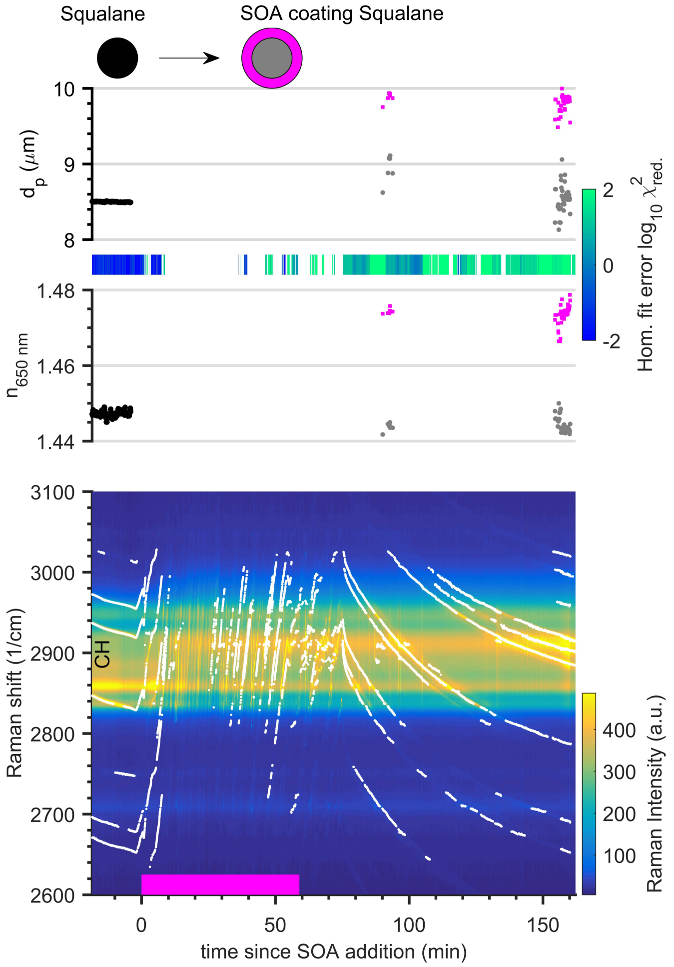

Figure 4.4. Raman spectral time series for a tweezed squalane droplet and addition of α-pinene SOA, at 80% RH, following the same format as in Figure 4.3. A decreasing trend of the WGM traces indicates the droplet was evaporating whereas an increase indicates droplet growth. The α-pinene SOA addition started at 0 min. and lasted for 60 min., indicated by the pink bar. The fit results of the WGM positions to a homogeneous model are shown in the top two plots as black dots. The core-shell fitting model is then used to retrieve the properties of the squalane core (gray) and α-pinene SOA shell (pink) following SOA addition. Few WGMs are retrieved as the C-H hydrocarbon band is too narrow to consistently contain at least 6 WGMs that are required for the core-shell Mie fit.

refractive index, n_{650nm}, of 1.444 ± 0.003 and diameter of 8.577 ± 0.186 μm provide evidence that no measurable amount of SOA was dissolved into the core (volume fraction < 11%). The retrieved refractive index of the α-pinene SOA shell (n_{650nm} = 1.473 ± 0.003) is consistent with the previous two experiments on aqueous NaCl and glycerol.

Note that squalane lacks any unsaturated bonds for ozone to attack. Squalane can be oxidized by the ·OH radicals produced by the ozonolysis of α-pinene, but this heterogeneous oxidation would be much slower than the gas-phase oxidation of α-pinene by ·OH due to mass transfer limitations from the gas phase to particle interface[190]. The squalane core also quickly became protected by the SOA coating.

4.5 Discussion

My extension of the AOT technique to generate and study complex α-pinene SOA *in situ* enables real-time investigations of complex aerosol systems at the individual particle level that more realistically mimic atmospheric aerosol compositions. Fitting of the WGMs provides highly accurate measurements of the droplet's size and refractive index that allow us to determine how different droplet compositions respond to the addition of SOA. The sequence of liquid-liquid phase separation experiments demonstrates that such phase separations are common for the aerosol mimics probed here, including mixtures of aqueous organic, aqueous inorganic, or hydrophobic organic particle phases with SOA. I also add further evidence to indicate that core-shell morphologies are common structures for complex mixed atmospheric aerosol mimics[44,55]. My work here focused on high humidity ranges of 70% to 80% RH to isolate the effect of the starting droplet composition; in Chapter 5, I will explore the effect of RH on the resulting phase-separation morphology. The high precursor concentrations used here are not representative of the ambient troposphere, and as such may affect my resulting SOA oxidative state and volatility. This high precursor effect appears to have shifted my SOA volatilty higher as my measured SOA volatility was higher then observed in an evaporation experiment by Yli-Juuti et al.[187]. These AOT experiments on *in situ* generated α-pinene SOA avoids limitations brought about in other measurements of phase separation and morphology that use SOA filter extracts where the solvent can alter the composition and only extracts the soluble portion, such as the water-soluble fraction of SOA[26,191–193].

Through the core-shell fitting of my different SOA systems, I also retrieve the refractive index to a 0.4% accuracy. My retrieved refractive index is valuable as previous optical closure studies on SOA systems yielded a wide range of refractive indices. The variability is in part due to the methods used where a new volume of particles is measured at each data point. In the AOT the environment is more controlled, and I measure the properties of the same SOA mass in real-time, which reduces experimental variability between measurements.

Synthesizing the results from the different RH stages of the aqueous NaCl droplet plus SOA experiment strengthens my proposal for the emulsion of SOA particles in the aqueous core. Dehydration of the aqueous core demulsified the SOA and produced a stable irreversible core-shell morphology of SOA coating the NaCl(aq). From this, I can conclude that the core-shell morphology observed is the thermodynamically stable condition for this mixed system, and the emulsion was metastable. Therefore, before the RH cycle, it is likely that a core-shell morphology was thermodynamically favored then as well. Finally, a droplet morphology composed of a homogenous SOA shell and the inhomogeneous core of emulsified SOA particles in aqueous NaCl would also explain the diminished WGM amplification observed. As this homogeneous shell and inhomogeneous core would account for the resonance of WGMs in the surface layer of the SOA shell, while not permitting the full amplification of the WGMs due to interference by the emulsion in the core. Presumably, when the core's volume decreases at the lower RH, these metastable emulsified SOA particles were efficiently added to the principle SOA phase that constitutes the shell, promoting demulsification. It is also notable that the SOA appears to be relatively insoluble in this aqueous solution, even though isolated α-pinene SOA is known to be reasonably hygroscopic[194]. If the solubility of SOA is greatly diminished in mixed composition particles (which pervade the atmosphere) this has significant implications for CCN activity of these particles; the aqueous solution will be much more dilute at the Köhler maximum in the droplet growth curve under supersaturated conditions than at 80% RH.

The glycerol(aq) plus SOA experiment is especially interesting when taken into the context of the NaCl(aq) plus SOA experiment. First, it shows that the phase separation in the NaCl(aq) plus SOA case is not principally driven by a salting out effect. Second, both experiments added SOA to an aqueous droplet, but the NaCl(aq) system formed an emulsion in the core whereas the glycerol(aq) did not. The physical formation of the emulsion is due to SOA particles coagulating onto the surface of the droplet, but that does not explain why it is a stable emulsion as shown in Figure 4.1. The same coagulation of homogeneously nucleated SOA is occurring with the glycerol(aq) droplet yet for that system SOA promptly starts to form a coating without creating an emulsion. In the atmosphere, this emulsified state would increase exposed SOA surface area to the aqueous medium and thus give more SOA a chance to undergo aqueous chemistry. The prevalence of the SOA emulsion may be limited to high number concentration regimes where coagulation is significant, such as new particle formation events that frequently occur, particularly near forested regions with high biogenic VOC emissions[192,195]. It would also delay the formation of a stable core-shell morphology where all the undissolved SOA resides at the air-particle interface. Considering my observations of a stable emulsified state for 48 hours, RH cycling in the atmosphere may play an important role in determining the morphology of mixed SOA and aqueous inorganic particles, and prevalent atmospheric particle mixing state.

The AOT experiment on the α-pinene SOA coating squalane system refines the interpretation of smog-chamber experiments reported by Robinson et al.[9]. They also observed phase separation of squalane and SOA, which my AOT experiments confirm. My experiment provides the additional observation that the phase-separated particle is a core-shell morphology, an important property that was unobservable in the smog chamber experiments. I have determined that a shell of α-pinene SOA surrounding the squalane core is the thermodynamically stable state for this mixture. Now I can definitively interpret the results from the aerosol evaporation experiments performed by Robinson et al.[9]. They observed prompt evaporation of squalane (which is more volatile than the oxidized SOA) which could indicate that the diffusion coefficient of the squalane in SOA phase is sufficiently high to promote the transport of squalane through the SOA as it evaporates. This interpretation requires the SOA to be coating the squalane phase, which my AOT experiments now confirm is the equilibrium morphology. Combining the results from my AOT experiments and their chamber experiments I can conclude that squalane has no major diffusion limitation through α-pinene SOA. I can also add my additional observations of glycerol evaporating through the SOA shell in Figure 4.3. From the glycerol experiment, I conclude that glycerol has no major diffusion limitation through α-pinene SOA. Finally, from the rapid WGM response to the RH cycle of the SOA coating an NaCl(aq) droplet, I conclude that water also has no major diffusion limitation through α-pinene SOA. If these results hold for other OA systems then assuming prompt partitioning under moderate humidities in atmospheric chemical transport models is valid when the model time steps are on the order of minutes[98,175,196–198]. A companion paper (Chapter 5) will explore in detail the physical properties of the SOA observed from these and additional AOT experiments, such as the volatility, diffusivity, viscosity, and surface tension of the SOA.

5 The morphologies of α-pinene secondary organic aerosol determined at low humidity using aerosol optical tweezers

5.1 Abstract

I highlight the prominence of phase-separated, core-shell morphologies for secondary organic aerosol through a series of aerosol optical tweezers (AOT) experiments. I explored the relative humidity (RH) dependence of α-pinene SOA phase-separation from squalane and glycerol phases. For α-pinene SOA added to a squalane droplet I observed no change in the core-shell morphology from 75% RH to 12% RH. From the observed persistent core-shell morphology, I can conclude that the surface tension of the *in situ* generated α-pinene SOA was always < 28 mN/m, the surface tension of squalane. I used trends in interfacial tensions between aqueous and organic phases to conclude that a core-shell morphology – with the organic phase coating the aqueous core – would be the most common morphology for phase-separated particles in the atmosphere. I did observe a humidity dependence for the solubility of α-pinene SOA in glycerol. At 12% RH, the glycerol plus SOA droplet was homogeneous, which is in contrast to the core-shell morphology observed at 75% RH. The RH-dependent phase-separation and morphology is caused by changes in the polarity of the glycerol phase as

its water content changes due to hygroscopic growth at elevated RH. This work points out the need to understand how surface tension and more importantly interfacial tension is related to commonly measured ambient aerosol properties such as oxidation state and the O:C atomic ratio. To predict phase-separation morphologies for organic-organic systems, a better understanding of molecular structure, and its resulting impact on interfacial and surface tension is required.

5.2 Introduction

Organic aerosols originate from direct emissions of primary organic aerosol (POA) and from the oxidation of precursors – VOCs and evaporated POA – that generates less-volatile secondary organic aerosol (SOA)[5,6]. SOA is composed of thousands of individual organic compounds and is a major component of atmospheric organic aerosol, constituting between 30-70% of the total aerosol mass[6–10]. More broadly atmospheric particulate matter is a mixture of organic carbon, elemental carbon, and inorganic, metallic, and mineral components, all mixed with a variable amount of water[3,4]. SOA is a major component of particulate matter, which affects human health and climate change[1,2].

In the atmosphere, the gas phase environment is constantly changing, causing aerosol components such as water and volatile organics to become enriched or diluted. Of particular interest for this study is how changes in relative humidity affect aerosol morphology. The aerosol optical tweezers (AOT) is used to explore the composition and the thermodynamic properties of SOA using isolated suspended droplets and cavity-enhanced Raman spectroscopy.

Liquid particles are common under atmospheric conditions. Depending on the constituents, they can undergo phase separation into distinct chemical phases[29,30,34,35,39,42,109]. I broadly categorize these liquid particles as either homogeneously mixed single-phase structures or liquid-liquid phase separated (LLPS) structures[40,46,54,55,109]. For a phase-separated particle, the two predominant equilibrium states are a core-shell or partially-engulfed arrangement of the phases[36,46–48]. The cavity-enhanced Raman spectrum retrieved from a droplet trapped in the AOT instrument provides a unique and real-time morphology measurement that can distinguish between these three structures in mixed droplets[108,110,172]. My previous study (Chapter 4) had focused at high relative humidities, e.g. ~75%; here I am extending this work to investigate the morphology of SOA under low relative humidity[199].

5.3 Methods

I previously described and characterized my AOT system in Gorkowski et al. (Chapter 2)[108]. Briefly, a 532 nm laser passes through a set of expansion lenses overfilling the back aperture of a 100x (NA 1.25) oil immersion objective. The objective presses against the bottom of a thin glass coverslip, and an optical gradient force trap forms approximately 40 microns above the coverslip inside the AOT chamber. To generate glycerol and squalane droplets, I use a Condensational Monodisperse Aerosol Generator

(CMAG; TSI, Inc.). I control the RH in the chamber by varying the flow ratio of dry to humidified air and I measure RH at the inlet using a hydrometer (Vaisala).

I used dark ozonolysis of α-pinene vapor to produce SOA directly inside the AOT chamber from the formation of less-volatile oxidation products, some of which homogeneously nucleated to form particles. The gas and particle-phase products then collided with the trapped particle, modifying its composition. During a typical ozonolysis experiment, the ozone concentration in the AOT is 55 ppm_v, and the α-pinene vapor concentration is 500 ppm_v, based on the saturated vapor pressure of α-pinene and volumetric flow rates. This method has been previously explained in detail in Chapter 4.

5.3.1 Raman Spectrum Analysis of Core-Shell Droplets

I use a spectrograph to record the Raman scattered light from the tweezed droplet, including resonant whispering gallery modes (WGMs). At the wavelength of each WGM, the droplet acts as a high finesse optical cavity where the WGMs form a standing wave near the droplet surface, amplifying the Raman scattering[103,104]. Any radial inhomogeneities in the droplet will weaken the amplification of the WGMs. For partially-engulfed morphologies, the WGM amplification process is completely quenched [52,54]. The WGMs will remain for core-shell morphologies as it is radially symmetric[108,109].

To distinguish the morphology of a core-shell versus a homogeneous droplet, I used an inverse algorithm based off the one developed by Preston and Reid[106,107]. When applied to a core-shell droplet I used the plausibility of the retrieved refractive index and diameter parameters as well as an abnormally high fit error to identify a droplet with a core-shell morphology[108,109]. Fitting WGMs of a core-shell droplet to a homogeneous Mie model results in a consistently high fit error. To assess whether the core-shell morphology is valid I have developed a fitting algorithm for the WGMs that retrieves the diameter and refractive index of both the core and shell phases, separately (Chapter 3). There are limitations to the fitting of the WGMs when only the hydrocarbon C-H Raman scattering mode is measured. The C-H Raman mode is narrower and more complex leading to fewer WGMs available to fit. To still gain insight into the pure organic systems I use *a priori* information on the refractive indexes of the core phase to reduce the parameter space, but even then the fits are not well constrained when compared to systems that contain the broader water O-H Raman mode that supports more WGMs to fit to.

5.4 Results

5.4.1 Morphology at Dry Conditions of SOA Added to a Hydrophobic Organic Droplet

In my previous work investigating α-pinene SOA in the AOT, I saw that the WGMs remained during the coagulation of SOA to a squalane droplet. I performed that experiment at 80% RH, which due to the plasticizing effects of water should reduce any viscous limitations to mass transfer or spreading imposed by the ~200 nm SOA particles coalescing to the surface of the droplet. In these new experiments, to maximize any viscous limitations I trapped a squalane droplet and proceeded to add α-pinene SOA while my chamber was at 12.5% RH. In my previous experiments on squalane with α-pinene SOA (Figure 4.4), I identified that the morphology was core-shell with the SOA forming the shell. The new low RH experiments reported here probe if the droplet's morphology changes as humidity changes. As both squalane and α-pinene SOA have low hygroscopicities, I wouldn't expect a major change in surface tension and therefore morphology with humidity.

I performed two types of experiments probing the morphology of squalane and α-pinene SOA. In the first, SOA was produced in the AOT chamber at 12.5% RH (shown in Figure 5.1), and in the second the SOA was formed at 75% RH and then the RH was reduced to 13% RH (shown in Figure 5.2).

In Figure 5.1 I focus on the observation that the WGMs remain during the coagulation of the SOA with the squalane droplet coagulation. The full time-series is shown in the supplemental information, for clarity only an isolated transition period is shown in Figure 5.1. Due to the narrow nature of the C-H hydrocarbon Raman band, I did not identify enough WGMs (6 or more) for a successful core-shell fit. The WGMs remain visible by eye in the Raman spectra, but in this experiment my peak finding method could not reliably sort out the false positives from the real WGM peaks. In Appendix D, I show the homogeneous Mie fit, which shows an increase in fit error after the SOA addition is started. This increase in fit error is characteristic of the formation of a core-shell morphology where the added SOA forms the shell (Chapter 2). If SOA had formed the core, then the WGMs would still fit a homogeneous model as WGMs are only present on the outer surface of the droplet, ~10% of the droplet's outer radius for the 1st mode order WGMs (Chapter 3).

I used the morphology of SOA coating squalane in my interpretation of the WGMs during the coagulation period. The constant presence of the WGMs means the droplet retained the spherical symmetry during the SOA coagulation. Thus the SOA particles are rapidly spreading over the surface. The rapid spreading is indicative of a liquid like behavior, as glassy (solid) particles would disrupt the WGM amplification. This liquid like behavior at low RHs for α-pinene SOA is in contrast to previous conclusions in the literature[50,51,59,60]. This difference could be due to my high SOA aerosol mass concentrations produced during the *in situ* SOA production. This shifts the volatility

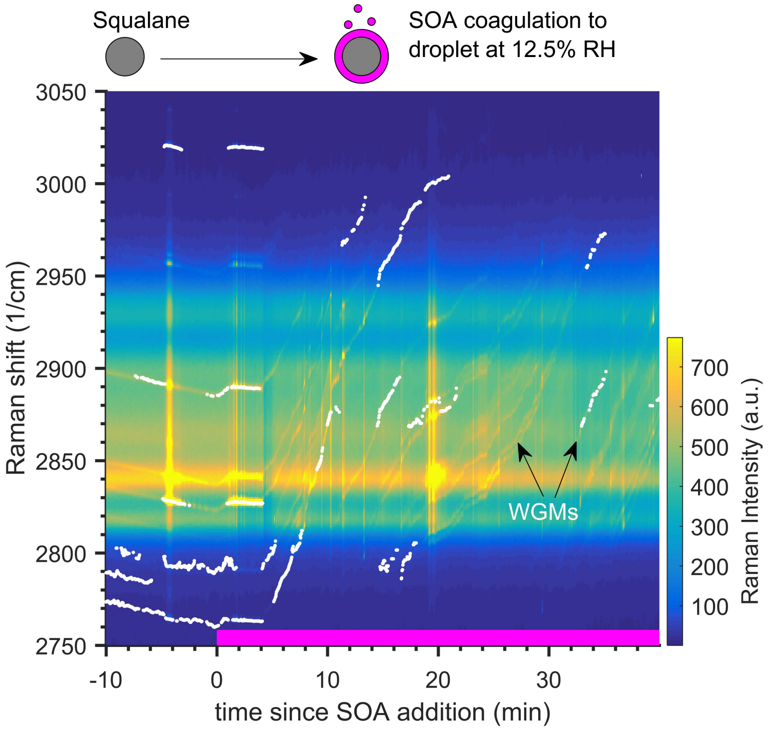

Figure 5.1. Raman spectral time series for a tweezed aqueous squalane droplet before, and during (pink bar at the bottom) α-pinene SOA was generated *in situ*, at 12.5% RH. See the supplemental information for the full time-series. The C-H hydrocarbon Raman mode center is at 2900 cm^{-1}, and the color scale indicates the intensity of the Raman signal at that Raman shift position. The bright white points indicate the positions of detectable WGMs. The SOA flow reaction started at 0 min, indicated by the pink bar. The WGMs remain during the coagulation of SOA to the droplet.

range of the SOA products that partitioned to the particle phase to a higher range, which would result in a lower viscosity[200]. More volatile SOA products are typically less oxidized, and the less polar nature of these molecules reduces the strength of the inter-molecular interactions they experience, reducing their viscosity while increasing their volatility. This result does highlight the complexity of understanding the viscosity of real SOA systems as it is influenced by the precursor concentrations as well as how the viscosity is inferred from the measurement.

I probed the SOA formation conditions of 75% RH, followed by drying out the droplet to 12% RH in the experiment shown in Figure 5.2. After drying the droplet, I were able to retrieve a self-consistent core-shell fit if I assumed low miscibility of the SOA in squalane. This low miscibility assumption was supported by aerosol mixing experiments performed by other researchers in CMU's Center for Atmospheric Particle Studies' smog chamber[9,97]. This assumption allowed us to constrain the core refractive index to that of pure squalane ($n_{650\ nm}$= 1.4472). I needed the refractive index constraint due to the narrow and complex C-H Raman mode that made it difficult to automatically identify the WGM positions. The resulting refractive index retrievals in Figure 5.2 support and confirm the interpretation of the SOA being on the shell in the completely dry experiment in Figure 5.1. From the 914 core-shell fits the SOA shell had an average refractive index ($n_{650\ nm}$) of 1.4718 ± 0.005 with an average shell thickness of 147 ± 21 nm. The relatively constant yet variable retrieved diameters made calculating and comparing the volatility of the SOA shell vs. squalane core impossible. The retrieved α-pinene SOA refractive index was consistent with my previous measurements at 75% RH of a $n_{650\ nm}$ of 1.473 ± 0.003 in Chapter 4.

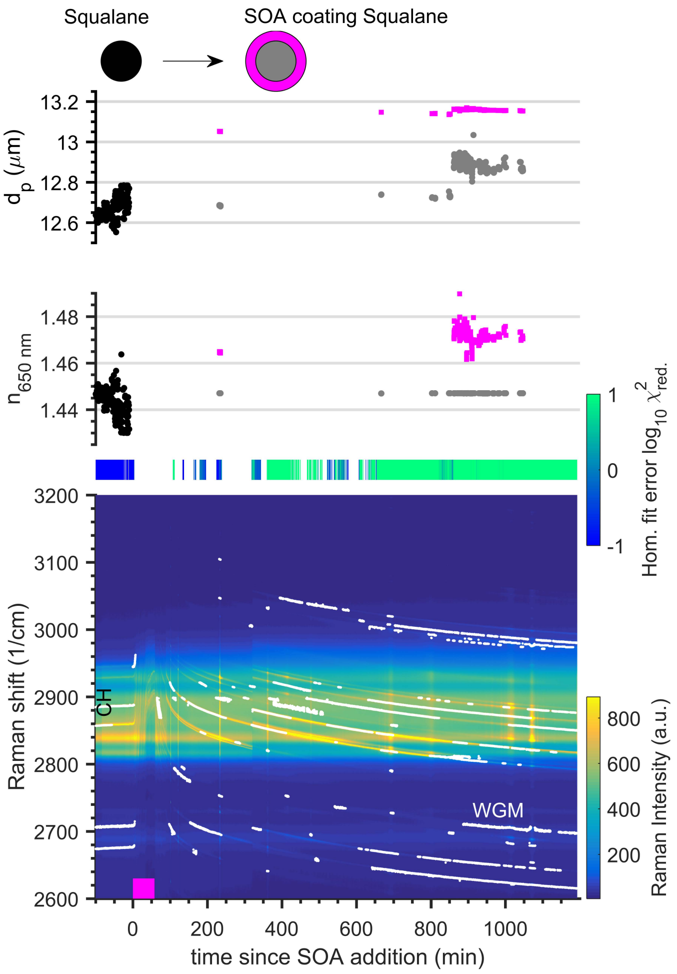

Figure 5.2. Raman spectral time series for a tweezed squalane droplet and the addition of α-pinene SOA, at 75% RH, following the same format as in Fig. 5.1. A decreasing trend of the WGM traces indicates the droplet was evaporating whereas an increase indicates droplet growth. The α-pinene SOA addition started at 0 min. and lasted for 60 min., indicated by the pink bar. At 70 min. the RH was ramped down to 12% RH. The fit results of the WGM positions to a homogeneous model are shown in the top two plots as black dots. The core-shell fitting model is then used to retrieve the properties of the squalane core (gray) and α-pinene SOA shell (pink) following SOA addition. Few WGMs are retrieved as the C-H hydrocarbon mode is too narrow to consistently contain at least 6 WGMs that are required for the core-shell Mie fit. The fit error for the homogeneous model is shown in the green/blue bar, where consistently blue indicates a valid fit and green indicates an invalid fit to the model.

5.4.2 Interplay of Morphology and Surface Tension

My two experiments show that the SOA formation conditions and the RH environment do not affect the equilibrium morphology of a particle containing α-pinene SOA and squalane. As in both the low RH and the high RH SOA reaction conditions, the result was the same core-shell morphology. I can use my results to explore other systems similar to α-pinene SOA using the spreading coefficient framework. The spreading coefficients relate the morphology of the biphasic droplet to the surface tensions between each interface. From the squalane, core-shell morphology with SOA as the shell, I can conclude that the surface tension of α-pinene SOA is less than or equal to that of squalane (28 mN/m[201]). I then assumed that the value of 28 mN/m was the surface tension of SOA so that I can calculate all other possible morphologies as shown in Figure 5.3. This assumption also implies that the interfacial tension between α-pinene SOA and squalane is zero which is an extreme case and it is likely to be slightly above zero making the core-shell parameter space in Figure 5.3 even larger. From Figure 5.3 I can map out a probable morphology for other biphasic systems where the 2nd liquid phase (L2) is similar to my α-pinene SOA phase. For example, when the 1st liquid phase (L1) is water with a surface tension of 72 mN/m, then the interfacial tension has to be < 44 mN/m for it to adopt a core-shell morphology. From my previous SOA additions to aqueous glycerol and aqueous NaCl I observed a core-shell morphology and therefore the interfacial tension of α-pinene SOA and the aqueous phase is < 44 mN/m.

When looking at the interfacial tension between pure organic compounds and water, there is a decreasing trend of interfacial tension (30 to 0 mN/m) with increasing oxidation state (O:C ratio: 0 to 0.5) [202,203]. I drew this trend from the literature on interfacial tensions, and the exact slope depends on the molecular structure[202,203]. I compiled this dependance from the literature data in Appendix D. As O:C increases between 0.6 to 0.8 the biphasic systems of atmospheric interest transition to homogeneous morphologies with an aqueous phase[32,40,42]. Organic phases with higher oxidation states are more polar and thus readily mix with the aqueous phase. For α-pinene SOA generated in a smog chamber the average O:C ratio is 0.41[204] which is consistent with my phase-separation

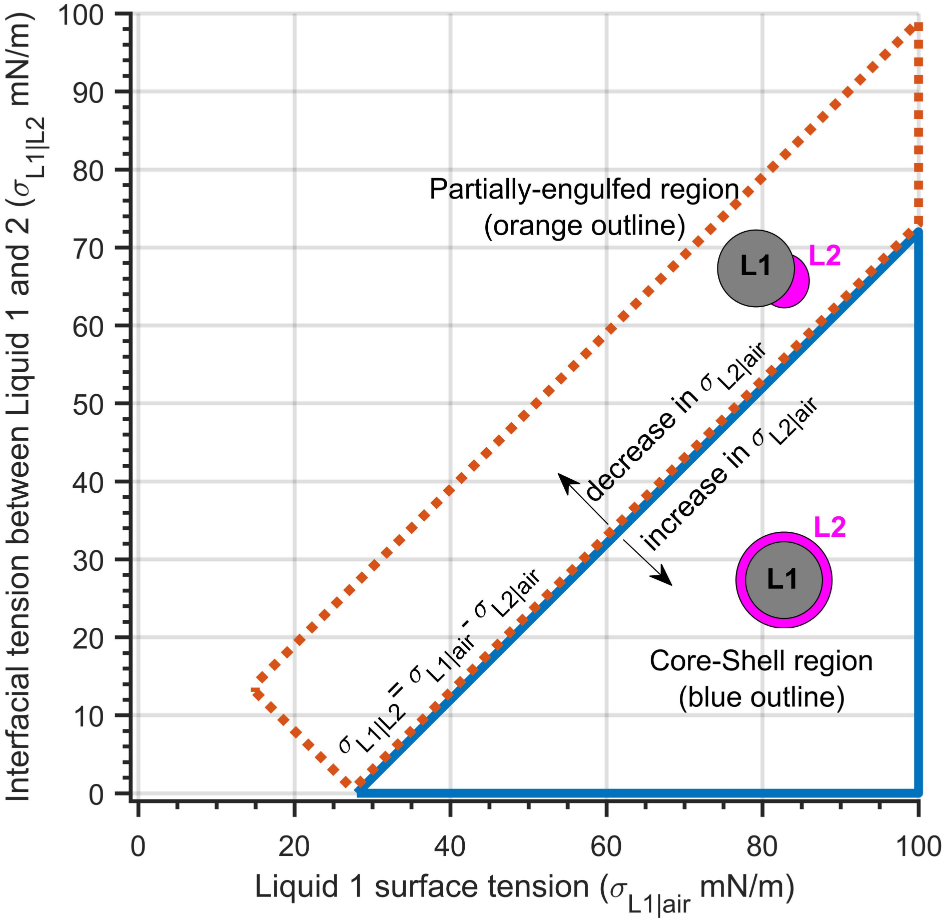

Figure 5.3. Possible morphologies for a biphasic particle composed of a liquid phase (L1, gray) and an SOA-like phase (L2, pink) with a surface tension of 28 mN/m. The L1 phase is assumed to always have a spreading coefficient less than zero. The interfacial tension is assumed to always be less than L1.

results and suggests a low interfacial tension with water. The low interfacial tension is consistent with forming a core-shell morphology. Comparison to the reported average ambient organic aerosol (OA) O:C value of ~0.52[204] also suggests phase separation of the OA phase from an aqueous phase, which would adopt a core-shell morphology with the OA as the shell. For specific components of the OA the primary organic aerosol has a low O:C (0.13 to 0.36[204]) pointing to a higher interfacial tension, which could lead to a partially-engulfed morphology (moving straight up in Figure 5.3). In contrast, ambient SOA has an average O:C of 0.67[204] which will tend to a low interfacial tension and a core-shell morphology (moving down on Figure 5.3). Putting this succinctly, based on my observations I would expect phase-separated particles to start as a partially-engulfed or core-shell morphology and after atmospheric processing to adopt a core-shell morphology for those low O:C – mostly primary OA – systems whose interfacial tensions are so large that they can begin as partially-engulfed structures. Increases in O:C of the OA through atmospheric oxidative processing would not alter a particle that is already in a core-shall morphology. However, if the O:C ratio was increased enough (>0.8) then the OA shell would dissolve into the aqueous phase, forming a homogenous mixed single phase[40].

5.4.3 Miscibility of SOA in a Polar Organic Droplet

The O:C ratio is a coarse measure to understand if a given SOA phase will be miscible in an aqueous droplet, but this simple approach does not transfer to organic-organic phase separation. In my previous work (Chapter 4) and the squalane work above I saw that α-pinene SOA phase-separated to a core-shell morphology when added to a squalane (at 12.5% and 75% RH) and glycerol (at 73% RH) droplet. To understand the phase-separation for this non-aqueous system Ye et al.[97] demonstrated that the Hansen solubility parameter (HSP, δ_t) was effective at predicting phase-separation. They found when the HSP of each phase differed by more than ~8 MPa$^{0.5}$ then the phases would

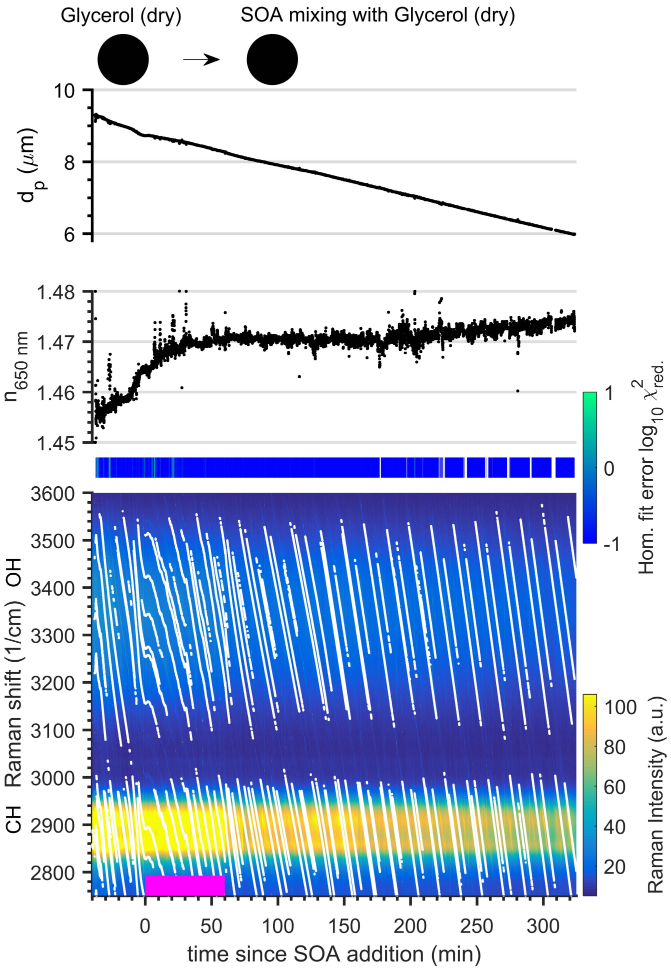

Figure 5.4. Raman spectral time series for a tweezed glycerol droplet with the addition of α-pinene SOA, at 12% RH. Raman spectra are shown in the bottom graph, and the white points indicate the positions of detectable whispering gallery modes (WGMs). The decreasing slope of the WGM traces indicates the droplet is evaporating. The α-pinene SOA flow reaction started at 0 min and lasted for 60 min, indicated by the pink bar. The droplet's refractive index and diameter retrieved from the WGM analysis are shown in the middle and top panels. The fit results of the WGM positions to a homogeneous Mie model are in the top two plots as black dots. The fit error for the homogeneous model is shown in the green/blue bar, where consistently blue indicates a valid fit and green indicates an invalid fit to the model.

separate. The HSP tries to parameterize the intermolecular forces of the dispersion, dipole-dipole interactions, and hydrogen bonding into a single term, δ_t. For simulated α-pinene SOA the average HSP was 24.85 $MPa^{0.5}$, but individual molecular components range from 20 to 32 $MPa^{0.5}$. For squalane the HSP is 15.7 $MPa^{0.5}$ which is different enough from the simulated α-pinene SOA that phase-separation is likely, which is what I saw in my AOT experiments. In the case of glycerol the HSP is 36.1 $MPa^{0.5}$ which is dissimilar enough from the mean HSP of α-pinene SOA to suggest phase-separation, but still close enough for some of the components in the SOA to be miscible in the glycerol. When water is added to the glycerol droplet, the effective HSP is pushed up even higher making phase-separation more likely which is why I observed a core-shell morphology for SOA added to aqueous glycerol. At low humidity it is unclear from the HSP if phase-separation should be expected, as the HSP is not a hard cut off but a guideline.

To probe the miscibility of the glycerol plus α-pinene SOA system I performed the experiments at 12% RH, shown in Figure 5.4. I trapped the pure glycerol droplet at 80% RH and then I ramped down to 12% RH. As the droplet environment passes below 30% RH, the viscosity of the glycerol droplet rapidly increases causing the mass transfer of the reaming 12% of water by mass to evaporate much slower to the gas phase. This slower evaporation is why in Figure 5.4 the refractive index ($n_{650\ nm}$) of the droplet was slowly increasing before 0 minutes towards the refractive index of pure glycerol ($n_{650\ nm}$ = 1.4701[138]). The refractive index of α-pinene SOA I measured is slightly higher than that of glycerol, $n_{650\ nm}$ = 1.4718 ± 0.005. Because of that difference I would expect the refractive index of the droplet to increase when the α-pinene SOA is added, which is what I observed during the SOA addition from 0 to 60 minutes. I also observed a small decrease in the evaporation rate of the whole droplet which is consistent with a vapor pressure reduction when creating a mixture. The change in the refractive index is rapid as I might expect for SOA diffusing into the viscous glycerol phase. The surface of the droplet would change more rapidly which is where the WGMs are generated, explaining the rapid increase in the refractive index. The absence of clear WGM peak splitting (Chapter 3) gives us qualitative proof that a clear core-shell morphology did not form. The constant low fit error of the WGMs to a homogeneous Mie model is quantitative proof that a core-shell morphology did not form. The increase in the refractive index after 200 minutes would be consistent with the evaporation of glycerol driving the mass fraction of SOA higher and therefore increasing the refractive index of the mixture.

There are still two possibilities that could result in this observed homogeneous morphology that this experiment does not probe. If there were a core-shell morphology and the refractive indexes were close enough (<0.00042) they may still fit a homogeneous morphology. This type of refractive index matching of a core-shell droplet has yet to be fully investigated theoretically or experimentally. Due to the very high sensitivity of refractive index in the homogeneous fit, it does seem unlikely that I have a matching of the refractive indexes. The second possibility was that glycerol and α-pinene SOA do phase-separate, but have a high solubility limit that I did not surpass. If I assume the same amount of SOA was added to the glycerol droplet as was added to the squalane droplet (Figure 5.2) then I can estimate a lower bound for the solubility of SOA in glycerol. The solubility limit is at least greater than 22 g of SOA per 100 g of glycerol, if I use an SOA density of 1.4 g/cm^3. This dependence on solubility does point to the coarse nature of using only the HSP to predict phase-separation and suggest that systems that are sparingly soluble in the other phase would help provide the experimental data needed to model POA-SOA phase-separation. In future work I will incorporate the Flory-Huggins solution theory to become more quantitative on the mixing of these two organic phases.

5.5 Discussion

I can qualitatively assessed the self-mixing timescale of the SOA under dry conditions at 12.5% RH and find it to be a liquid-like viscosity. The nucleated particles promptly formed a coating, as the WGMs were not quenched. The mixing of additional SOA particles to the surface has a timescale much shorter than the Raman spectrum acquisition time of 2 seconds, otherwise the WGMs would not have been present. This self-mixing timescale runs in contrast to previous experimental results that conclude SOM is highly viscous and has a self-mixing timescale of months or hours[50,51,60]. The α-pinene SOA generated in my system evidently has a self-mixing timescale shorter than 2 seconds. These contrasting result suggest that SOA mass loadings and therefore volatility distribution can greatly influence the inferred viscosities.

I made use of the spreading coefficients to bound the surface tension of α-pinene SOA. I concluded that the air-liquid surface tension of α-pinene SOA (σ_{SOA}) is less than or equal to that of squalane, which is 28.15 mN/m[201]. This, in turn, helps to constrain the Kelvin diameter for condensation of α-pinene SOA products onto very small particles soon after nucleation in the atmosphere[184,205]. It is also important to note that σ_{SOA} is less than 28.15 mN/m at 75% RH and at 12.5% RH. I found one other direct measurement of α-pinene SOA surface tension in the literature performed using an atomic force microscopy (AFM) technique[206]. They measured a surface tension of 27.5 mN/m at 10% RH and 44.4 mN/m at 67% RH for α-pinene SOA[206]. My observations did not see this strong RH dependence for the surface tension of SOA as my morphology did not change. Based on a SOA surface tension of 44.4 mN/m at 67% RH, my squalane plus SOA experiment at 75% RH should have been a partially-engulfed morphology or core-shell with squalane as the shell. The morphology should not have been core-shell with SOA as the shell, which conflicts with what I observed. This difference in surface tensions between the two methods could be due to my vastly different precursor concentrations and reaction conditions (Chapter 4). The AFM used a smog chamber (batch reactor) with an ozone to α-pinene ratio of 1:1. In contrast the AOT used a flow reactor with an ozone limited reaction of 1:100 ozone to α-pinene ratio. I know from my previous measurements that the volatility of my AOT *in situ* SOA is shifted higher than typical smog chamber reactions. What remains unclear still is how strongly volatility and surface tension are related. Based on the hygroscopic growth factor of α-pinene SOA being ~5% at 70% RH, it would suggest a more modest increase in surface tension of 33 mN/m using a volume mixing rule. However, it has already been pointed out that a simple volume mixing rule for surface tension is insufficient for prediction of mixtures[55,207,208]. It is clear that measurements of SOA surface tension are lacking and its dependence on environmental conditions remains insufficiently explored.

Using my limited dataset on SOA surface tensions I then calculated what the particle morphologies would be for a range of surface tensions. For aqueous systems I would expect phase-separated particles to start as partially-engulfed or core-shell morphology and then after atmospheric processing that increases the oxidation state for them to adopt a core-shell morphology. When the oxidation state increases above an O:C atomic ratio of ~0.8 then the organic phase should mix with the aqueous phase, resulting in a homogeneous morphology. For organic-organic phase-separated systems there is not enough information on surface tensions and interfacial tensions as a function of commonly measured aerosol properties such as O:C.

The Hanson solubility parameter is a good predictor of phase-separation when the solubility is low but for sparingly soluble components this approach is likely too simplistic for atmospheric aerosol. This is pointed out in Figure 5.4 where SOA addition to glycerol does not result in clear phase-separation even though the Hanson solubility parameter would suggest it is likely. As I have previously discussed regarding Figure 5.4, the solubility limit of glycerol and α-pinene SOA may have not be reached, thus I still retained a homogeneous morphology. This was not the case for my squalane and aqueous NaCl system previously studied as the solubility limit was quite low, as the core-shell formation was prompt (Chapter 3 & 4).

This work has summarized my study of *in situ* generated α-pinene SOA that was directly collect onto a droplet trapped in the AOT. I consistently observed core-shell morphologies on aqueous and organic systems with SOA always as the shell. For aqueous systems I discussed that based on the O:C ratios it is likely that the dominate morphology of OA on an aqueous particle in the atmosphere is core-shell with OA as the shell. For organic systems I highlighted the insufficient understanding of how surface tension and more importantly interfacial tension is related to commonly measured ambient aerosol properties like O:C. To predict phase-separation morphologies a deeper understanding of the relation between molecular structure and resulting interfacial and surface tension is needed.

6 Conclusion

In this dissertation I used the aerosol optical tweezers to investigate phase separations and the resulting morphology of complex atmospherically relevant aerosol systems for the first time. The optical tweezers are uniquely suited to directly observe particle morphology from the WGMs generated by Raman scattering. The core-shell Mie fitting algorithm I have developed allowed me to obtain valuable new information on phase-separated droplets.

My study of the morphology of immiscible aerosol systems has assembled the advanced methodology that enabled my subsequent experiments on more complex SOA droplets. I show that a squalane shell creates no measurable impedance on the uptake of water by the underlying aqueous NaCl core, determined from its prompt growth following a humidity ramp. I also highlighted the need for an algorithm to fit unlabeled whispering gallery modes to a core-shell Mie model. This work facilitated the analysis of subsequent complex and realistic aerosol systems.

I then developed a practical and efficient algorithm for fitting WGMs for a core-shell droplet. In the process I have added to the understanding of how WGMs change as a second shell phase forms around a previously homogeneous trapped droplet. The major difference in the WGMs from a homogeneous to a core-shell droplet is the peak splitting of adjacent WGMs which was predicted in Figure 3.4 and demonstrated experimentally in Figure 3.6. I then tested my new fitting algorithm on simulated data for a homogeneous droplet achieving accuracies of ±5 nm in particle diameter (d_p) and ±0.00042 in refractive index (n). The same algorithm applied to a simulated core-shell droplet achieved accuracies of ±34 nm in shell d_p, ±359 nm in core d_p, and ±0.0064 in core and shell refractive indices. Using my new algorithm I analyzed an AOT experiment trapping a core-shell droplet of squalane coating aqueous glycerol. The retrieved refractive indices of the core and shell phases were used to determine the chemical composition of each phase, finding that there is sparing solubility between each phase. This improved analysis method for core-shell droplets opened the door to future experiments that study the dynamics of phase-separated aerosol in the AOT.

I used the improved chamber design and newly developed core-shell fitting algorithm to identify and measure the core-shell morphology of SOA. By combining the results from my AOT experiments and their equivalent smog chamber experiments I can conclude that squalane has no major diffusion limitation through α-pinene SOA. I can also add my additional observations of glycerol evaporating through the SOA shell from Figure 4.3. From the glycerol experiment, I conclude that glycerol has no major diffusion limitation through α-pinene SOA. Finally, from the rapid WGM response to the RH cycle of the SOA coating an NaCl(aq) droplet, I conclude that water also has no major diffusion limitation through α-pinene SOA. If these results hold for other OA systems then assuming prompt partitioning under moderate humidities in atmospheric chemical transport models is valid when the model time steps are on the order of minutes[98,175,196–198].

I consistently observed core-shell morphologies on aqueous and organic systems with SOA always as the shell. For aqueous systems I discussed that based on the O:C ratios it is likely that the dominate morphology of OA on an aqueous particle in the atmosphere is core-shell with OA as the shell. For organic systems I highlighted the insufficient understanding of how surface tension and more importantly interfacial tension is related to commonly measured ambient aerosol properties like O:C. To predict phase-separation morphologies a deeper understanding of the relation between molecular structure and resulting interfacial and surface tension is needed.

6.1 Future Inquiries

It was interesting to note that I only observed core-shell morphologies and never a partially-engulfed morphology with the SOA systems. This aspect does warrant future experiments using mixtures of pure compounds and different SOA precursors. If core-shell morphology is dominant in phase-separated multicomponent systems that would simplify the implementation of modeling phase-separation in the atmosphere.

If work using core-shell droplets becomes more widely valuable, then improvements to the inverse fitting algorithm would be desirable. There are cases where the fitting provided inconsistent results, especially when there are few WGMs. Right now, the optimization cost function only utilizes the position of the WGM peaks but, there are more characteristics that could be added. For example, the height of the peak, relative to its neighbors, adds information as to its possible WGM label. The full spectrum could also be incorporated to check for predicted WGMs positions and the positions of low amplitude WGMs.

The formation of SOA in the AOT should be extended to different precursor compounds like β-caryophyllene and isoprene. Due to the higher O:C ratio of isoprene SOA (~0.87[204]) I would expect the droplet to be homogeneous when the SOA is added to an aqueous system. Contradicting this interpretation are the epoxydiol hydrolysis products from isoprene SOA which can be surface-active and thus could lead to a core-shell morphology [91,93,94].

6.2 Final Remarks

In this work I have systematically improved the experimental capabilities of the AOT, extending it to studying SOA. In the process of understanding the WGMs of a core-shell droplet I, by necessity and curiosity, made substantial improvements to the inverse problem of matching WGMs to a specific droplet size and composition. I then combined both of these improvements to study the morphology of SOA collected directly to a tweezed droplet. My results support the prompt partitioning framework used in atmospheric chemical transport models. Through my experiments I highlight the prevalence of a core-shell morphology; the impacts of which have yet to be explored in atmospheric chemical transport models.

7 Appendix A

Supplemental Information for: Chapter 2 Advanced Aerosol Optical Tweezers Chamber Design to Facilitate Phase-Separation and Equilibration Timescale Experiments on Complex Droplets

Here I discuss in more detail the aerosol optical tweezers (AOT) system and the operation of the AOT. I then outline the improvements made in finding the whispering gallery modes (WGMs) in the Raman spectra. This then allowed us to find enough WGMs on the narrow C-H Raman mode for refractive index and diameter retrieval of hydrocarbon droplets. I then present the full 24-hour dataset for the chamber equilibration assessment experiment. Lastly, I discuss and show the error landscapes for the core-shell fitting of WGMs in the Raman spectra obtained from the NaCl(aq) droplet coated by squalane experiment.

7.1 Aerosol Optical Tweezers System

The Aerosol Optical Tweezers (AOT) system consists of three main components: the aerosol generation system, the droplet trapping system, and the trapping chamber. The trapping system uses a Coherent Verdi 532 nm laser that is operated at a laser power between 60 and 200 mW depending on the trapped droplet size and airflow conditions. The laser is then passed through a set of expansion lenses so that the resulting beam overfills the back aperture of the microscope objective. The expanded laser then passes through the back aperture of a 100x (NA 1.25) oil immersion objective (Nikon). The objective is pressed against the bottom of a thin glass coverslip, and an optical trap forms approximately 40 microns above the coverslip inside the trapping chamber. The coverslip is coated in a solution to disperse impacted droplets so that the optical trap is not significantly distorted.

The droplet is illuminated with a 447.5 nm LED for real-time imaging with a Teledyne DALSA camera (model G2-GM10-T1921). The droplet's Raman scattered light and the blue LED scattered light are collected using the same microscope objective, and separated and delivered to the spectrograph and camera, respectively, as shown in Figure 7.1. The Raman scattered light exits the back aperture and passes through two 50:50 beam splitters. A notch filter (Semrock) then removes most of the intense incident 532 nm light before the signal is focused into the Raman spectrograph. The Stokes shifted Raman spectrum is measured with a Princeton Instruments SP2500 Raman Spectrometer. The spectrometer typically operates using an entrance slit width of 20 μm or less and a 1200 groove/mm diffraction grating blazed at 500 nm, producing a spectral resolution of 0.037 nm. The dispersed Raman spectrum is recorded on a 1024 pixel CCD array chilled to -70 °C used in the Princeton Pixis 256E detector. The spectrograph is calibrated for wavelength position using a built-in Neon-Argon lamp. Under these operating conditions the Raman scattered light is recorded every 2 seconds over a 38 nm spectral range.

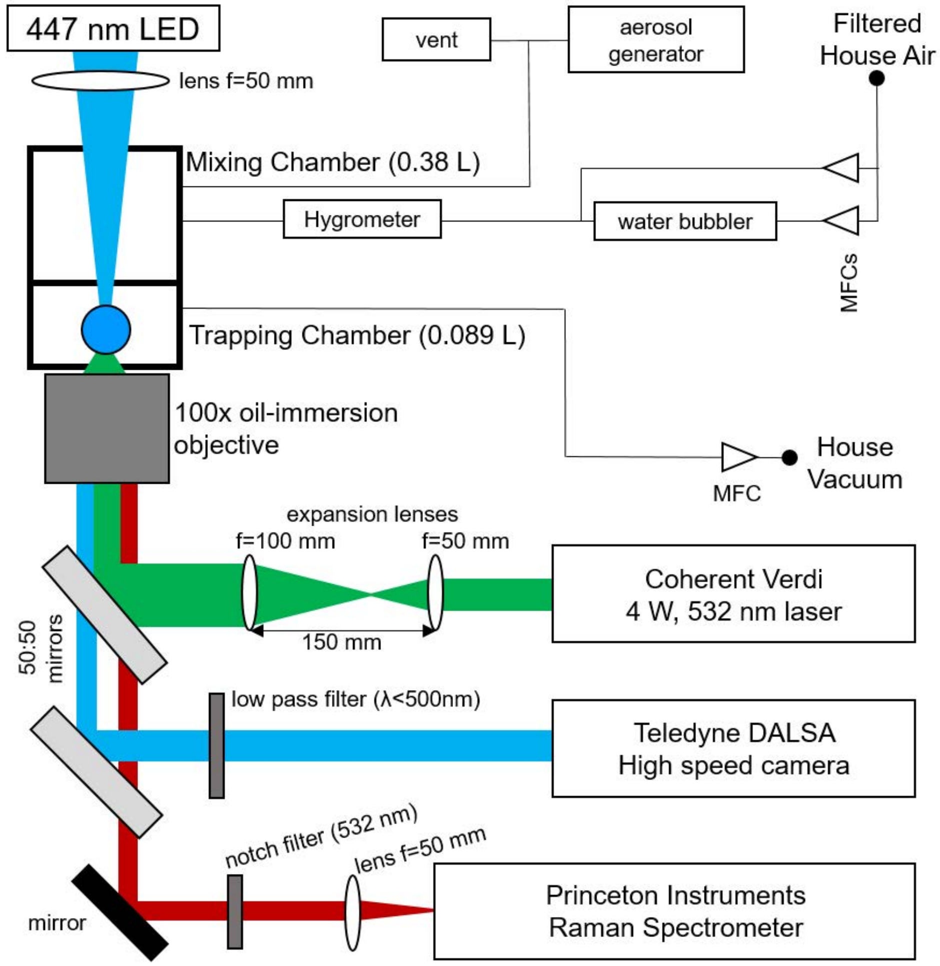

Figure 7.1. Airflow and optical schematic for the aerosol optical tweezers. The house air is dried and filtered before the mass flow controllers (MFCs, 0-1 LPM). The RH is controlled by mixing a dry airflow with humid air that has passed through a water bubbler. A hygrometer (Vaisala) measures the T and RH of the conditioned airflow before it enters the upper mixing chamber. The aerosol generator used is a medical nebulizer if using aqueous solutions, or a Condensational Monodisperse Aerosol Generator (CMAG) to produce large organic droplets. The trapping laser (Coherent Verdi 4 W, 532 nm laser) is expanded to fill the back aperture of the objective, which forms the optical trap. The laser is typically operated at 60 to 200 mW, depending on droplet size. The droplet is backlit using a 447 nm LED and imaged using a Teledyne DALSA high speed camera. The inelastically scattered light from the droplet is filtered and then recorded with a Princeton Instruments Acton Raman Spectrometer.

The aerosol generation system creates droplets of sufficient size and passes them into the chamber. This optical trapping setup requires a minimum droplet diameter of 4 µm when trapping with a typical total laser power of 80 mW (~70% of this power is attenuated by the optics before forming the optical trap). A medical nebulizer (PARI TREK S) is used to generate aerosol from aqueous solutions whose viscosity is similar to water. To trap organic carbon based droplets the condensation monodisperse aerosol generator (CMAG; TSI, Inc.) is used for compounds whose droplets can grow large enough by vapor condensation and are stable when heated. Specifically, this means the compounds must achieve vapor supersaturation at temperatures of less than 300 °C without thermally decomposing. The vapor supersaturation must also be high enough so that the resulting particles produced by heterogeneous condensation are greater than 4 µm in diameter.

7.2 Droplet Trapping and Coagulation

Catching and stably trapping a droplet is the essential first step in an aerosol optical tweezers experiment. To accomplish this, I rely on sending in a mist of droplets of a trappable diameter, greater than 4 µm. A droplet that passes into the optical trap may not be trapped depending on its speed and size. By using a mist of droplets, it is more likely one droplet will become stably trapped. For aqueous systems such as sodium chloride, potassium chloride, and ammonium sulfate, I prepare a saturated solution in water for subsequent aerosol generation by the medical nebulizer. Using the condensation monodisperse aerosol generator (CMAG) I successfully trapped pure organic droplets composed of squalane or dioctyl sebacate.

Before trapping a particle, the chamber is initialized with the conditioned airflow for 10 minutes to allow for the temperature and RH to stabilize. Then the conditioned airflow is turned off while the vacuum flow is opened and the nebulizer or CMAG is running. The aerosols are pulled down the central shaft into the trapping volume until a particle is stably trapped. The aerosol flow is run in a combination of short (10 s) bursts and longer pulses of > 30 s; I have not observed any standard pulse length that guaranties trapping. If there is no particle trapped after 10 minutes the system is reset by changing the coverslip and flowing in clean conditioned air. It should be noted that trapping aerosol droplets with the smaller chamber design used in Hopkins et al. (2004) leads to trapping within 30 seconds. Typical reasons for unsuccessful particle trapping are droplet starting sizes that are too small, a broken/cracked coverslip, or a cloudy/dirty coverslip coating. When trapping I usually have no condition air flow and the vacuum is typically between 0.15 Lpm and 0.25 Lpm. After a particle is trapped the conditioned air flow runs higher than the vacuum flow (0.25 Lpm vacuum and 0.35 Lpm conditioned) to ensure all air flow around the droplet has been conditioned.

When the aerosol flow passes over the coverslip, many of the droplets strike the coverslip due to their large size. I use a coverslip coating to disperse those droplets so that the trapping laser beam is not significantly distorted; that would degrade the symmetrical optical gradient trap. The one system change between tapping an aqueous droplet versus trapping a pure organic droplet is the coating used on the coverslip. For aqueous systems, I soak the coverslips for 30 minutes in a solution of 50 mL Decon 90 surfactant (Electron Microscopy Sciences) and 50 mL Milli-Q water. For the pure organic compounds, I soak the cover slip in a solution of 30 mL Decon 90, 24 mL of reagent alcohol (Sigma Aldrich) and 24 mL of poly(ethylene glycol) dimethyl ether (PEG-DE, averaging MW 500, Sigma Aldrich). Most organic compounds dissolve readily into the PEG-DE, causing dispersal of organic droplets that land on the coverslip during trapping or *in situ* SOM generation. I also tested using glycerol in the cover slip solution but due to its higher vapor pressure I observed the material partitioning into the trapped droplet, making it unsuitable.

7.3 Raman Spectrum Analysis

The analysis of the droplet's retrieved Raman spectrum involves first finding the whispering gallery modes (WGMs) in the raw spectrum and then fitting the wavelength positions of the peaks to a homogeneous Mie scattering model to retrieve the droplet's diameter, d_p, and refractive index, n. For the fitting I use the algorithm developed by Preston and Reid (2013). My previous WGM peak finding method for AOT spectral analysis relied on a smooth spline fitting of a single spectrum (to capture the broad Raman mode) and then preforming a Gaussian fit to the WGM peaks above the smoothed spline. Although this method works well for WGM peaks with a signal to noise over 20, it produces many false positives when used to find WGM peaks at a S/N below 10. This posed a problem with analysis of my pure organic droplets where the WGMs only appear in the narrower C-H Raman mode, and thus there are fewer large WGM peaks (> 10 S/N) to constrain the fit. Aqueous droplets have a broad O-H Raman water stretch mode that supports a larger number of intense WGM peaks, facilitating the fitting.

It is important to find accurate wavelengths for as many WGM peaks as possible because the accuracy of the droplet diameter and refractive index parameter estimation increases as the number of identified whispering gallery modes increases. This is even more important when fitting the WGMs for a core-shell structure because at least 6 WGMs are required, 3 from the core phase and 3 from the shell. To find the less intense WGM peaks in the Raman spectrum, which is required to fit hydrocarbon-only droplets, I developed a new signal processing method. I first remove some of the background noise from the Raman signal by using a non-local means algorithm. Here the non-local means algorithm assesses the variability of each recorded Raman intensity pixel simultaneously in the spectral domain and in the time domain. In this way it assesses the noise over time across spectra and from pixel to pixel, and adjusts the intensity of a given pixel by the weighted average of its neighbors [209–211]. After the spectral noise reduction, I remove the broad Raman signal from the O-H and C-H bands using Matlab's background subtraction algorithm. I then transform the Raman spectrum from the spectral domain to a wavelet domain using a continuous wavelet transform. This is a key procedure to successfully find the lower intensity WGM peaks (S/N < 10) because the continuous wavelet transform acts as a bandpass filter that can be tuned to the frequency range of the WGMs. This causes the WGMs alone to have clear features in the wavelet domain while diminishing any other variations in the signal. Once in the wavelet domain I use a simple peak thresholding to find the peak center and width. I then fit that section to a Gaussian in the spectral domain, recording the center of the Gaussian as the wavelet position of the WGM peak. With this algorithm I can find WGMs that have peak intensities over 2.4 S/N, but I can find even weaker WGM peaks (1.2-1.6 S/N) depending on the noise level of the data. The raw noise level (root mean square) after excluding the WGM peaks is ±5 a.u.

7.4 Chamber Equilibration Assessment

To assess the chamber's equilibration timescale an aqueous NaCl droplet was trapped and used as a probe for RH equilibration. The RH was stepped in increasing and decreasing RH ramps and the droplet diameter and refractive index was fit to the WGMs, as shown in Figure 7.2. Each step change in RH had a corresponding size change of the droplet which was fit to an exponential decay to find the e-folding timescale (Figure 7.3).

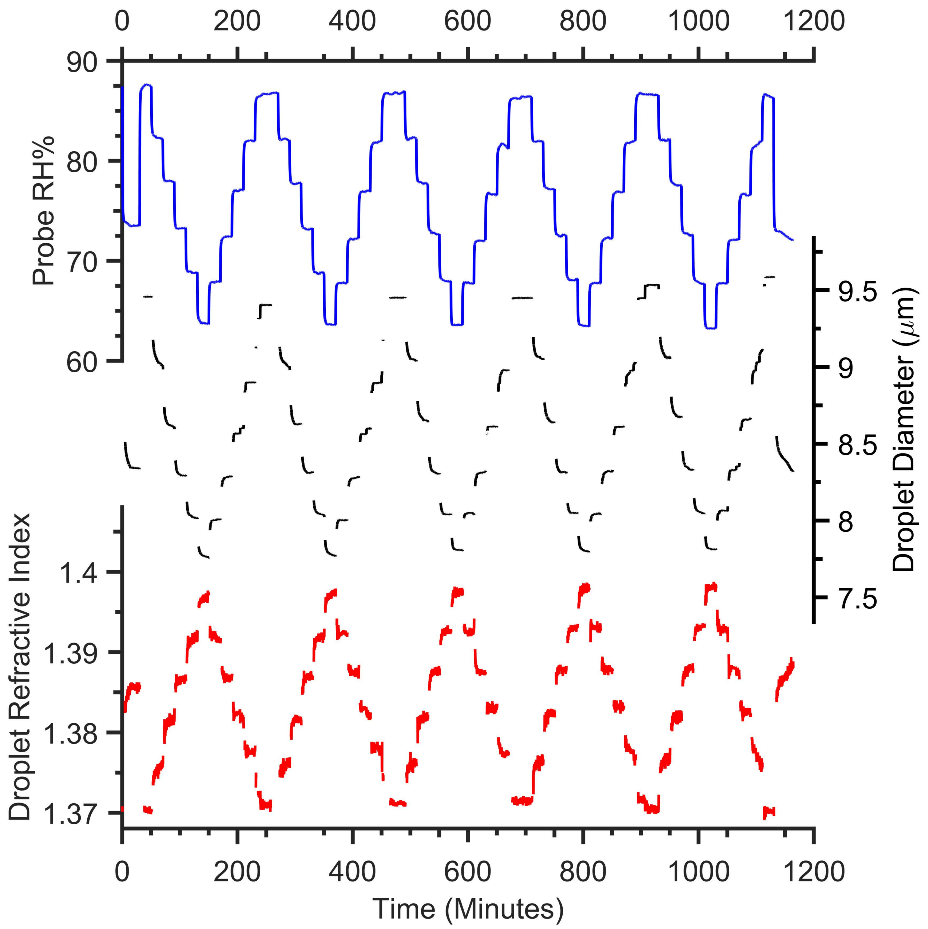

Figure 7.2. Timescale of changes in droplet size and refractive index, determined from fitting the Raman shift positions of the WGMs, as the chamber RH was stepped, to determine the chamber's equilibration timescale. An aqueous NaCl droplet was used, nebulized from a saturated solution of 0.4 g/mL. The RH steps were in increments of 5% in the humid air flowrate, while holding the total conditioned air flow at 0.35 Lpm. Each RH condition was held for 20 minutes before stepping to the next. At each RH step the droplet diameter promptly changed causing the observed WGMs to become blurred, which results in a gap of WGMs and retrieved fit parameters d_p and n. The average equilibration timescale was determined to be 1.83 ± 0.36 min minutes, from fitting the exponential decay of the diameter. A longer equilibration timescale of 3 minutes was observed when RH exceeded 82%. There was a delay in the droplet response after the start of the RH step of 0 to 1.5 minutes, while the hygrometer that measured RH right before the introduction of conditioned flow into the mixing chamber had no measurable response delay. The RH probe's equilibration timescale was measured to be 0.5 minutes, for all RH levels tested here.

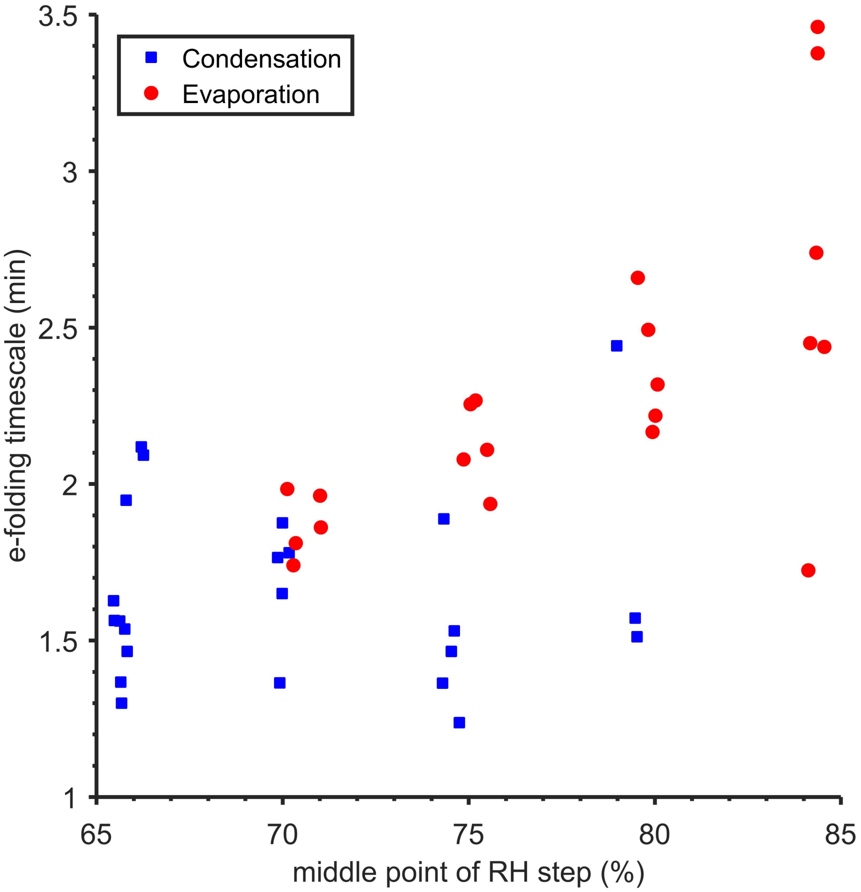

Figure 7.3. An NaCl droplet's e-folding equilibration timescale retrieved by fitting the response of the droplet's size, d_p, to an RH step. The theoretical timescale based on flowrates was 1.44 minutes. The average of RH steps below 82% was 1.83 ± 0.36 minutes.

The second method I used to measure the equilibration timescale is fitting the decay of the WGM Raman shift positions. To do this I calculate the derivative of WGM's position with respect to time and average this with the derivatives from the other WGMs in that spectral frame. In this way I end up with a single time series for the slope of the WGM positions. I then parse this data in the same way as above and fit each RH step to an exponential decay. I plot the e-folding timescale for the NaCl(aq) droplet in Figure 7.4, along with the e-folding timescale for the NaCl(aq) droplet coated by squalane.

The equilibration timescale for the squalane coated droplet is within the range observed for an uncoated droplet. I would expect the equilibration timescale to be on the long side from previous observations as the middle point for the RH step is higher than RH steps probed using the uncoated droplet. From this result I conclude that the squalane coating does not have a measurable effect on the RH equilibration response of the core NaCl(aq) phase. A longer experiment spanning multiple RH steps will be conducted in

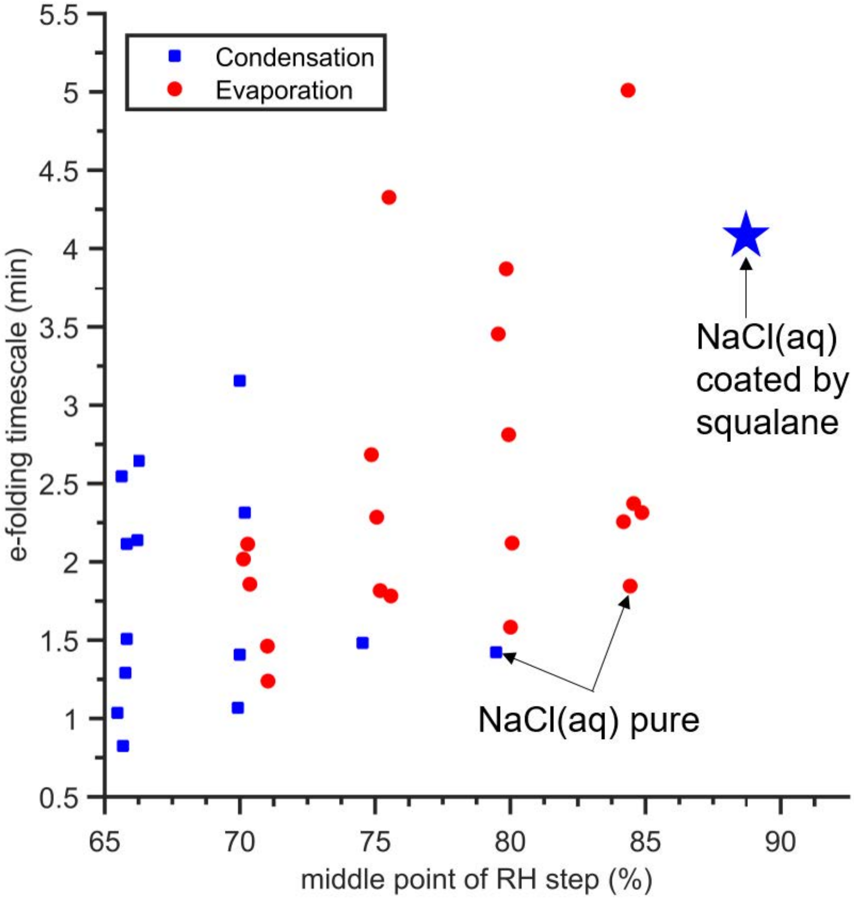

Figure 7.4. An NaCl(aq) droplet's e-folding equilibration timescale retrieved by fitting the response of the average WGM slopes to an RH step. The theoretical timescale based on flowrates was 1.44 minutes. The average of RH steps below 82% was 2.08 ± 0.85 minutes. The e-folding equilibration timescale retrieved from the NaCl(aq) coated by squalane is indicated by a star. Its equilibration timescale is within the upper range observed for an uncoated NaCl(aq) droplet.

the future to investigate the effect of the squalane coating on water equilibration timescales, and the effect of the coating thickness.

I show the full WGM fit results for the dioctyl sebecate and NaCl(aq) droplets below, Figure 7.5 and Figure 7.6. To accurately account for the fact that the refractive index varies with wavelength I use a linear dispersion term, Equation 7.1. Note ν is the wavenumber $(1/\lambda)$ of the WGM wavelength in units of $1/\mu m$.

$$n(\nu) = n_{650\,nm} + \frac{dn}{d\nu}(\nu - \nu_{650\,nm}) \tag{7.1}$$

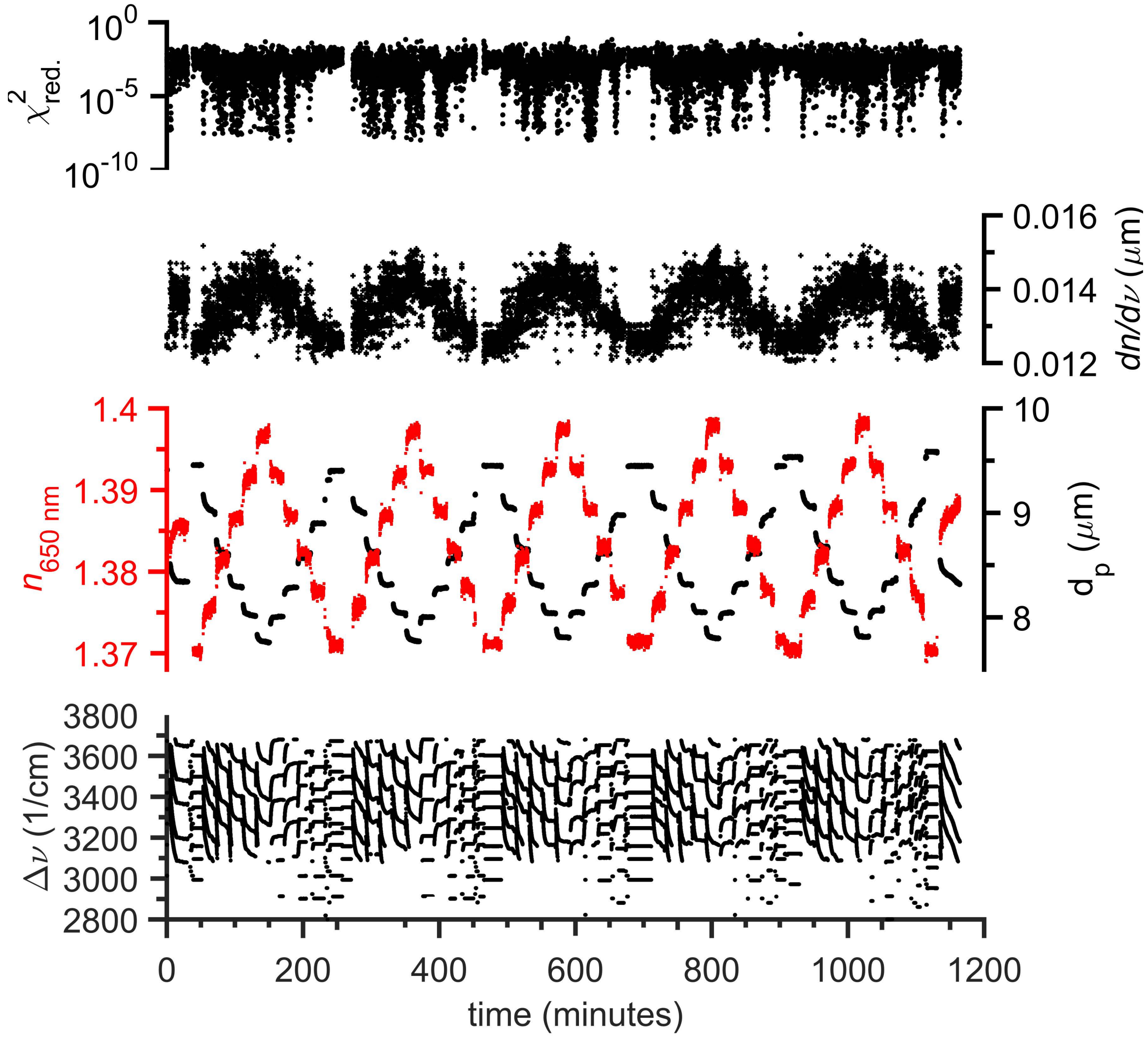

Figure 7.5. The full WGM fit results for NaCl(aq) RH equilibration experiment.

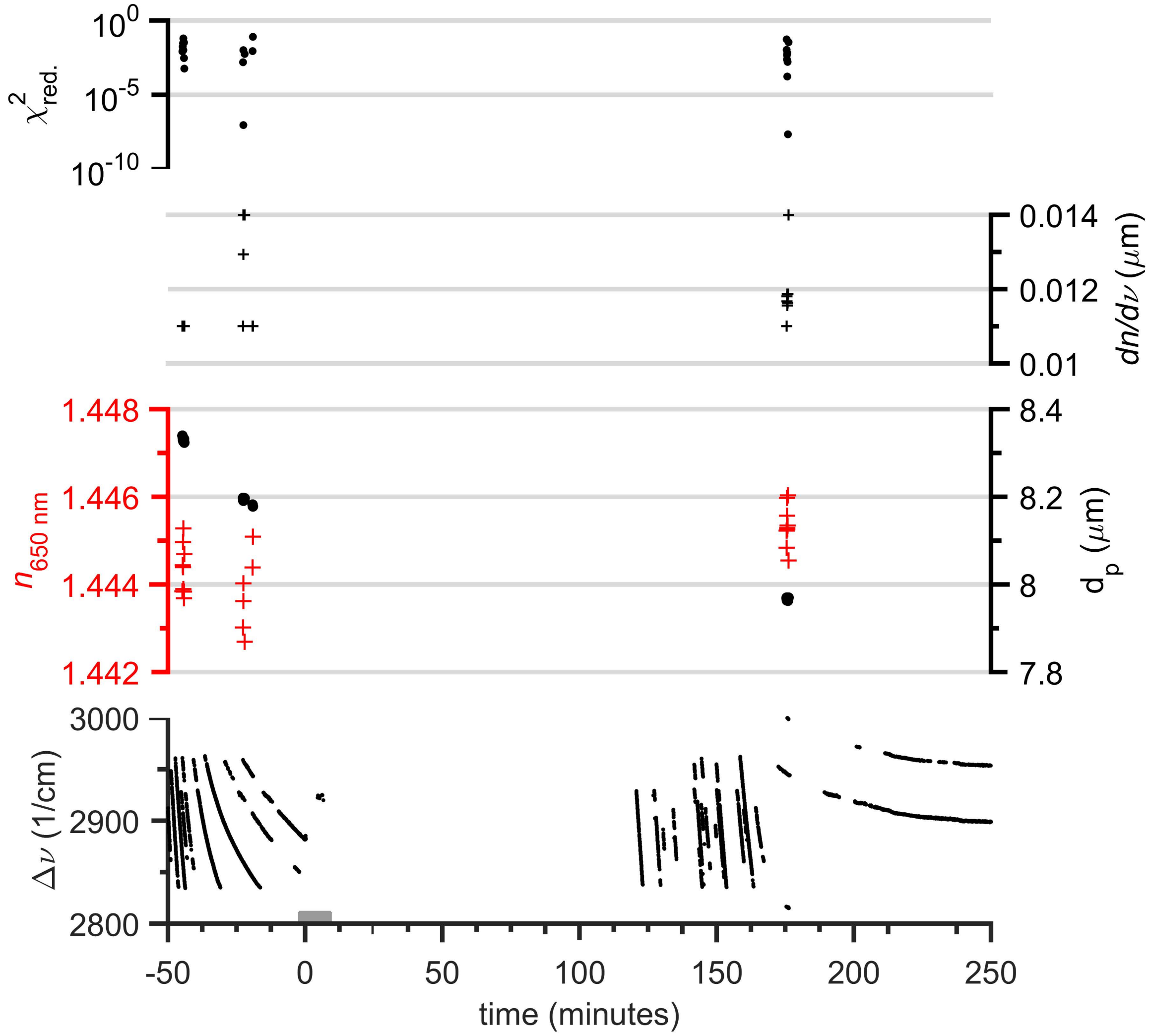

Figure 7.6. The full WGM fit results for the DOS coagulation with glycerol(aq) experiment.

7.5 Core-Shell Fitting Parameters and Error Landscapes

The core-shell optimization problem, just like for the homogeneous algorithm, involves finding the global minimum on a non-convex error space. I used a gridded search over the six droplet parameters: the diameters, refractive indices, and chromatic dispersions for both the core and shell. Then for each parameter set I also need to optimize for the WGM labels, which have discrete values for the mode number (30 to 80), mode order (1 to 3), and EM wave type (TE or TM). For the optimization of the WGM labels I search possible combinations to find the combination with the lowest error for each set of droplet parameters. I sample the droplet parameter space using a gridded search with a specified resolution for each parameter.

In the gridded search I specify the resolution and span of the dispersions and refractive indices, which have to a have a full error calculation done. For each of those 4 parameter sets, the mode numbers, mode order, EM wave type, core-radius and shell-radius are evaluated but a full error calculation does not need to be completed on these parameters. This is due to the core-radius and shell-radius being invariant with each WGM, so I only need to propagate the lowest error parameters and stop the calculation on the higher error values. To reduce the number of parameters needed to fit, I assume the WGM peak with the largest amplitude has zero error and use it set the possible radiuses of the shell. The assumption is relaxed on the $\chi^2_{red.}$ calculation.

7.6 Core-Shell Fit for Squalane Coating Aqueous NaCl

Table 7.1, describes the gridded search space used in the first core-shell fit system of the NaCl droplet coated by squalane. The minimum values for each parameter are projected onto the error landscape of the refractive indices shown in Figure 7.7.

Table 7.1. Core-Shell fit parameters for NaCl(aq) coated by Squalane.

Parameter	lower value	steps	upper value	count
shell $n_{650\text{ nm}}$	1.442	0.0005	1.449	15
core $n_{650\text{ nm}}$	1.36	0.0005	1.38	41
shell dispersion (10^{-2} µm)	1.1	0.05	1.9	17
core dispersion (10^{-2} µm)	1.1	0.05	1.7	13
mode number	40	1	70	30
mode order	1	1	3	3
EM wave type	TE or TM			2
shell radius	(values set by first WGM)			180
core fraction	0.8	0.0025	1	81
CPU time	24.4 hours	Total Parameter Sets		3.56 x10^{11}

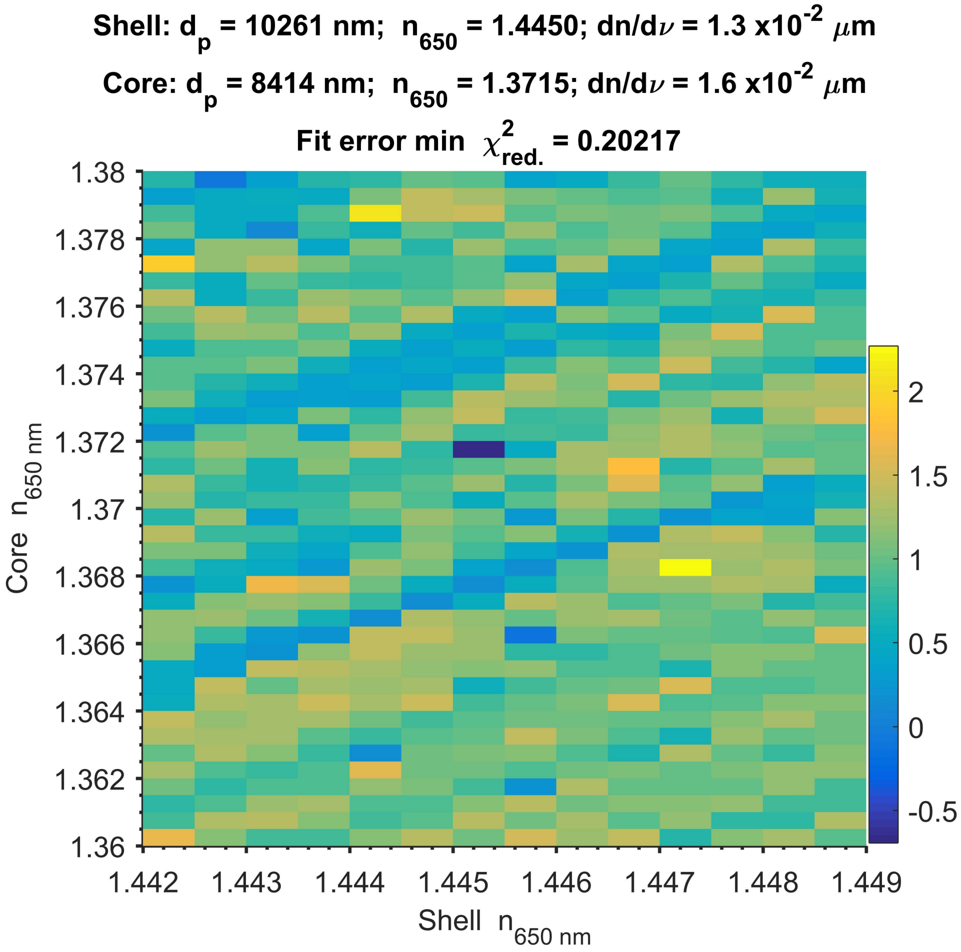

Figure 7.7. Core-shell fit results from using the gridded search parameters from Table 7.1.. The core and shell refractive indices are plotted. Color bar is the $\log_{10}(\chi^2_{red})$., the reduced fit error.

A higher resolution fit was implemented for refinement shown in Table 7.2 and Figure 7.8

Table 7.2. Core-Shell fit parameters for the higher resolution solution for the NaCl coated by squalane system.

Parameter	lower value	steps	upper value	count
shell n650 nm	1.4445	0.0001	1.448	36
core n650 nm	1.369	0.0001	1.373	41
shell dispersion (10-2 µm)	1.2	0.025	1.7	21
core dispersion (10-2 µm)	1.1	0.025	1.7	25
mode number	40	1	70	30
mode order	1	1	3	3
EM wave type	TE or TM			2
shell radius	(values set by first WGM)			180
core fraction	0.8	0.0025	0.92	49
CPU time	39.15 hours	Total Parameter Sets		12.30 x1011

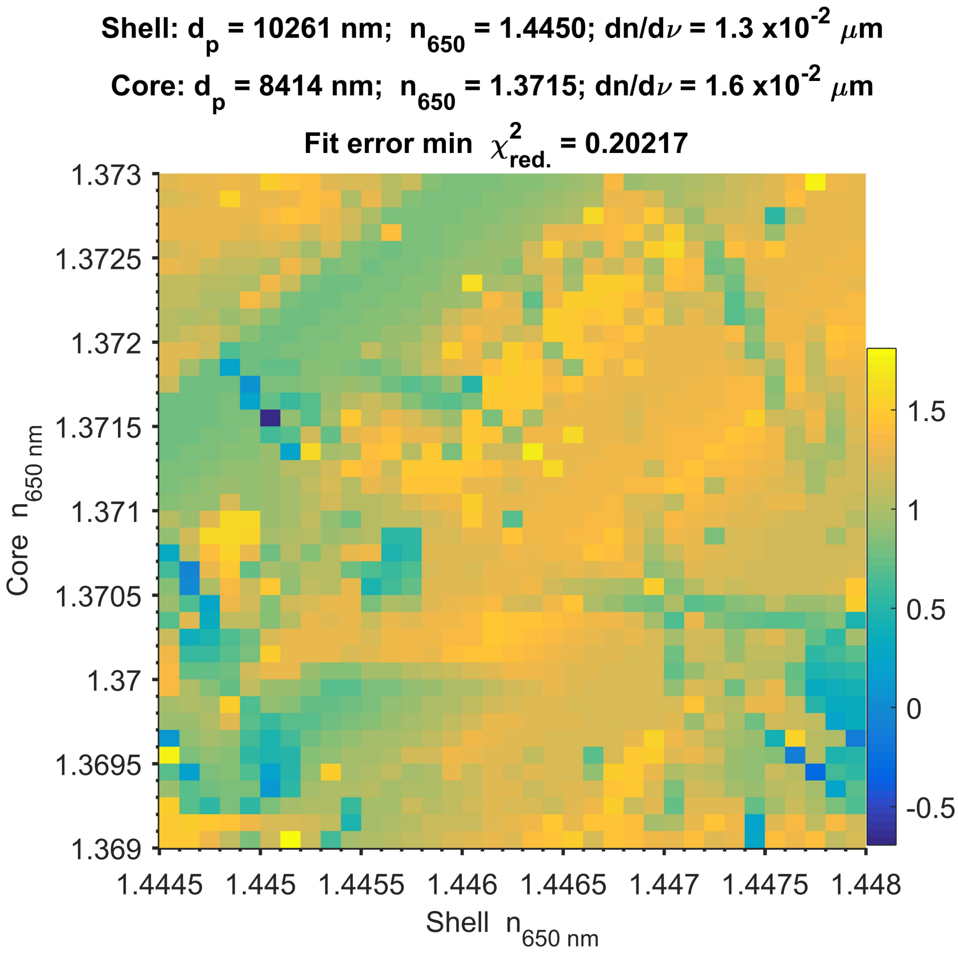

Figure 7.8. Core-shell fit results for NaCl coated by squalane from using the higher resolution gridded search parameters from Table 7.2. Color bar is the $\log_{10}(\chi^2_{red})$.

8 Appendix B

Supplemental Information for: Chapter 3 Determination of the core and shell properties in biphasic droplets analyzed using aerosol optical tweezers

8.1 Overview

Here in I outline the Mie scattering coefficients for a homogeneous and core-shell droplet used for the WGM position calculations. I plot the dependence of WGM position vs. refractive index, and dispersion. I plot an example of WGM peak grouping. I discuss the simulation bounds used for the error assessment of the homogeneous and core-shell fitting algorithm.

8.2 Homogeneous Mie Scattering Model

The homogeneous Mie Scattering derivation presented in Bohren and Huffman (1998) utilizes a slight variation on the notation present in the main text. The Mie size parameter (Eqn. 8.1) is defined by radius (a) in Bohren and Huffman, where I used the more common diameter (d_p) present in the aerosol community. The Mie size parameter (x) is a dimensionless number that relates the circumference of the particle to wavelength of light (λ) incident to it.

$$x = \frac{2\pi a}{\lambda} = \frac{\pi d_p}{\lambda} \qquad (8.1)$$

Lorenz-Mie theory then derives the two scattering coefficients of the sphere, a_n and b_n, Eqn. 8.2 and Eqn. 8.3. The refractive index of the surrounding medium is simplified to be one and therefore m is the refractive index of the droplet.

$$a_n = \frac{m\psi_n(mx)\,\psi_n'(x) - \psi_n(x)\,\psi_n'(mx)}{m\psi_n(mx)\,\xi_n'(x) - \xi_n(x)\,\psi_n'(mx)} \tag{8.2}$$

$$b_n = \frac{\psi_n(mx)\,\psi_n'(x) - m\psi_n(x)\,\psi_n'(mx)}{\psi_n(mx)\,\xi_n'(x) - m\xi_n(x)\,\psi_n'(mx)} \tag{8.3}$$

The solution utilizes the Riccati-Bessel functions which are written bellow for reference, Eqn. 8.4 to 8.6. J_n and Y_n are Bessel functions of the first and second kind.

$$\psi_n(\rho) = J_{n+\frac{1}{2}}(\rho)\sqrt{\rho\frac{\pi}{2}} \tag{8.4}$$

$$\chi_n(\rho) = -Y_{n+\frac{1}{2}}(\rho)\sqrt{\rho\frac{\pi}{2}} \tag{8.5}$$

$$\xi_n(\rho) = J_{n+\frac{1}{2}}(\rho)\sqrt{\rho\frac{\pi}{2}} + Y_{n+\frac{1}{2}}(\rho)\sqrt{\rho\frac{\pi}{2}}\,i \tag{8.6}$$

The WGMs arise when the denominator of scattering coefficients is equal to zero. Therefore, I set the denominator for each coefficient equal to zero and solve for the optimum x value given an m. The transverse magnetic resonance comes from a_n (Eqn. 8.7) and the transverse electric resonance comes from b_n (Eqn. 8.8).

$$0 = m\psi_n(mx)\,\xi_n'(x) - \xi_n(x)\,\psi_n'(mx) \tag{8.7}$$

$$0 = \psi_n(mx)\,\xi_n'(x) - m\xi_n(x)\,\psi_n'(mx) \tag{8.8}$$

The initial guess for the numerical solver for Eqn. 8.7 or Eqn. 8.8, is from the analytical solution for the same equations. The analytical solution is presented in Schiller (1993).

8.3 Core-Shell Mie Scattering Model

The core-shell solution for Mie Scattering derivation is presented on page 183 in Bohren and Huffman (1998). I used a slightly different notation than presented in Bohren and Huffman with the first change being using subscripts of *c* and *s* in replace of 1 and 2 for the core and shell refractive index. The shell size parameter is still defined by the total droplet diameter (Eqn. 8.9), in this case the shell d_p. In Bohren and Huffman the size parameter of the core (y) was defined by the core diameter, where as I chose to relate it as a fraction of the shell diameter, as shown in Eqn. 10.

$$x = \frac{\pi \mathrm{d}_{\mathrm{p-shell}}}{\lambda} \tag{8.9}$$

$$y = x f_c = \frac{\pi \mathrm{d}_{\mathrm{p-core}}}{\lambda} = \frac{\pi \mathrm{d}_{\mathrm{p-shell}} f_c}{\lambda} \tag{8.10}$$

With these slight notation changes I then write out the scattering coefficients for the core-shell system Eqn. 8.11 and Eqn. 8.12.

$$a_n = \frac{\psi_n(x)[\,\psi'_n(m_s x) - A_n\,\chi'_n(m_s x)] - m_s\psi'_n(x)[\,\psi_n(m_s x) - A_n\,\chi_n(m_s x)]}{\xi_n(x)[\,\psi'_n(m_s x) - A_n\,\chi'_n(m_s x)] - m_s\xi'_n(x)[\,\psi_n(m_s x) - A_n\,\chi_n(m_s x)]} \tag{8.11}$$

$$b_n = \frac{m_s\psi_n(x)[\,\psi'_n(m_s x) - B_n\,\chi'_n(m_s x)] - \psi'_n(x)[\,\psi_n(m_s x) - B_n\,\chi_n(m_s x)]}{m_s\xi_n(x)[\,\psi'_n(m_s x) - B_n\,\chi'_n(m_s x)] - \xi'_n(x)[\,\psi_n(m_s x) - B_n\,\chi_n(m_s x)]} \tag{8.12}$$

The two terms A_n and B_n contain the influence from the core and are written in Eqn. 13 and Eqn. 14.

$$A_n = \frac{m_s \psi_n(m_s x f_c)\psi_n'(m_c x f_c) - m_c \psi_n'(m_s x f_c)\psi_n(m_c x f_c)}{m_s \chi_n(m_s x f_c)\psi_n'(m_c x f_c) - m_c \chi_n'(m_s x f_c)\psi_n(m_c x f_c)} \tag{8.13}$$

$$B_n = \frac{m_s \psi_n(m_c x f_c)\psi_n'(m_s x f_c) - m_c \psi_n(m_s x f_c)\psi_n'(m_c x f_c)}{m_s \chi_n'(m_s x f_c)\psi_n(m_c x f_c) - m_c \psi_n'(m_c x f_c)\chi_n(m_s x f_c)} \tag{8.14}$$

The WGMs arise when the denominator of scattering coefficients is equal to zero Eqn. 8.15 and Eqn. 8.16. Therefore, I set the denominator for each coefficient equal to zero and solve for the optimum x. The numerical solver starts at the solution to the homogeneous case (f_c=1) and then slowly decreases f_c by steps of 10^{-3}. This is the same approached used to find the WGM resonances in Stewart et al. (2015).

$$0 = \xi_n(x)[\,\psi_n'(m_s x) - A_n\,\chi_n'(m_s x)] - m_s \xi_n'(x)[\,\psi_n(m_s x) - A_n\,\chi_n(m_s x)] \tag{8.15}$$

$$0 = m_s \xi_n(x)[\,\psi_n'(m_s x) - B_n\,\chi_n'(m_s x)] - \xi_n'(x)[\,\psi_n(m_s x) - B_n\,\chi_n(m_s x)] \tag{8.16}$$

8.4 Whispering Gallery Mode Dependence on Refractive Index

The variation of the whispering gallery modes (WGMs) as a function of the refractive index and dispersion are plotted in Figure 8.1 and Figure 8.2. The inverse of the average slope for the WGMs was then calculated to get the dependence

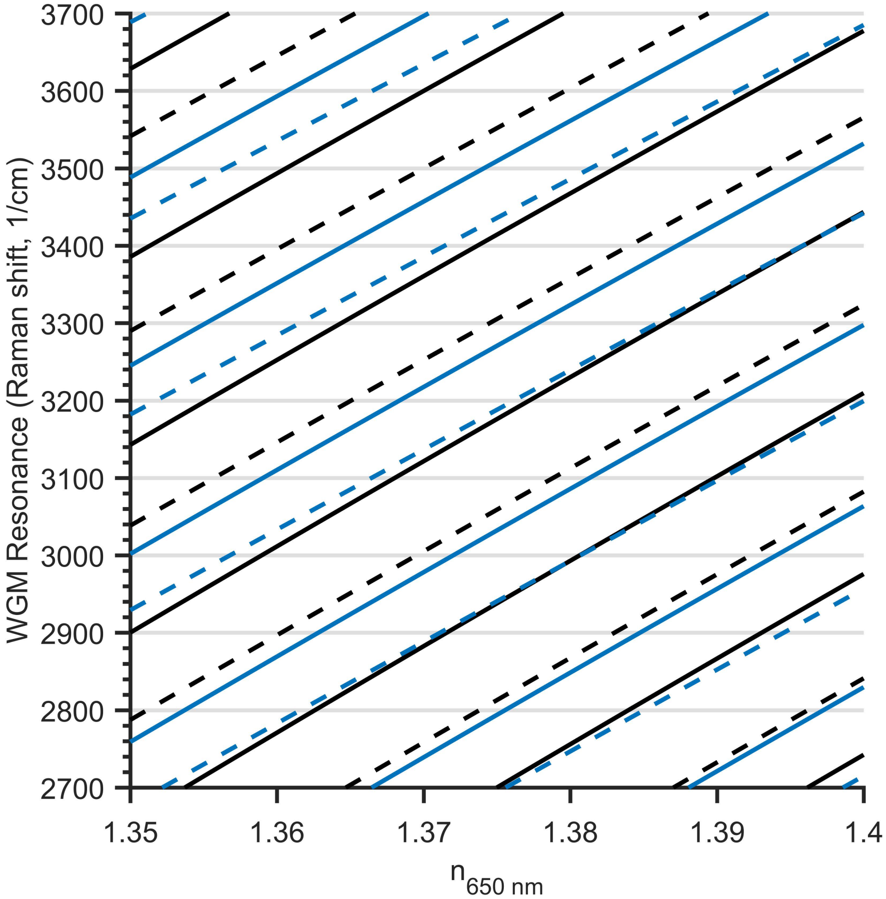

Figure 8.1. Homogeneous droplet refractive index variation from 1.35 to 1.4, while keeping the diameter (10 µm) and dispersion constant (0.01 µm). The WGM resonance wavelength is converted to a 532 nm Raman shift, as this comparable to the AOT measurement. WGM labels are indicated by TE for transverse electric (black) and TM for transverse magnetic (blue), with mode order 1 solid-lines and mode order 2 dashed-lines.

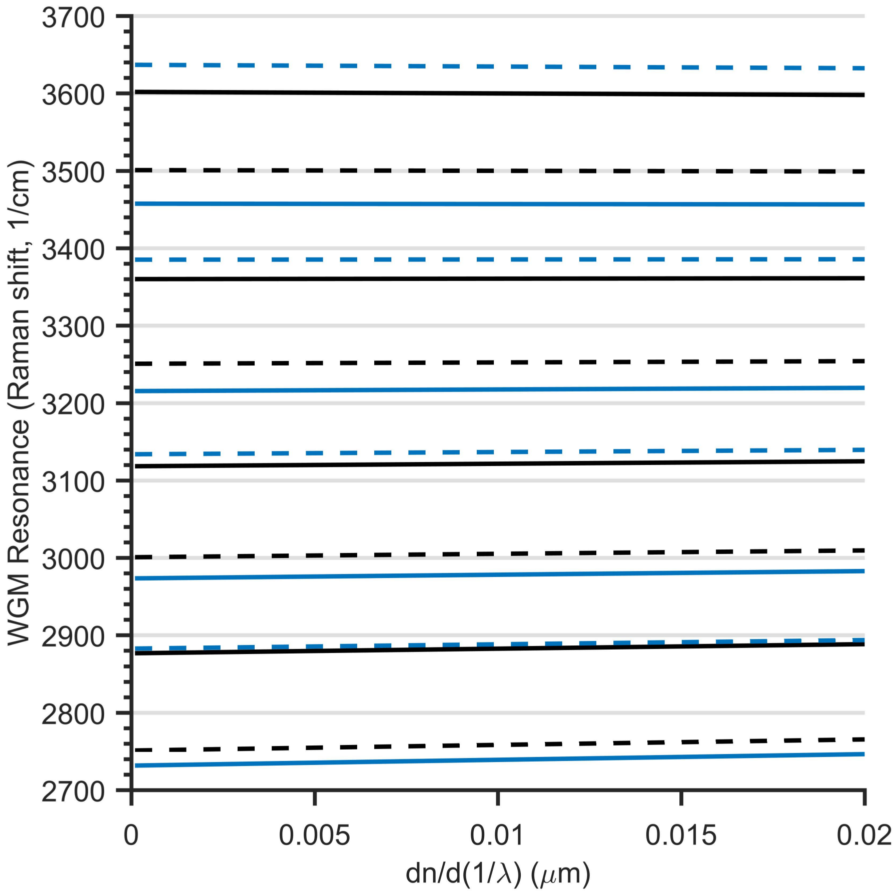

Figure 8.2. Homogeneous droplet dispersion variation from 0 to 0.02, while keeping the diameter and $n_{650\ nm}$ constant. The WGM resonance wavelength is converted to a 532 nm Raman shift, as this comparable to the AOT measurement. WGM labels are indicated by TE for transverse electric (black) and TM for transverse magnetic (blue), with mode order 1 solid-lines and mode order 2 dashed-lines.

8.5 WGM Series Sorting Example

The sorting of the individual WGMs into series follows a simplified version of clustering where if a WGM within 4 cm^{-1} and the gap is smaller than 1 minute the next WGM is placed in the same series. If the gap between the previous WGM and the next is larger than that then a new WGM series is created. I then remove all the WGM series that have less than 30 data points, which helps to remove the scattered WGMs that arise from noise in the data. The result of this sorting is shown in Figure 8.3.

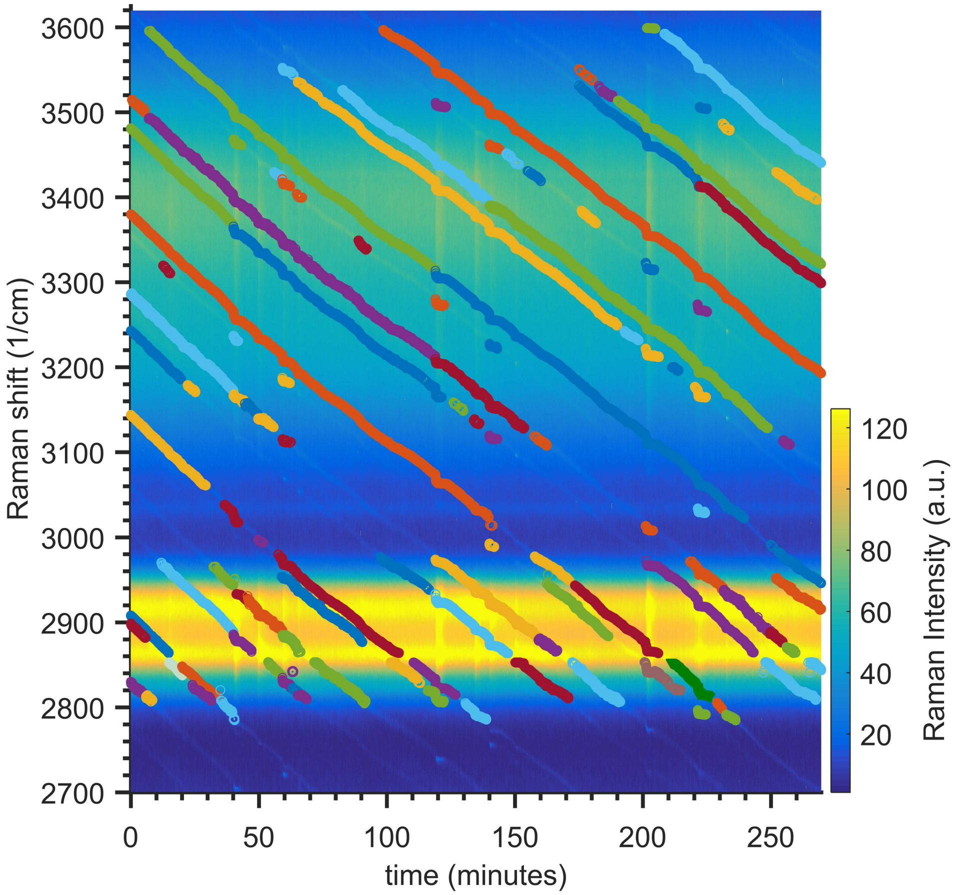

Figure 8.3. WGM series from the squalane coating glycerol experiment. There are 111 separate series. Each series is either has a temporal or spectral gap of 1 min or 4 cm^{-1} and by necessity the induvial colors are repeated. The C-H hydrocarbon Raman mode center is at 2900 cm^{-1}, the O-H aqueous mode is at 3450 cm^{-1}, and the color scale indicates the intensity of the Raman signal at that Raman shift position.

8.6 Additional WGM Algorithm Information

The dispersion fit error is plotted in Figure 8.4, showing that with the fewer parameters in the Homogeneous fit to the dispersion parameter is more constrained than in the core-shell fit.

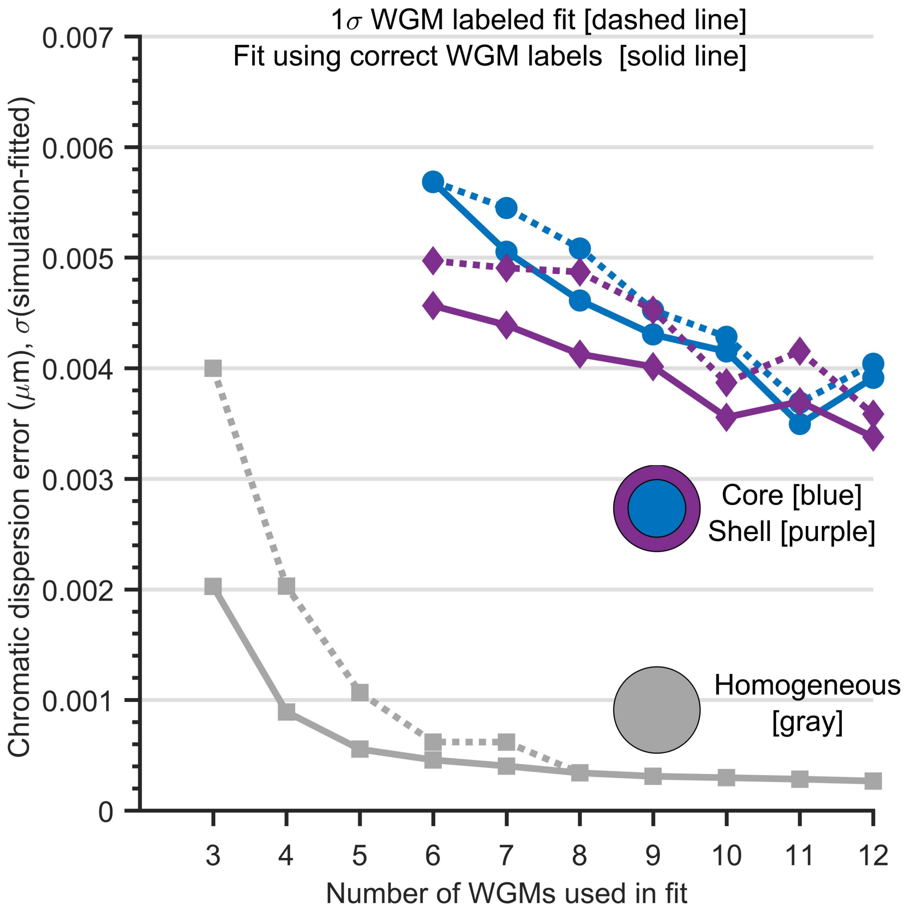

Figure 8.4. The chromatic dispersion (m_1) fit error of a homogeneous and core-shell WGMs versus the number of WGMs used. The standard deviation is for 300 simulated droplets at each set of WGMs used. The dashed line represents the mean of all the fits within 1σ of the global minimum. The solid line is the minimum using the correct WGM labels.

The outline of the algorithm is shown in Figure 8.5. The inputs to the program are the full timeseries of the WGM positions and the sigma's of each WGM.

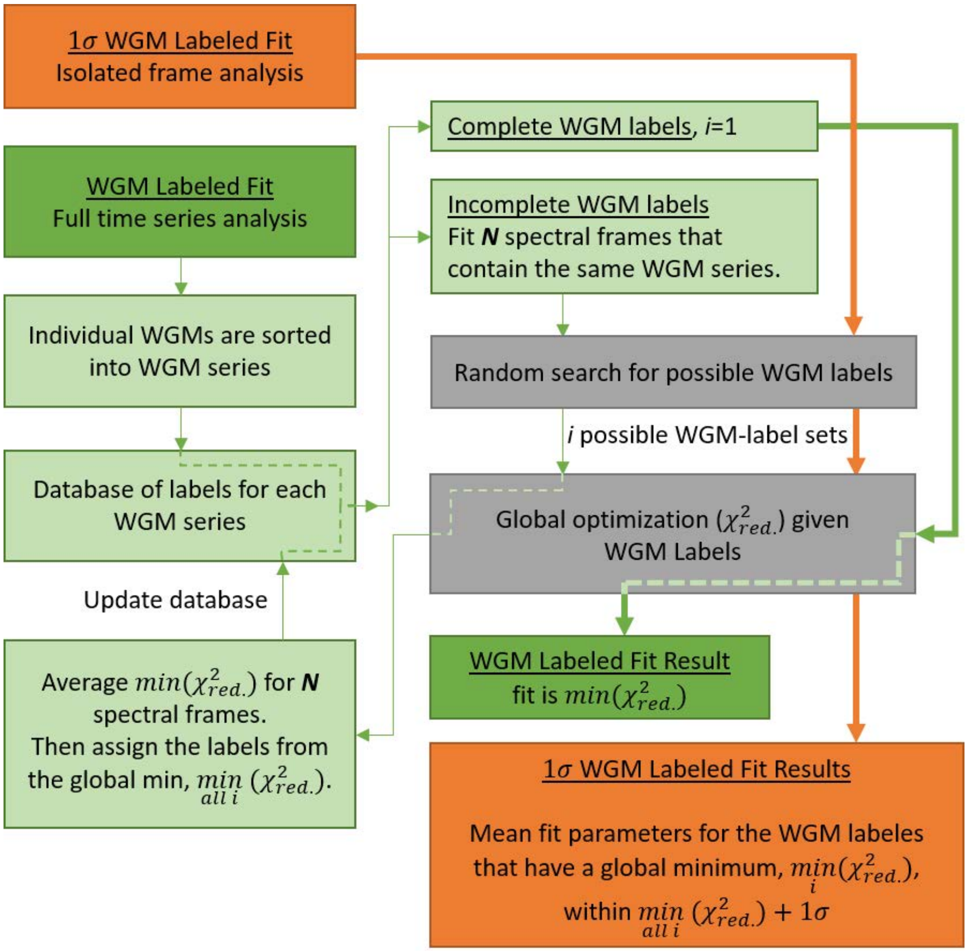

Figure 8.5. Computational outline for the fitting algorithm. Orange represent 1σ WGM labeled fit which uses only a single frame analysis. The green path represents the preferred way to analysis a full timeseries using WGM series.

The average computational times for each part of the algorithm are broken down Table 8.1. The cluster of 32-CPUs has two disadvantages when compared the CPU+GPU method. The first being the network communication which I contribute to the major slow down for the time per random draw, as that step requires a frequent complication between the parallel nodes. That could be improved with a more hierarchical splitting of the parallelization. The second drawback is that the GPU is much faster at the large matrix operation used in the global optimizations than the CPU. Even though the cluster global optimization is efficiently parallelized across the cluster of 32 cores the GPU is more efficient.

Table 8.1. Summary of computational times for the fitting algorithm.

	Homogeneous Droplet (CPU only)	Core-Shell Droplet (CPU + GPU)	Core-Shell Droplet (32 CPUs)
Time per random draw for WGM labels	22 ms	0.7563 sec	2.541 sec
Global optimization time per set of WGM labels	9 ms	0.576 sec	0.949 sec
Total time per set of unlabeled WGMs	2.6 sec	6.82 min	15.52 min

The simulation bounds for the error assessment for the homogeneous and core-shell fits are shown in Table 8.2.

Table 8.2. Simulation bounds for the error assessment of the fitting algorithm.

	Homogeneous Simulation	Core-Shell simulation
f_c (fraction of core)	-	0.8 to 1
d_p or $d_{p\text{-shell}}$	9 to 11 μm	9 to 11 μm
m_{C0} (n_{650nm})	1.37 to 1.42	1.37 to 1.42
m_{S0} (n_{650nm})	-	1.4 to 1.45
m_{C1} (dispersion)	0 to 0.02 μm	0 to 0.02 μm
m_{S1} (dispersion)	-	0 to 0.02 μm

8.7 Method for α-Pinene SOA Addition

The method I implemented for α-pinene SOM addition turns the AOT chamber into a flow reactor; the experimental schematic is shown in Figure 8.6. During a typical ozonolysis experiment, the ozone concentration in the AOT was constant at 3.4 ppm$_v$, calculated based on the air flow rates and volume mixing. The ozone flows from a UV lamb ozone generator (using air) and the output concentration was validated with an ozone monitor (Dasibi 1008-PC). I introduced the α-pinene vapor *via* a second dry air flow (0.05 Lpm) that passed over a pool of liquid α-pinene before entering a secondary port on the top of the mixing chamber. The α-pinene concentration in the mixing chamber was 182 ppm$_v$, estimated based on temperature, compound saturated vapor pressure, and gas flow rates. In contrast to my previously report AOT SOA experiments the concentrations are much lower so I do not observe any optically detectable particles from the α-pinene oxidation in the form of small-particle light scattering events in the visual droplet imaging. The vapors and particles produced in the upper section of the AOT

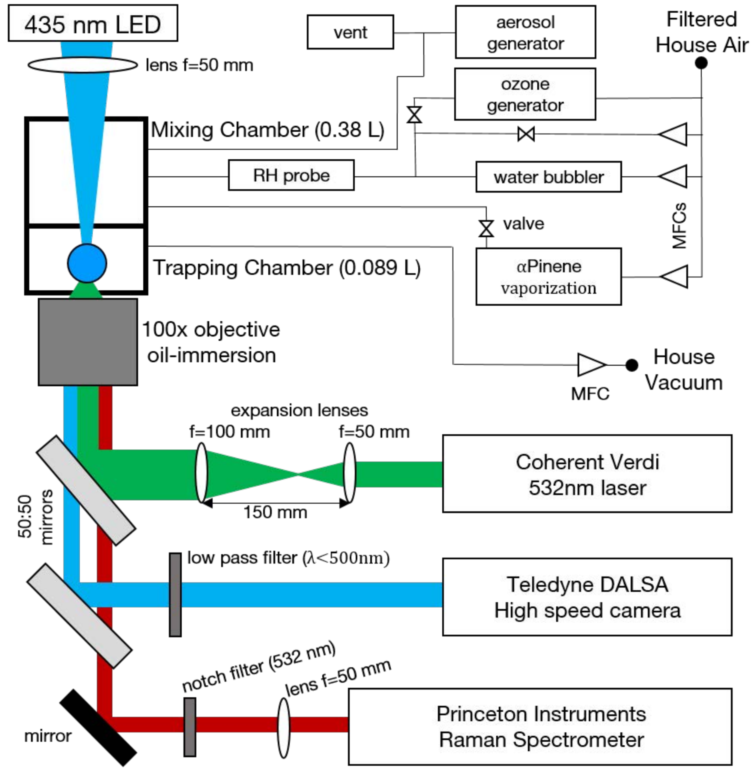

Figure 8.6. Airflow and optical schematic for the aerosol optical tweezers. The house air is dried and filtered before the mass flow controllers (MFCs, 0-1 LPM). There is a dedicated flow for the introduction of α-pinene vapor that goes directly to the mixing chamber. The RH is controlled by mixing a dry airflow with humid air that has passed through a water bubbler. A hygrometer (Vaisala) measures the T and RH of the conditioned airflow before it enters the upper mixing chamber. There is the option to flow dry airflow form an UV lamb ozone generator. The aerosol generator used is a medical nebulizer if using aqueous solutions, or a Condensational Monodisperse Aerosol Generator (CMAG; TSI, Inc.) to produce large organic droplets. The trapping laser (Coherent Verdi 4 W, 532 nm laser) is expanded to fill the back aperture of the objective, which forms the optical trap. The laser is typically operated at 60 to 200 mW, depending on droplet size. The droplet is backlit using a 447 nm LED and imaged using a Teledyne DALSA high-speed camera. The inelastically scattered light from the droplet is filtered and then recorded with a Princeton Instruments Acton Raman Spectrometer.

chamber were then transported toward the tweezed droplet at the bottom of the AOT chamber. An appreciable portion of the less volatile SOA components was likely lost by adsorption to the metal chamber walls, but these components by necessity will also be present in the nucleated particles that coalesced with the tweezed droplet [175].

9 Appendix C

Supplemental Information for Chapter 4: Emulsified and liquid-liquid phase separated states of α-pinene secondary organic aerosol determined using aerosol optical tweezers.

I discuss in more detail the aerosol optical tweezers (AOT) experimental setup and the addition of α-pinene secondary organic matter (SOM). I show isolated frames of the Raman spectrum during the NaCl(aq) plus SOA experiment. Raman spectra from experiments where solid NaCl crystals were present in a squalane droplet to test the effect of emulsified particles on the WGMs are presented. Finally, I present an assessment of the core-shell fitting from the Raman spectra, and the evaporation rate calculation.

9.1 Method for α-Pinene SOA Addition

The method I implemented for α-pinene SOM addition turns the AOT chamber into a flow reactor; the experimental schematic is shown in Figure 9.1. During a typical ozonolysis experiment, the ozone concentration in the AOT was 60 ppm_v and decreased to 50 ppm_v after 60 min, calculated based on the air flow rates and volume mixing. The ozone flows from a 4 L bottle, which was filled to a steady state concentration by an ozone generator (using O_2) and the output concentration was validated with an ozone monitor (Dasibi 1008-PC). I introduced the α-pinene vapor *via* a second dry air flow (0.05 Lpm) that passed over a pool of liquid α-pinene before entering a secondary port on the top of the mixing chamber. The α-pinene concentration in the mixing chamber was 500 ppm_v, estimated based on temperature, compound saturated vapor pressure, and gas flow rates. The ozonolysis of α-pinene proceeds by addition to the solitary double bond and the reaction was ozone limited under these conditions. This reaction produces ·OH radicals with a yield of ~0.8, and under my conditions essentially all of the ·OH reacted with α-pinene[174]. Consequently, the SOM consisted of an approximately 0.8:1 mixture of OH and ozone oxidation products. I occasionally observed nucleation of optically detectable particles from the α-pinene oxidation in the form of small-particle light scattering events in the visual droplet imaging. The vapors and particles produced in the upper section of the AOT chamber were then transported toward the tweezed droplet at the bottom of the AOT chamber. An appreciable portion of the less volatile SOA components was likely lost by adsorption to the metal chamber walls, but these components by necessity will also be present in the nucleated particles that coalesced with the tweezed droplet[175].

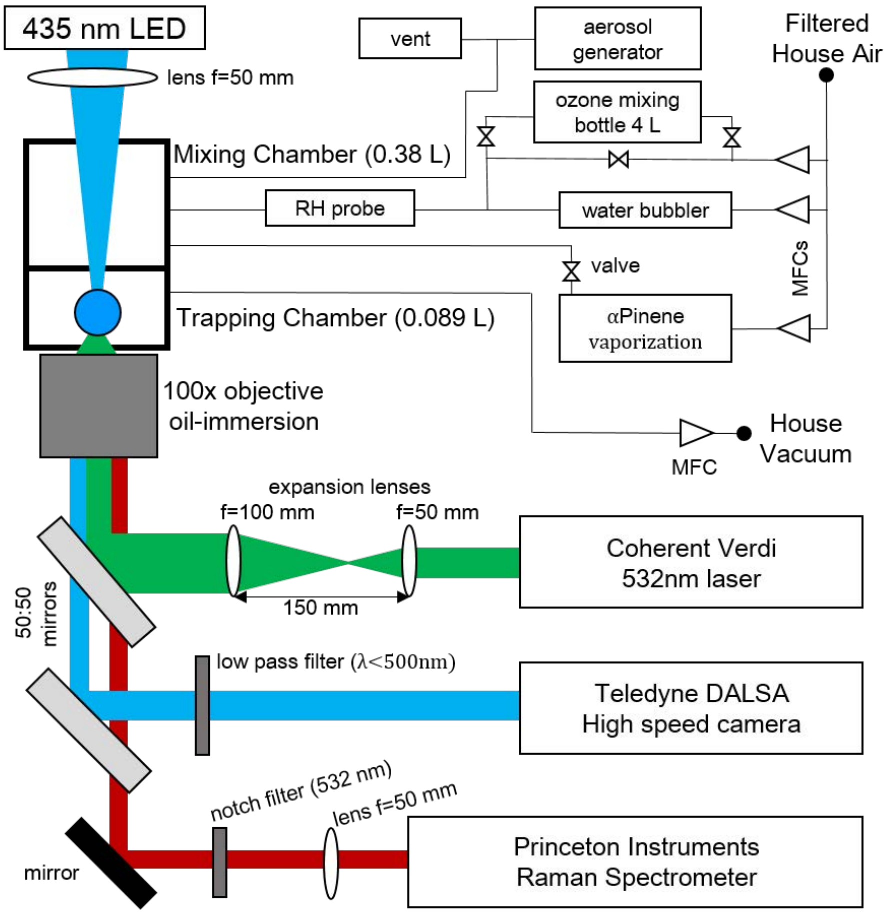

Figure 9.1. Airflow and optical schematic for the aerosol optical tweezers. The house air is dried and filtered before the mass flow controllers (MFCs, 0-1 LPM). There is a dedicated flow for the introduction of α-pinene vapor that goes directly to the mixing chamber. The RH is controlled by mixing a dry airflow with humid air that has passed through a water bubbler. A hygrometer (Vaisala) measures the T and RH of the conditioned airflow before it enters the upper mixing chamber. There is the option to pass the dry airflow through a 4 L bottle filled with ozone from an ozone generator. The aerosol generator used is a medical nebulizer if using aqueous solutions, or a Condensational Monodisperse Aerosol Generator (CMAG; TSI, Inc.) to produce large organic droplets. The trapping laser (Coherent Verdi 4 W, 532 nm laser) is expanded to fill the back aperture of the objective, which forms the optical trap. The laser is typically operated at 60 to 200 mW, depending on droplet size. The droplet is backlit using a 447 nm LED and imaged using a Teledyne DALSA high-speed camera. The inelastically scattered light from the droplet is filtered and then recorded with a Princeton Instruments Acton Raman Spectrometer

9.2 Accuracy of Core-Shell Fitting

The core-shell optimization problem, just like for the homogeneous Mie fit, involves finding the global minimum on a non-convex error space. I use a combination of a random search for the WGM labels and a gridded search for the diameters, refractive indices, and chromatic dispersions for both the core and shell. The WGM labels have discrete values for the mode number (30 to 80), mode order (1 to 2), and EM wave type (TE or TM). For the optimization of the WGM labels, I search possible combinations to find the set with the lowest error. The summary of the fit accuracy is shown in Table 9.1. This summary is a result of 2100 simulated WGM spectra using between 6 to 12 WGMs in each fit.

Table 9.1. Accuracy of the core-shell fitting.

Fit Parameter	Accuracy stdv(simulated - fitted)
shell dp	0.0344 μm
core dp	0.3596 μm
shell n650 nm	0.0060
core n650 nm	0.0068
shell dn/d(1/λ)	0.0039 μm
core dn/d(1/λ)	0.0045 μm

The accuracy reported in Table 9.1. is for a single frame, i.e. the accuracy on an individual data point. The accuracy reported in the manuscript is the standard deviation of the all data points, which is shown Table 9.2. There were 111 data points for the SOA coating NaCl(aq) droplet, 2716 data points for the SOA coating glycerol(aq) droplet, and

59 data points for the SOA coating squalane droplet. This table is also used to compare my retrieved refractive index value to those reported in the literature; good agreement is found between my measured refractive index for α-pinene SOA and the literature values.

Table 9.2. Summary of α-pinene SOA refractive indices.

Method Used	Refractive Index	Wavelength	Reference
AOT, SOA coating NaCl(aq)	1.469 ± 0.004	650 nm	This work.
AOT, SOA coating glycerol(aq)	1.474 ± 0.005	650 nm	This work.
AOT, SOA coating squalane	1.473 ± 0.003	650 nm	This work.
Cavity Ring-Down, PASS-3 and SMPS	1.476 ± 0.022	532 nm	Nakayama et al., 2012
EDB with a Cavity Ring-Down (aq. SOA)	1.45 to 1.49	532 nm	Marsh et al., 2017
Polar Nephelometer and SMPS	1.43 to 1.52	532 nm	Kim et al., 2014
Polar Nephelometer and SMPS	1.4 to 1.48	670 nm	Kim et al., 2010
Polar Nephelometer and SMPS	1.39 to 1.52	532 nm	Kim and Paulson, 2013
Cavity Ring-Down, Albedometer and DMA	1.49 to 1.51	532 nm	Redmond and Thompson, 2011
Quantitative Structure-Property Relationship Prediction	1.493	589 nm	Redmond and Thompson, 2011
Unreacted α-pinene liquid	1.4632	589 nm	Haynes W. M., 2017

9.3 Humidity Cycling of SOA on an Aqueous Inorganic Droplet

My multipart experiment on a single trapped droplet composed of an initially supermicron aqueous NaCl droplet to which I added SOM through submicron particle coagulation and vapor condensation is summarized in Figure 9.2. Synthesizing the information learned from the various stages of this experiment support my proposal of an emulsion of SOM particles in the aqueous core that was then converted into a completely phase-separated core-shell state by partially dehydrating the aqueous core. I can also conclude from the core-shell fit that the core-shell morphology observed at the end of the experiment in Figure 9.2 after the RH cycling is the thermodynamically stable condition for this mixed system. Therefore, before the RH cycle, it is likely that a core-shell morphology was thermodynamically favored then as well. By decreasing the aqueous core's volume the rate at which the emulsified SOA particles found the SOA interface was increased, promoting the demulsification. Finally, a droplet morphology composed of a homogenous shell and emulsified submicron particles in an inhomogeneous aqueous core would also explain the diminished and intermittent WGM signal observed. This would account for the partial resonance of WGMs in the surface layer that penetrates through the thin SOA shell into the outer layer of the emulsion-containing aqueous core, while not permitting the full amplification of the WGMs due to interference by the emulsion in the core.

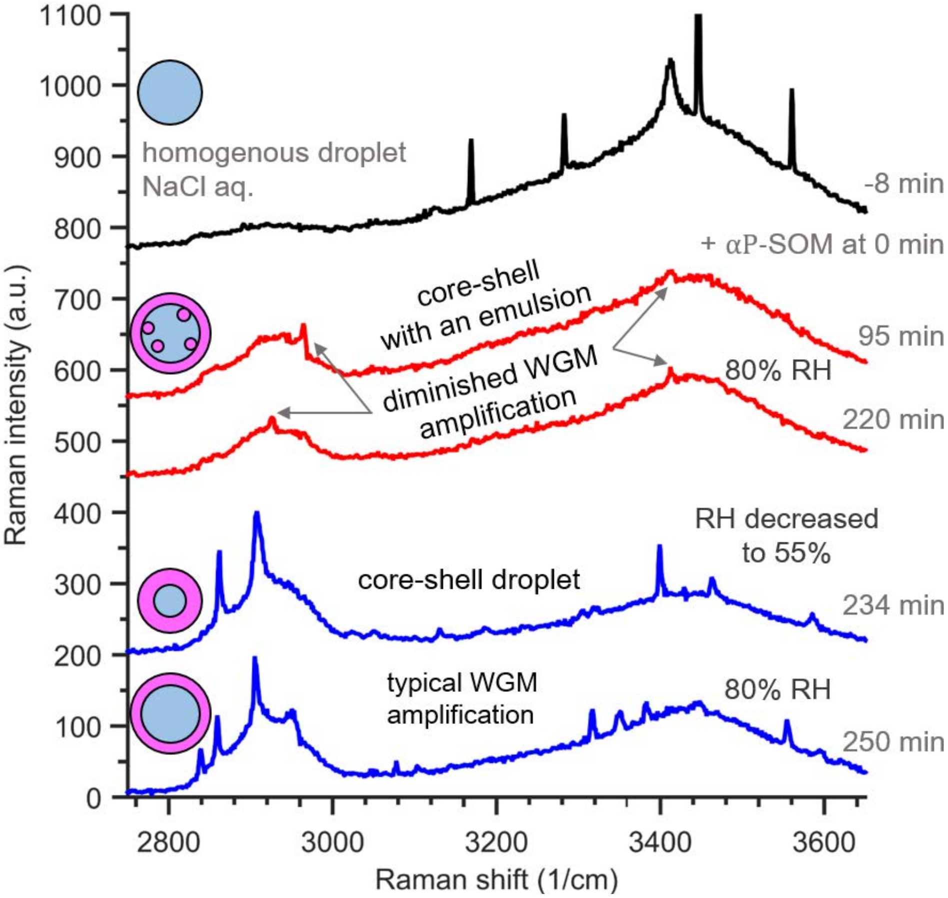

Figure 9.2. Summary of the evolution of the Raman spectra for different droplet morphologies as α-pinene SOM was added to a NaCl(aq) droplet, followed by cycling the chamber RH. The black line represents the NaCl(aq) droplet before SOM addition, showing strong WGM resonant peaks. After SOA addition ends and clean airflow was restored the WGMs remained diminished (red lines). A core-shell structure containing an emulsion of SOA explains the diminished but not absent WGM amplification. The return of the normal amplification of the WGMs after the RH was decreased from 80% to 55% at 234 min indicates the emulsion was no longer present (top blue line). The WGM patterns indicating droplet growth after the RH was restored to 80% (bottom blue line).

From the retrieved WGMs during the period of diminished amplification, I cannot determine exactly what the morphology of the core is. It is radially inhomogeneous as the WGMs are diminished, but exactly where these inhomogeneous occur is undetermined. In Figure 9.3 I propose some possible configurations.

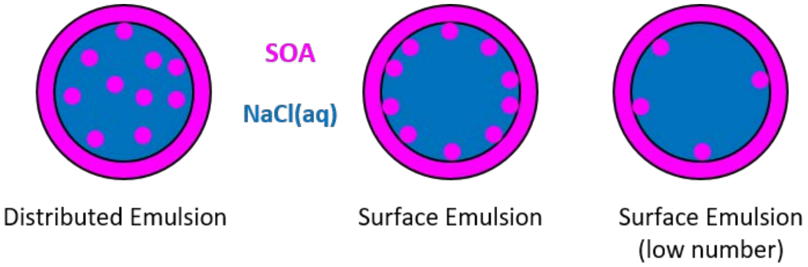

Figure 9.3. Example configurations for a radially inhomogeneous core. SOA phase in pink and NaCl(aq) phase in blue. These would all result in diminished and intermittent WGM amplification.

9.4 Effect of Emulsified Salt Crystals on the Raman Spectrum's WGMs

An additional experiment was performed to further test my interpretation of the intermittent WGMs signal being caused by emulsified SOA particles in the NaCl(aq) core (Figure 9.2). A pure squalane particle was trapped and then at 0 minutes in Figure 9.4 aqueous NaCl was added through coagulation. After this first coagulation the RH was decreased to below the efflouresce relative humidity (ERH) of the NaCl, which is 45%[115]. After the salt should have effloresced the presence of the WGMs are still observed. This indicates the NaCl crystal phase was not transported to the surface of the squalane droplet where it would quench the WGMs. At 15 minutes the RH was increased above the deliquescence RH (DRH) of NaCl. The WGMs have a positive slope indicating water uptake by NaCl which confirms that I can deliquesce the NaCl crystal that is inside a squalane droplet.

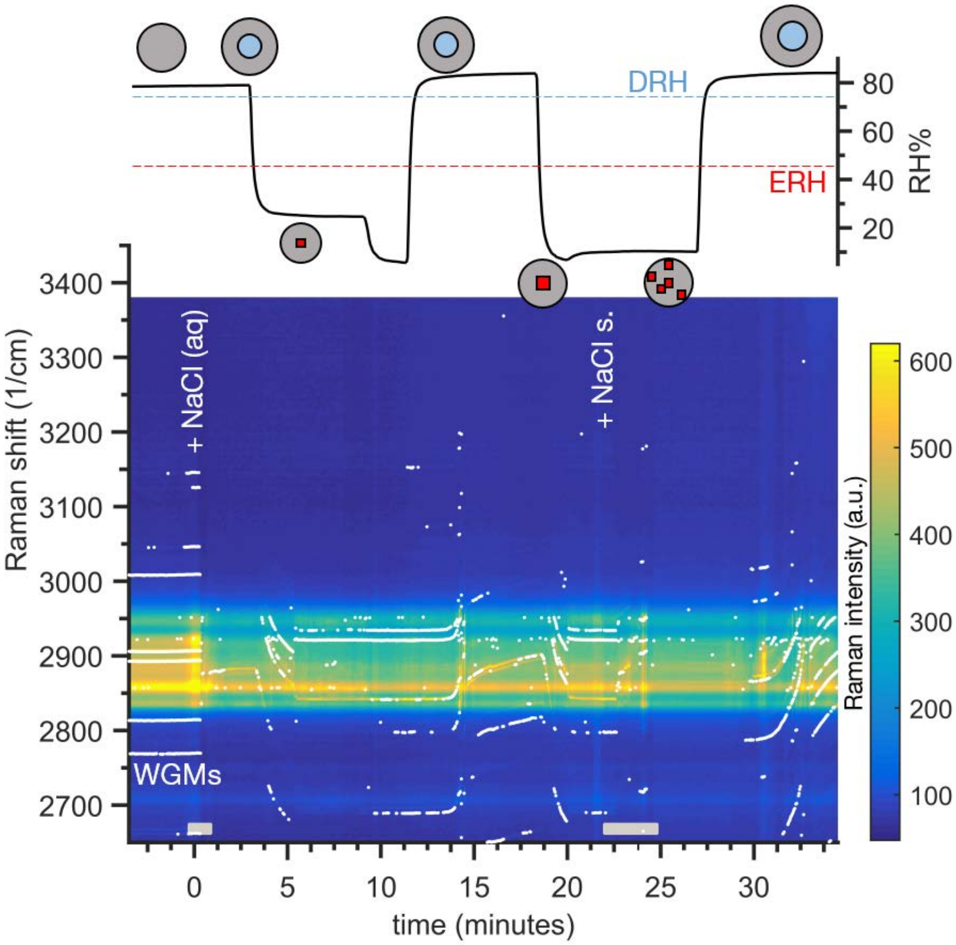

Figure 9.4. Time series of a trapped squalane droplet to which aqueous and then solid NaCl aerosol was added by coagulation, indicated by the gray bars. The efflorescence RH (ERH) and deliquescence RH (DRH) of NaCl are indicated by a dashed line, red and blue respectively. The first addition of NaCl(aq) was at 0 minutes, then followed by a decrease and then increase in RH to cause an efflorescence and deliquescence cycle of the NaCl phase. NaCl(s) crystals were added to the droplet at low RH at 22 min, and this produced intermittent quenching of the WGMs. The paucity of WGMs in the 25-29 min. period indicates that the NaCl(s) crystals that coagulated with the droplet did not cluster in the droplet's center but remained near the surface of the squalane where the WGMs resonate.

I then investigated if effloresced NaCl crystals would remain near the surface when coagulated with the droplet. To explore this, solid NaCl particles were added to the same squalane coated NaCl droplet through coagulation while maintaining the chamber RH below NaCl's ERH (22 to 25 min). This also caused the NaCl phase already in the droplet to effloresce again. There is a distinct absence of WGMs in the period from 25 to 29 minutes following the coagulation of crystalized NaCl particles. From this I can conclude that the NaCl crystals remained near the surface, interfering with the resonant amplification process of the WGMs. The WGMs were restored when the RH was increased above the DRH of NaCl at 30 minutes. Note that the Raman O-H band is not strong throughout this experiment, indicating that the squalane shell (from the original trapped pure squalane droplet) was thick enough such that the WGMs existed entirely in the squalane phase and did not sample the solid or liquid aqueous NaCl phase at the center of the droplet. From the interfacial spreading coefficients and prior AOT experiments I know that squalane would form a shell around aqueous NaCl[108]. The intermittent WGM signal observed when solid NaCl particles were present in the surface layer of the squalane is similar to the weak WGM signal observed when SOA was added to the NaCl(aq) droplet. This similarity in the Raman spectra further supports my interpretation of the weak WGM signal being caused by small emulsified solid or liquid particles that interfere with the light path of the resonating WGM wavelengths.

9.5 Evaporation Rate and Vapor Pressure Calculation

The calculation of vapor pressures of evaporating droplets has been previously studied and is based on fundamental mass transport theory[101,111,139,186,213–215]. My formulation of evaporation rate in Eqn. (9.1) follows the work by Cai et al. (2014) except I simplify my equations assuming the composition remains constant, which is done as the humidity was not being varied significantly.

$$\frac{1}{r_c}\frac{dm_c}{dt} = 4\pi\frac{M_c D_{c,vapor}}{RT}\Delta P \tag{9.1}$$

Where m_c is the mass of the core, r_c is the radius of the core, M_c is the molecular weight of the core, $D_{c,vapor}$ is the gas phase diffusion coefficient of the core species, ΔP the change in partial pressure at the surface and bulk air flow, R is the gas constant, and T is temperature in Kelvin.

By substituting the mass of the core for the density (ρ_c) and volume I derive Eqn. (2), which is used to calculate the evaporation rate.

$$r_c\frac{dr_c}{dt} = \frac{M_c D_{c,vapor}}{RT\rho_c}\Delta P \tag{9.2}$$

Due to the trapping method of the glycerol droplet, which results in the cover slip being coated with glycerol droplets, my partial pressure in the bulk air flow is not zero. This results in slowing the evaporation of the glycerol droplet. This is why I compare the relative evaporation rate when SOM is added to the glycerol droplet.

The derivation of the evaporation rate of the core, in a core-shell droplet, makes two simplifying assumptions. The first is that the core species evaporation rate is much less than that of the shell species and the second being that diffusion through the shell is not the rate limiting step. With those assumptions, I then derive Eqns. 9.3 and 9.4, where r_s is the radius of the shell.

$$\frac{1}{r_s}\frac{dm_c}{dt} = 4\pi\frac{M_c D_{c,vapor}}{RT}\,\Delta \mathrm{P} \tag{9.3}$$

$$\frac{r_c^2}{r_s}\frac{dr_c}{dt} = \frac{M_c D_{c,vapor}}{RT\rho_c}\,\Delta P \tag{9.4}$$

If there were a diffusion limitation in the shell, this would decrease the observed evaporation rate when using Eqn. (4). A decrease in the partial pressure due to Raoult's law would also show up as a decrease in observed evaporation rate. Using the homogeneous fit from the glycerol droplet before the SOA was added the resulting average evaporation rate calculated via Eqn. (9.2), was -194 nm^2/s. After the SOA was added the average core evaporation rate calculated via Eqn. (9.4), was -151 nm^2/s. The addition of the SOA shell resulted in a 22% decrease in the evaporation rate.

The evaporation rate of the shell is similar to the homogeneous case (Eqn. 9.1) except I have to account for only the volume change due to the shell phase.

$$\frac{1}{r_s}\frac{dm_s}{dt} = 4\pi\frac{M_s D_{s,vapor}}{RT}\,\Delta P \tag{9.5}$$

$$r_s\frac{dr_s}{dt} - \frac{r_c^2}{r_s}\frac{dr_c}{dt} = \frac{M_s D_{s,vapor}}{RT\rho_s}\,\Delta \mathrm{P} \tag{9.6}$$

Using the fitted timeseries I can calculate the evaporation rate for the shell and then retrieve an effective vapor pressure of the SOA phase. The unit conversion from vapor pressure to volatility follows from the ideal gas law, Eqn. (9.7). As this is an effective vapor pressure I'm observing a C* and not individual component volatilities (C).

$$C = \frac{M\, p_{vapor}}{RT} \tag{9.7}$$

10 Appendix D

Supplemental Information for Chapter 5: The morphologies of a-pinene secondary organic aerosol determined at low humidity using aerosol optical tweezers

10.1 Morphology of Dry SOA Added to a Hydrophobic Organic Droplet

In Figure 10.1 I show the results of adding α-pinene SOA to a squalane droplet under dry RH conditions. Due to the complexity of the C-H Raman mode I'm unable to consistently separate the false positive peaks from the real WGMs. This left us only able to use the homogeneous fit model as there are not enough peaks for the core-shell fit. I see that the after the SOA addition the peak error increased and the fit dimeters are inconsistent after 400 min. Using this evidence I can conclude that the SOA was being added to the surface of the droplet and thus was a core-shell morphology with SOA as the shell.

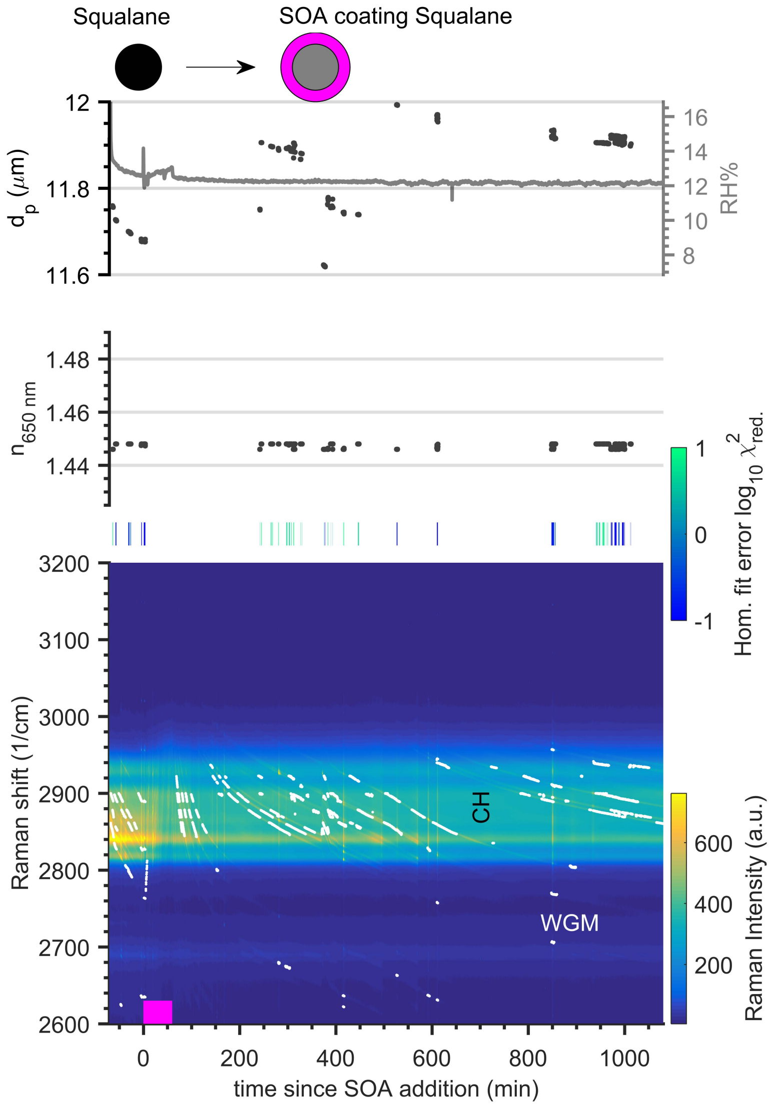

Figure 10.1. Raman spectral time series for a tweezed squalane droplet with the addition of α-pinene SOA, at 12.5% RH. Raman spectra are shown in the bottom graph, and the white points indicate the positions of detectable whispering gallery modes (WGMs). The decreasing slope of the WGM traces indicates the droplet is evaporating. The α-pinene SOA flow reaction started at 0 min and lasted for 60 min, indicated by the pink bar. The droplet's refractive index and diameter retrieved from the Homogeneous WGM analysis are shown in the middle and top panels (black dots). The fit error for the homogeneous model is shown in the green/blue bar, where consistently blue indicates a valid fit and green indicates an invalid fit to the model. Along with the low fit error the decreasing droplet size should be self-consistent, which it is not after 400 min, indicating an invalid fit.

10.2 Interfacial Tensions with Water

I compiled in Figure 10.2 the interfacial tension with water for a range of organic compounds that have an O:C ratio greater than zero. I also only graphed the compounds that phase-separate with water (O:C<0.6). The trend is clearly decreasing interfacial tension with increasing O:C ratio. I used this evidence to justify the likely morphology of an OA phase plus an aqueous phase being a core-shell morphology in the atmosphere.

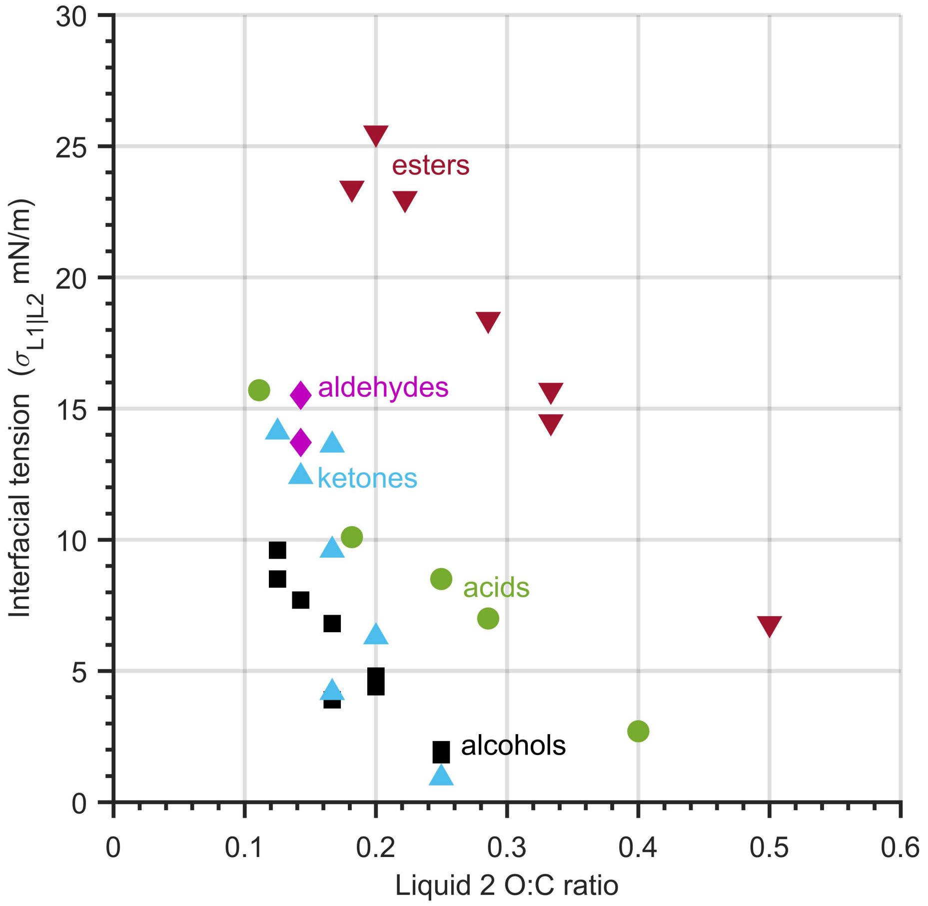

Figure 10.2. Interfacial tension between water and an organic compound. This was compiled for a different organic classes vs the oxygen to carbon ratio (O:C) [202,203].

References

1. Myhre G, Shindell D, Bréon F-M, Collins W, Fuglestvedt J, Huang J, Koch D, Lamarque J-F, Lee D, Mendoza B, et al. 2013: Anthropogenic and Natural Radiative Forcing. Climate Change 2013: The Physical Science Basis. Contribution of Working Group I to the Fifth Assessment Report of the Intergovernmental Panel on Climate Change. 2013:659–740. doi:10.1017/CBO9781107415324.018

2. Pope CA, Ezzati M, Dockery DW. Fine-particulate air pollution and life expectancy in the United States. The New England journal of medicine. 2009;360(4):376–86. doi:10.1056/NEJMsa0805646

3. Kolb CE, Worsnop DR. Chemistry and Composition of Atmospheric Aerosol Particles. Annual Review of Physical Chemistry. 2012;63(1):471–491. doi:10.1146/annurev-physchem-032511-143706

4. Pöschl U. Atmospheric Aerosols: Composition, Transformation, Climate and Health Effects. Angewandte Chemie International Edition. 2005;44(46):7520–7540. doi:10.1002/anie.200501122

5. Gentner DR, Isaacman G, Worton DR, Chan AWH, Dallmann TR, Davis L, Liu S, Day DA, Russell LM, Wilson KR, et al. Elucidating secondary organic aerosol from diesel and gasoline vehicles through detailed characterization of organic carbon emissions. Proceedings of the National Academy of Sciences of the United States of America. 2012;109(45):18318–23. doi:10.1073/pnas.1212272109

6. Hallquist M, Wenger JC, Baltensperger U, Rudich Y, Simpson D, Claeys M, Dommen J, Donahue NM, George C, Goldstein AH, et al. The formation, properties and impact of secondary organic aerosol: current and emerging issues. Atmospheric Chemistry and Physics. 2009;9(14):5155–5236. doi:10.5194/acp-9-5155-2009

7. Zhang Q, Jimenez JL, Canagaratna MR, Allan JD, Coe H, Ulbrich I, Alfarra MR, Takami A, Middlebrook AM, Sun YL, et al. Ubiquity and dominance of oxygenated species in organic aerosols in anthropogenically-influenced Northern Hemisphere midlatitudes. Geophysical Research Letters. 2007;34(13):1–6. doi:10.1029/2007GL029979

8. Surratt JD, Murphy SM, Kroll JH, Ng NL, Hildebrandt L, Sorooshian A, Szmigielski R, Vermeylen R, Maenhaut W, Claeys M, et al. Chemical Composition of Secondary

Organic Aerosol Formed from the Photooxidation of Isoprene. The Journal of Physical Chemistry A. 2006;110(31):9665–9690. doi:10.1021/jp061734m

9. Robinson ES, Saleh R, Donahue NM. Probing the Evaporation Dynamics of Mixed SOA/Squalane Particles Using Size-Resolved Composition and Single-Particle Measurements. Environmental Science & Technology. 2015;49(16):9724–9732. doi:10.1021/acs.est.5b01692

10. Zhao Y, Wingen LM, Perraud V, Finlayson-Pitts BJ. Phase, composition, and growth mechanism for secondary organic aerosol from the ozonolysis of alpha-cedrene. Atmospheric Chemistry and Physics. 2016;16(5):3245–3264. doi:10.5194/acp-16-3245-2016

11. Riemer N, Vogel H, Vogel B, Anttila T, Kiendler-Scharr A, Mentel TF. Relative importance of organic coatings for the heterogeneous hydrolysis of N 2 O 5 during summer in Europe. Journal of Geophysical Research. 2009;114(D17):D17307. doi:10.1029/2008JD011369

12. McNeill VF, Patterson J, Wolfe GM, Thornton JA. The effect of varying levels of surfactant on the reactive uptake of N_2O_5 to aqueous aerosol. Atmospheric Chemistry and Physics. 2006;6(6):1635–1644. doi:10.5194/acp-6-1635-2006

13. Hallquist M, Stewart DJ, Baker J, Cox RA. Hydrolysis of N2O5 on Submicron Sulfuric Acid Aerosols. The Journal of Physical Chemistry A. 2000;104(17):3984–3990. doi:10.1021/jp9939625

14. Park S-C, Burden DK, Nathanson GM. The Inhibition of N2O5 Hydrolysis in Sulfuric Acid by 1-Butanol and 1-Hexanol Surfactant Coatings. The Journal of Physical Chemistry A. 2007;111(15):2921–2929. doi:10.1021/jp068228h

15. Cosman LM, Knopf DA, Bertram AK. N2O5 reactive uptake on aqueous sulfuric acid solutions coated with branched and straight-chain insoluble organic surfactants. Journal of Physical Chemistry A. 2008;112(11):2386–2396. doi:10.1021/jp710685r

16. Escorcia EN, Sjostedt SJ, Abbatt JPD. Kinetics of N2O5 hydrolysis on secondary organic aerosol and mixed ammonium bisulfate-secondary organic aerosol particles. Journal of Physical Chemistry A. 2010;114(50):13113–13121. doi:10.1021/jp107721v

17. Riemer N, Vogel H, Vogel B, Anttila T, Kiendler-Scharr A, Mentel TF. Relative importance of organic coatings for the heterogeneous hydrolysis of N2O5 during summer in Europe. Journal of Geophysical Research Atmospheres. 2009;114(17):1–14. doi:10.1029/2008JD011369

18. Anttila T, Kiendler-Scharr A, Tillmann R, Mentel TF. On the reactive uptake of gaseous compounds by organic-coated aqueous aerosols: Theoretical analysis and application to the heterogeneous hydrolysis of N2O5. Journal of Physical Chemistry A. 2006;110(35):10435–10443. doi:10.1021/jp062403c

19. Shiraiwa M, Zuend A, Bertram AK, Seinfeld JH. Gas-particle partitioning of atmospheric aerosols: interplay of physical state, non-ideal mixing and morphology. Physical chemistry chemical physics : PCCP. 2013;15(27):11441–53. doi:10.1039/c3cp51595h

20. Zuend A, Marcolli C, Peter T, Seinfeld JH. Computation of liquid-liquid equilibria and phase stabilities: Implications for RH-dependent gas/particle partitioning of organic-inorganic aerosols. Atmospheric Chemistry and Physics. 2010;10(16):7795–7820. doi:10.5194/acp-10-7795-2010

21. Chang EI, Pankow JF. Prediction of activity coefficients in liquid aerosol particles containing organic compounds, dissolved inorganic salts, and water—Part 2: Consideration of phase separation effects by an X-UNIFAC model. Atmospheric Environment. 2006;40(33):6422–6436. doi:10.1016/j.atmosenv.2006.04.031

22. Seinfeld JH, Erdakos GB, Asher WE, Pankow JF. Modeling the Formation of Secondary Organic Aerosol (SOA). 2. The Predicted Effects of Relative Humidity on Aerosol Formation in the α-Pinene-, β-Pinene-, Sabinene-, Δ 3 -Carene-, and Cyclohexene-Ozone Systems. Environmental Science & Technology. 2001;35(9):1806–1817. doi:10.1021/es001765+

23. Wang J, Hoffmann AA, Park RJ, Jacob DJ, Martin ST. Global distribution of solid and aqueous sulfafte aerosols: Effect of the hysteresis of particle phase transitions. Journal of Geophysical Research Atmospheres. 2008;113(11). doi:10.1029/2007JD009367

24. Smith ML, Kuwata M, Martin ST. Secondary Organic Material Produced by the Dark Ozonolysis of α-Pinene Minimally Affects the Deliquescence and Efflorescence of Ammonium Sulfate. Aerosol Science and Technology. 2011;45(2):244–261. doi:10.1080/02786826.2010.532178

25. Takahama S, Pathak RK, Pandis SN. Efflorescence transitions of ammonium sulfate particles coated with secondary organic aerosol. Environmental Science and Technology. 2007;41(7):2289–2295. doi:10.1021/es0619915

26. Smith ML, You Y, Kuwata M, Bertram AK, Martin ST. Phase transitions and phase miscibility of mixed particles of ammonium sulfate, toluene-derived secondary organic material, and water. Journal of Physical Chemistry A. 2013;117(36):8895–8906. doi:10.1021/jp405095e

27. Drozd GT, Woo JL, McNeill VF. Self-limited uptake of α-pinene oxide to acidic aerosol: the effects of liquid–liquid phase separation and implications for the formation of secondary organic aerosol and organosulfates from epoxides. Atmospheric Chemistry and Physics. 2013;13(16):8255–8263. doi:10.5194/acp-13-8255-2013

28. Ciobanu G, Marcolli C, Krieger UK, Weers U, Peter T. Liquid-liquid phase separation in mixed organic-inorganic aerosols exposed to hygroscopic cycles. Geophysical Research Abstracts. 2008;Vol. 10, E:1.

29. Schill GP, Tolbert MA. Heterogeneous ice nucleation on phase-separated organic-sulfate particles: Effect of liquid vs. glassy coatings. Atmospheric Chemistry and Physics. 2013;13(9):4681–4695. doi:10.5194/acp-13-4681-2013

30. Song M, Marcolli C, Krieger UK, Zuend A, Peter T. Liquid-liquid phase separation in aerosol particles: Dependence on O:C, organic functionalities, and compositional complexity. Geophysical Research Letters. 2012;39(19):1–5. doi:10.1029/2012GL052807

31. Wheeler MJ, Bertram AK. Deposition nucleation on mineral dust particles: a case against classical nucleation theory with the assumption of a single contact angle. Atmospheric Chemistry and Physics. 2012;12(2):1189–1201. doi:10.5194/acp-12-1189-2012

32. Bertram AK, Martin ST, Hanna SJ, Smith ML, Bodsworth A, Chen Q, Kuwata M, Liu A, You Y, Zorn SR. Predicting the relative humidities of liquid-liquid phase separation, efflorescence, and deliquescence of mixed particles of ammonium sulfate, organic material, and water using the organic-to-sulfate mass ratio of the particle and the oxygen-to-carbon ele. Atmospheric Chemistry and Physics. 2011;11(21):10995–11006. doi:10.5194/acp-11-10995-2011

33. Martin ST, Hung H-M, Park RJ, Jacob DJ, Spurr RJD, Chance K V., Chin M. Effects of the physical state of tropospheric ammonium-sulfate-nitrate particles on global aerosol direct radiative forcing. Atmospheric Chemistry and Physics. 2004;4(1):183–214. doi:10.5194/acp-4-183-2004

34. Hekayati J, Roosta A, Javanmardi J. Liquid–liquid equilibria in the quinary aqueous two-phase system of poly(ethylene glycol) 6000+sodium sulfate+water in the presence of glucose and ethanol: Experimental investigation and thermodynamic modeling. Thermochimica Acta. 2016;625:47–52. doi:10.1016/j.tca.2015.12.013

35. Bateman AP, Gong Z, Liu P, Sato B, Cirino G, Zhang Y, Artaxo P, Bertram AK, Manzi AO, Rizzo L V., et al. Sub-micrometre particulate matter is primarily in liquid form over Amazon rainforest. Nature Geoscience. 2015;9(1):34–37. doi:10.1038/ngeo2599

36. O'Brien RE, Wang B, Kelly ST, Lundt N, You Y, Bertram AK, Leone SR, Laskin A, Gilles MK. Liquid–Liquid Phase Separation in Aerosol Particles: Imaging at the Nanometer Scale. Environmental Science & Technology. 2015;49(8):4995–5002. doi:10.1021/acs.est.5b00062

37. Song M, Marcolli C, Krieger UK, Zuend a., Peter T. Liquid-liquid phase separation and morphology of internally mixed dicarboxylic acids/ammonium sulfate/water particles. Atmospheric Chemistry and Physics. 2012;12(5):2691–2712. doi:10.5194/acp-12-2691-2012

38. Li YJ, Liu P, Gong Z, Wang Y, Bateman AP, Bergoend C, Bertram AK, Martin ST. Chemical Reactivity and Liquid/Nonliquid States of Secondary Organic Material. Environmental Science & Technology. 2015;49(22):13264–13274. doi:10.1021/acs.est.5b03392

39. Renbaum-Wolff L, Song M, Marcolli C, Zhang Y, Liu PF, Grayson JW, Geiger FM, Martin ST, Bertram AK. Observations and implications of liquid–liquid phase separation at high relative humidities in secondary organic material produced by *α*-pinene ozonolysis without inorganic salts. Atmospheric Chemistry and Physics. 2016;16(12):7969–7979. doi:10.5194/acp-16-7969-2016

40. You Y, Bertram AK. Effects of molecular weight and temperature on liquid–liquid phase separation in particles containing organic species and inorganic salts. Atmospheric Chemistry and Physics. 2015;15(3):1351–1365. doi:10.5194/acp-15-1351-2015

41. You Y, Renbaum-Wolff L, Carreras-Sospedra M, Hanna SJ, Hiranuma N, Kamal S, Smith ML, Zhang X, Weber RJ, Shilling JE, et al. Images reveal that atmospheric particles can undergo liquid-liquid phase separations. Proceedings of the National Academy of Sciences of the United States of America. 2012;109(33):13188–93. doi:10.1073/pnas.1206414109

42. You Y, Smith ML, Song M, Martin ST, Bertram AK. Liquid–liquid phase separation in atmospherically relevant particles consisting of organic species and inorganic salts. International Reviews in Physical Chemistry. 2014;33(1):43–77. doi:10.1080/0144235X.2014.890786

43. Qiu Y, Molinero V. Morphology of Liquid–Liquid Phase Separated Aerosols. Journal of the American Chemical Society. 2015;137(33):10642–10651. doi:10.1021/jacs.5b05579

44. Stewart DJ, Cai C, Nayler J, Preston TC, Reid JP, Krieger UK, Marcolli C, Zhang YH. Liquid–Liquid Phase Separation in Mixed Organic/Inorganic Single Aqueous Aerosol Droplets. The Journal of Physical Chemistry A. 2015;119(18):4177–4190. doi:10.1021/acs.jpca.5b01658

45. Ciobanu VG, Marcolli C, Krieger UK, Weers U, Peter T. Liquid−Liquid Phase Separation in Mixed Organic/Inorganic Aerosol Particles. The Journal of Physical Chemistry A. 2009;113(41):10966–10978. doi:10.1021/jp905054d

46. Song M, Marcolli C, Krieger UK, Lienhard DM, Peter T. Morphologies of mixed organic/inorganic/aqueous aerosol droplets. Faraday Discussions. 2013;165:289–316. doi:10.1039/c3fd00049d

47. Buajarern J, Mitchem L, Reid JP. Characterizing Multiphase Organic/Inorganic/Aqueous Aerosol Droplets. The Journal of Physical Chemistry A. 2007;111(37):9054–9061. doi:10.1021/jp074366a

48. Reid JP, Dennis-Smither BJ, Kwamena N-OA, Miles REH, Hanford KL, Homer CJ. The morphology of aerosol particles consisting of hydrophobic and hydrophilic phases: hydrocarbons, alcohols and fatty acids as the hydrophobic component. Physical chemistry chemical physics : PCCP. 2011;13(34):15559–15572. doi:10.1039/c1cp21510h

49. Platt SM, El Haddad I, Zardini a. a., Clairotte M, Astorga C, Wolf R, Slowik JG, Temime-Roussel B, Marchand N, Ježek I, et al. Secondary organic aerosol formation from gasoline vehicle emissions in a new mobile environmental reaction chamber. Atmospheric Chemistry and Physics. 2013;13(18):9141–9158. doi:10.5194/acp-13-9141-2013

50. Abramson E, Imre D, Beránek J, Wilson J, Zelenyuk A. Experimental determination of chemical diffusion within secondary organic aerosol particles. Physical Chemistry Chemical Physics. 2013;15(8):2983–2991. doi:10.1039/c2cp44013j

51. Vaden TD, Imre D, Beránek J, Shrivastava M, Zelenyuk A. Evaporation kinetics and phase of laboratory and ambient secondary organic aerosol. Proceedings of the National Academy of Sciences of the United States of America. 2011;108(6):2190–2195. doi:10.1073/pnas.1013391108

52. Dennis-Smither BJ, Hanford KL, Kwamena NA, Miles REH, Reid JP. Phase, morphology, and hygroscopicity of mixed oleic acid/sodium chloride/water aerosol particles before and after ozonolysis. The journal of physical chemistry. A. 2012;116(24):6159–68. doi:10.1021/jp211429f

53. Buajarern J, Mitchem L, Reid JP. Characterizing the Formation of Organic Layers on the Surface of Inorganic/Aqueous Aerosols by Raman Spectroscopy. The Journal of Physical Chemistry A. 2007;111(46):11852–11859. doi:10.1021/jp075021v

54. Kwamena N-OA, Buajarern J, Reid JP. Equilibrium morphology of mixed organic/inorganic/aqueous aerosol droplets: investigating the effect of relative

humidity and surfactants. The journal of physical chemistry. A. 2010;114(18):5787–95. doi:10.1021/jp1003648

55. Metcalf AR, Boyer HC, Dutcher CS. Interfacial Tensions of Aged Organic Aerosol Particle Mimics Using a Biphasic Microfluidic Platform. Environmental Science & Technology. 2016;50(3):1251–1259. doi:10.1021/acs.est.5b04880

56. Shiraiwa M, Pfrang C, Koop T, Pöschl U. Kinetic multi-layer model of gas-particle interactions in aerosols and clouds (KM-GAP): linking condensation, evaporation and chemical reactions of organics, oxidants and water. Atmospheric Chemistry and Physics. 2012;12(5):2777–2794. doi:10.5194/acp-12-2777-2012

57. Lu JW, Rickards AMJ, Walker JS, Knox KJ, Miles REH, Reid JP, Signorell R. Timescales of water transport in viscous aerosol: measurements on sub-micron particles and dependence on conditioning history. Phys. Chem. Chem. Phys. 2014;16(21):9819–9830. doi:10.1039/C3CP54233E

58. Davies JF, Haddrell AE, Miles REH, Bull CR, Reid JP. Bulk, surface, and gas-phase limited water transport in aerosol. The journal of physical chemistry. A. 2012;116(45):10987–98. doi:10.1021/jp3086667

59. Abbatt JPD, Lee AKY, Thornton JA. Quantifying trace gas uptake to tropospheric aerosol: recent advances and remaining challenges. Chemical Society Reviews. 2012;41(19):6555–6581. doi:10.1039/c2cs35052a

60. Pajunoja A, Malila J, Hao L, Joutsensaari J, Lehtinen KEJ, Virtanen A. Estimating the Viscosity Range of SOA Particles Based on Their Coalescence Time. Aerosol Science and Technology. 2014;48(2):i–iv. doi:10.1080/02786826.2013.870325

61. Koop T, Bookhold J, Shiraiwa M, Pöschl U. Glass transition and phase state of organic compounds: dependency on molecular properties and implications for secondary organic aerosols in the atmosphere. Physical chemistry chemical physics : PCCP. 2011;13(43):19238–55. doi:10.1039/c1cp22617g

62. Kanakidou M, Seinfeld JH, Pandis SN, Barnes I, Dentener FJ, Facchini MC, Van Dingenen R, Ervens B, Nenes A, Nielsen CJ, et al. Organic aerosol and global climate modelling: a review. Atmospheric Chemistry and Physics. 2005;5(4):1053–1123. doi:10.5194/acp-5-1053-2005

63. Alexander B, Hastings MG, Allman DJ, Dachs J, Thornton J a., Kunasek S a. Quantifying atmospheric nitrate formation pathways based on a global model of the oxygen isotopic composition (Δ^{17}O) of atmospheric nitrate. Atmospheric Chemistry and Physics. 2009;9(14):5043–5056. doi:10.5194/acp-9-5043-2009

64. Shindell DT, Faluvegi G, Koch DM, Schmidt GA, Unger N, Bauer SE. Improved Attribution of Climate Forcing to Emissions. Science. 2009;326(5953):716–718. doi:10.1126/science.1174760

65. Evans MJ. Impact of new laboratory studies of N 2 O 5 hydrolysis on global model budgets of tropospheric nitrogen oxides, ozone, and OH. Geophysical Research Letters. 2005;32(9):L09813. doi:10.1029/2005GL022469

66. Kane SM, Caloz F, Leu M-T. Heterogeneous Uptake of Gaseous N 2 O 5 by (NH 4) 2 SO 4 , NH 4 HSO 4 , and H 2 SO 4 Aerosols. The Journal of Physical Chemistry A. 2001;105(26):6465–6470. doi:10.1021/jp010490x

67. Ryder OS, Ault AP, Cahill JF, Guasco TL, Riedel TP, Cuadra-Rodriguez LA, Gaston CJ, Fitzgerald E, Lee C, Prather KA, et al. On the role of particle inorganic mixing state in the reactive uptake of N2O5 to ambient aerosol particles. Environmental Science and Technology. 2014;48(3):1618–1627. doi:10.1021/es4042622

68. Hallquist M, Stewart DJ, Stephenson SK, Anthony Cox R. Hydrolysis of N2O5 on sub-micron sulfate aerosols. Physical Chemistry Chemical Physics. 2003;5(16):3453. doi:10.1039/b301827j

69. Behnke W, George C, Scheer V, Zetzsch C. Production and decay of ClNO 2 from the reaction of gaseous N 2 O 5 with NaCl solution: Bulk and aerosol experiments. Journal of Geophysical Research: Atmospheres. 1997;102(D3):3795–3804. doi:10.1029/96JD03057

70. Folkers M, Mentel TF, Wahner A. Influence of an organic coating on the reactivity of aqueous aerosols probed by the heterogeneous hydrolysis of N 2 O 5. Geophysical Research Letters. 2003;30(12):46p1-46p4. doi:10.1029/2003GL017168

71. Fried A, Henry BE, Calvert JG, Mozurkewich M. The reaction probability of N 2 O 5 with sulfuric acid aerosols at stratospheric temperatures and compositions. Journal of Geophysical Research. 1994;99(D2):3517. doi:10.1029/93JD01907

72. Hu JH, Abbatt JPD. Reaction probabilities for N2O5 hydrolysis on sulfuric acid and ammonium sulfate aerosols at room temperature. J. Phys. Chem. A. 1997;101(5):871–878. doi:10.1021/jp9627436

73. Mozurkewich M, Calvert JG. Reaction probability of N 2 O 5 on aqueous aerosols. Journal of Geophysical Research. 1988;93(D12):15889. doi:10.1029/JD093iD12p15889

74. Thornton JA, Braban CF, Abbatt JPD. N2O5 hydrolysis on sub-micron organic aerosols: the effect of relative humidity, particle phase, and particle size. Phys. Chem. Chem. Phys. 2003;5(20):4593–4603. doi:10.1039/b307498f

75. Chang WL, Bhave P V, Brown SS, Riemer N, Stutz J, Dabdub D. Heterogeneous Atmospheric Chemistry, Ambient Measurements, and Model Calculations of N 2 O 5 : A Review. Aerosol Science and Technology. 2011;45(6):665–695. doi:10.1080/02786826.2010.551672

76. Gaston CJ, Thornton JA. Reacto-Diffusive Length of N 2 O 5 in Aqueous Sulfate- and Chloride-Containing Aerosol Particles. The Journal of Physical Chemistry A. 2016;120(7):1039–1045. doi:10.1021/acs.jpca.5b11914

77. Kolb CE, Cox RA, Abbatt JPD, Ammann M, Davis EJ, Donaldson DJ, Garrett BC, George C, Griffiths PT, Hanson DR, et al. An overview of current issues in the uptake of atmospheric trace gases by aerosols and clouds. Atmospheric Chemistry and Physics. 2010;10(21):10561–10605. doi:10.5194/acp-10-10561-2010

78. Surratt JD, Kroll JH, Kleindienst TE, Edney EO, Claeys M, Sorooshian A, Ng NL, Offenberg JH, Lewandowski M, Jaoui M, et al. Evidence for Organosulfates in Secondary Organic Aerosol. Environmental Science & Technology. 2007;41(2):517–527. doi:10.1021/es062081q

79. Pratt KA, Fiddler MN, Shepson PB, Carlton AG, Surratt JD. Organosulfates in cloud water above the Ozarks' isoprene source region. Atmospheric Environment. 2013;77:231–238. doi:10.1016/j.atmosenv.2013.05.011

80. Robinson NH, Hamilton JF, Allan JD, Langford B, Oram DE, Chen Q, Docherty K, Farmer DK, Jimenez JL, Ward MW, et al. Evidence for a significant proportion of Secondary Organic Aerosol from isoprene above a maritime tropical forest. Atmospheric Chemistry and Physics. 2011;11(3):1039–1050. doi:10.5194/acp-11-1039-2011

81. Surratt JD, Lewandowski M, Offenberg JH, Jaoui M, Kleindienst TE, Edney EO, Seinfeld JH. Effect of Acidity on Secondary Organic Aerosol Formation from Isoprene. Environmental Science & Technology. 2007;41(15):5363–5369. doi:10.1021/es0704176

82. Surratt JD, Chan AWH, Eddingsaas NC, Chan M, Loza CL, Kwan a J, Hersey SP, Flagan RC, Wennberg PO, Seinfeld JH. Reactive intermediates revealed in secondary organic aerosol formation from isoprene. Proceedings of the National Academy of Sciences. 2010;107(15):6640–6645. doi:10.1073/pnas.0911114107

83. Lin Y-H, Zhang Z, Docherty KS, Zhang H, Budisulistiorini SH, Rubitschun CL, Shaw SL, Knipping EM, Edgerton ES, Kleindienst TE, et al. Isoprene Epoxydiols as Precursors to Secondary Organic Aerosol Formation: Acid-Catalyzed Reactive Uptake Studies with Authentic Compounds. Environmental Science & Technology. 2012;46(1):250–258. doi:10.1021/es202554c

84. Hatch LE, Creamean JM, Ault AP, Surratt JD, Chan MN, Seinfeld JH, Edgerton ES, Su Y, Prather KA. Measurements of Isoprene-Derived Organosulfates in Ambient Aerosols by Aerosol Time-of-Flight Mass Spectrometry - Part 1: Single Particle Atmospheric Observations in Atlanta. Environmental Science & Technology. 2011;45(12):5105–5111. doi:10.1021/es103944a

85. Hu WW, Campuzano-Jost P, Palm BB, Day DA, Ortega AM, Hayes PL, Krechmer JE, Chen Q, Kuwata M, Liu YJ, et al. Characterization of a real-time tracer for isoprene epoxydiols-derived secondary organic aerosol (IEPOX-SOA) from aerosol mass spectrometer measurements. Atmospheric Chemistry and Physics. 2015;15(20):11807–11833. doi:10.5194/acp-15-11807-2015

86. Chan MN, Surratt JD, Claeys M, Edgerton ES, Tanner RL, Shaw SL, Zheng M, Knipping EM, Eddingsaas NC, Wennberg PO, et al. Characterization and Quantification of Isoprene-Derived Epoxydiols in Ambient Aerosol in the Southeastern United States. Environmental Science & Technology. 2010;44(12):4590–4596. doi:10.1021/es100596b

87. Paulot F, Crounse JD, Kjaergaard HG, Kurten A, St. Clair JM, Seinfeld JH, Wennberg PO. Unexpected Epoxide Formation in the Gas-Phase Photooxidation of Isoprene. Science. 2009;325(5941):730–733. doi:10.1126/science.1172910

88. Kroll JH, Ng NL, Murphy SM, Flagan RC, Seinfeld JH. Secondary Organic Aerosol Formation from Isoprene Photooxidation. Environmental Science & Technology. 2006;40(6):1869–1877. doi:10.1021/es0524301

89. Claeys M. Formation of Secondary Organic Aerosols Through Photooxidation of Isoprene. Science. 2004;303(5661):1173–1176. doi:10.1126/science.1092805

90. Carlton AG, Wiedinmyer C, Kroll JH. A review of Secondary Organic Aerosol (SOA) formation from isoprene. Atmospheric Chemistry and Physics. 2009;9(14):4987–5005. doi:10.5194/acp-9-4987-2009

91. Gaston CJ, Riedel TP, Zhang Z, Gold A, Surratt JD, Thornton J a. Reactive Uptake of an Isoprene-Derived Epoxydiol to Submicron Aerosol Particles. Environmental Science & Technology. 2014;48(19):11178–11186. doi:10.1021/es5034266

92. Cole-Filipiak NC, O'Connor AE, Elrod MJ. Kinetics of the hydrolysis of atmospherically relevant isoprene-derived hydroxy epoxides. Environmental Science and Technology. 2010;44(17):6718–6723. doi:10.1021/es1019228

93. Zhang H, Surratt JD, Lin YH, Bapat J, Kamens RM. Effect of relative humidity on SOA formation from isoprene/NO photooxidation: enhancement of 2-methylglyceric acid and its corresponding oligoesters under dry conditions. Atmospheric Chemistry and Physics. 2011;11(13):6411–6424. doi:10.5194/acp-11-6411-2011

94. He Q-F, Ding X, Wang X-M, Yu J-Z, Fu X-X, Liu T-Y, Zhang Z, Xue J, Chen D-H, Zhong L-J, et al. Organosulfates from Pinene and Isoprene over the Pearl River Delta, South China: Seasonal Variation and Implication in Formation Mechanisms. Environmental science & technology. 2014;48(16):9236–45. doi:10.1021/es501299v

95. Song C, Zaveri RA, Shilling JE, Alexander ML, Newburn M. Effect of hydrophilic organic seed aerosols on secondary organic aerosol formation from ozonolysis of α-pinene. Environmental Science and Technology. 2011;45(17):7323–7329. doi:10.1021/es201225c

96. Gordon CA, Ye J, Chan AWH. Secondary Organic Aerosol Formation Enhanced by Organic Seeds of Similar Polarity at Atmospherically Relative Humidity. STEM Fellowship Journal. 2015;1(2):6–10. doi:10.17975/sfj-2015-009

97. Ye J, Gordon CA, Chan AWH. Enhancement in Secondary Organic Aerosol Formation in the Presence of Preexisting Organic Particle. Environmental Science and Technology. 2016;50(7):3572–3579. doi:10.1021/acs.est.5b05512

98. Liu P, Li YJ, Wang Y, Gilles MK, Zaveri RA, Bertram AK, Martin ST. Lability of secondary organic particulate matter. Proceedings of the National Academy of Sciences. 2016;113(45):12643–12648. doi:10.1073/pnas.1603138113

99. Veghte DP, Altaf MB, Freedman MA. Size Dependence of the Structure of Organic Aerosol. Journal of the American Chemical Society. 2013;135(43):16046–16049. doi:10.1021/ja408903g

100. Reid JP, Mitchem L. LASER PROBING OF SINGLE-AEROSOL DROPLET DYNAMICS. Annual Review of Physical Chemistry. 2006;57(1):245–271. doi:10.1146/annurev.physchem.57.032905.104621

101. Cotterell MI, Mason BJ, Carruthers AE, Walker JS, Orr-Ewing AJ, Reid JP. Measurements of the evaporation and hygroscopic response of single fine-mode aerosol particles using a Bessel beam optical trap. Physical chemistry chemical physics : PCCP. 2014;16(5):2118–28. doi:10.1039/c3cp54368d

102. Porfirev AP, Skidanov R V. Optical trapping and manipulation of light-absorbing particles by means of a Hermite–Gaussian laser beam. Journal of Optical Technology. 2015;82(9):587. doi:10.1364/JOT.82.000587

103. Wills JB, Knox KJ, Reid JP. Optical control and characterisation of aerosol. Chemical Physics Letters. 2009;481(4–6):153–165. doi:10.1016/j.cplett.2009.09.020

104. Yang JJ, Huang M, Yu J, Lan YZ. Surface whispering-gallery mode. Europhysics Letters. 2011;96(5):1–5. doi:10.1209/0295-5075/96/57003

105. Matsko AB, Ilchenko VS. Optical resonators with whispering-gallery modes-part I: basics. IEEE Journal of Selected Topics in Quantum Electronics. 2006;12(1):3–14. doi:10.1109/JSTQE.2005.862952

106. Preston TC, Reid JP. Determining the size and refractive index of microspheres using the mode assignments from Mie resonances. Journal of the Optical Society of America A. 2015;32(11):2210–2217. doi:10.1364/JOSAA.32.002210

107. Preston TC, Reid JP. Accurate and efficient determination of the radius, refractive index, and dispersion of weakly absorbing spherical particle using whispering gallery modes. Journal of the Optical Society of America B-Optical Physics. 2013;30(8):2113–2122. doi:10.1364/josab.30.002113

108. Gorkowski K, Beydoun H, Aboff M, Walker JS, Reid JP, Sullivan RC. Advanced aerosol optical tweezers chamber design to facilitate phase-separation and equilibration timescale experiments on complex droplets. Aerosol Science and Technology. 2016;50(12):1327–1341. doi:10.1080/02786826.2016.1224317

109. Stewart DJ, Cai C, Nayler J, Preston TC, Reid JP, Krieger UK, Marcolli C, Zhang Y-HH. Liquid–Liquid Phase Separation in Mixed Organic/Inorganic Single Aqueous Aerosol Droplets. The Journal of Physical Chemistry A. 2015;119(18):4177–4190. doi:10.1021/acs.jpca.5b01658

110. Cai C, Tan S, Chen H, Ma J, Wang Y, Reid JP, Zhang Y. Slow water transport in MgSO 4 aerosol droplets at gel-forming relative humidities. Phys. Chem. Chem. Phys. 2015;17(44):29753–29763. doi:10.1039/C5CP05181A

111. Cai C, Stewart DJ, Preston TC, Walker JS, Zhang YH, Reid JP. A new approach to determine vapour pressures and hygroscopicities of aqueous aerosols containing semi-volatile organic compounds. Physical chemistry chemical physics : PCCP. 2014;16(7):3162–72. doi:10.1039/c3cp54948h

112. Rickards AMJ, Miles REH, Davies JF, Marshall FH, Reid JP. Measurements of the sensitivity of aerosol hygroscopicity and the κ parameter to the O/C ratio. The journal of physical chemistry. A. 2013;117(51):14120–31. doi:10.1021/jp407991n

113. Hopkins RJ, Mitchem L, Ward AD, Reid JP. Control and characterisation of a single aerosol droplet in a single-beam gradient-force optical trap. Physical Chemistry Chemical Physics. 2004;6(21):4924–4927. doi:10.1039/b414459g

114. Redding B, Schwab M, Pan Y. Raman Spectroscopy of Optically Trapped Single Biological Micro-Particles. Sensors. 2015;15(8):19021–19046. doi:10.3390/s150819021

115. Davis RD, Lance S, Gordon JA, Tolbert MA. Long Working-Distance Optical Trap for in Situ Analysis of Contact-Induced Phase Transformations. Analytical Chemistry. 2015;87(12):6186–6194. doi:10.1021/acs.analchem.5b00809

116. Power R, Reid JP, Anand S, McGloin D, Almohammedi a, Almohamedi a, Mistry NS, Hudson a J. Observation of the binary coalescence and equilibration of micrometer-sized droplets of aqueous aerosol in a single-beam gradient-force optical trap. The journal of physical chemistry. A. 2012;116(35):8873–84. doi:10.1021/jp304929t

117. Marsh A, Rovelli G, Song Y-C, Pereira KL, Willoughby RE, Bzdek BR, Hamilton JF, Orr-Ewing AJ, Topping DO, Reid JP. Accurate representations of the physicochemical properties of atmospheric aerosols: when are laboratory measurements of value? Faraday Discuss. 2017:1–19. doi:10.1039/C7FD00008A

118. Bzdek BR, Power RM, Simpson SH, Reid JP, Royall CP. Precise, contactless measurements of the surface tension of picolitre aerosol droplets. Chem. Sci. 2015;0:1–12. doi:10.1039/C5SC03184B

119. Rickards AMJ, Song Y-C, Miles REH, Preston TC, Reid JP. Variabilities and uncertainties in characterising water transport kinetics in glassy and ultraviscous aerosol. Phys. Chem. Chem. Phys. 2015;17(15):10059–10073. doi:10.1039/C4CP05383D

120. Lienhard DM, Bones DL, Zuend A, Krieger UK, Reid JP, Peter T. Measurements of thermodynamic and optical properties of selected aqueous organic and organic-inorganic mixtures of atmospheric relevance. The journal of physical chemistry. A. 2012;116(40):9954–68. doi:10.1021/jp3055872

121. Bones DL, Reid JP, Lienhard DM, Krieger UK. Comparing the mechanism of water condensation and evaporation in glassy aerosol. Proceedings of the National Academy of Sciences of the United States of America. 2012;109(29):11613–8. doi:10.1073/pnas.1200691109

122. Steimer SS, Krieger UK, Te Y-F, Lienhard DM, Huisman AJ, Luo BP, Ammann M, Peter T. Electrodynamic balance measurements of thermodynamic, kinetic, and optical aerosol properties inaccessible to bulk methods. Atmospheric Measurement Techniques. 2015;8(6):2397–2408. doi:10.5194/amt-8-2397-2015

123. Hargreaves G, Kwamena N-O a, Zhang YH, Butler JR, Rushworth S, Clegg SL, Reid JP. Measurements of the equilibrium size of supersaturated aqueous sodium chloride droplets at low relative humidity using aerosol optical tweezers and an electrodynamic balance. The journal of physical chemistry. A. 2010;114(4):1806–15. doi:10.1021/jp9095985

124. Tong HJ, Ouyang B, Nikolovski N, Lienhard DM, Pope FD, Kalberer M. A new electrodynamic balance (EDB) design for low-temperature studies: Application to immersion freezing of pollen extract bioaerosols. Atmospheric Measurement Techniques. 2015;8(3):1183–1195. doi:10.5194/amt-8-1183-2015

125. Thomas J-L, Marchiano R, Baresch D. Acoustical and optical radiation pressures and the development of single beam acoustical tweezers. Journal of Quantitative Spectroscopy and Radiative Transfer. 2017:1–11. doi:10.1016/j.jqsrt.2017.01.012

126. Murphy DM, Cziczo DJ, Froyd KD, Hudson PK, Matthew BM, Middlebrook a. M, Peltier RE, Sullivan A, Thomson DS, Weber RJ. Single-particle mass spectrometry of tropospheric aerosol particles. Journal of Geophysical Research. 2006;111(D23):D23S32. doi:10.1029/2006jd007340

127. Emanuelsson EU, Hallquist M, Kristensen K, Glasius M, Bohn B, Fuchs H, Kammer B, Kiendler-Scharr A, Nehr S, Rubach F, et al. Formation of anthropogenic secondary organic aerosol (SOA) and its influence on biogenic SOA properties. Atmospheric Chemistry and Physics. 2013;13(5):2837–2855. doi:10.5194/acp-13-2837-2013

128. Shen S-C, Wang YJ, Chen Y-Y. Design and fabrication of medical micro-nebulizer. Sensors and Actuators A: Physical. 2008;144(1):135–143. doi:10.1016/j.sna.2007.12.004

129. Ciobanu VG, Marcolli C, Krieger UK, Weers U, Peter T. Liquid−Liquid Phase Separation in Mixed Organic/Inorganic Aerosol Particles. The Journal of Physical Chemistry A. 2009;113(41):10966–10978. doi:10.1021/jp905054d

130. Verdeny I, Farré A, Mas J, López-Quesada C, Martín-Badosa E, Montes-Usategui M. Optical trapping: A review of essential concepts. Óptica Pura Y Aplicada. 2011;44:527–551.

131. Mitchem L, Reid JP. Optical manipulation and characterisation of aerosol particles using a single-beam gradient force optical trap. Chemical Society reviews. 2008;37(4):756–69. doi:10.1039/b609713h

132. Bzdek BR, Power RM, Simpson SH, Reid JP, Royall CP. Precise, contactless measurements of the surface tension of picolitre aerosol droplets. Chem. Sci. 2016;7(1):274–285. doi:10.1039/C5SC03184B

133. Robinson ES, Saleh R, Donahue NM. Organic Aerosol Mixing Observed by Single-Particle Mass Spectrometry. The Journal of Physical Chemistry A. 2013;117(51):13935–13945. doi:10.1021/jp405789t

134. Loza CL, Coggon MM, Nguyen TB, Zuend A, Flagan RC, Seinfeld JH. On the Mixing and Evaporation of Secondary Organic Aerosol Components. Environmental Science & Technology. 2013;47(12):6173–6180. doi:10.1021/es400979k

135. Bruns EA, El Haddad I, Keller A, Klein F, Kumar NK, Pieber SM, Corbin JC, Slowik JG, Brune WH, Baltensperger U, et al. Inter-comparison of laboratory smog chamber and flow reactor systems on organic aerosol yield and composition. Atmospheric Measurement Techniques. 2015;8(6):2315–2332. doi:10.5194/amt-8-2315-2015

136. Ortega AM, Day DA, Cubison MJ, Brune WH, Bon D, de Gouw JA, Jimenez JL. Secondary organic aerosol formation and primary organic aerosol oxidation from biomass-burning smoke in a flow reactor during FLAME-3. Atmospheric Chemistry and Physics. 2013;13(22):11551–11571. doi:10.5194/acp-13-11551-2013

137. Ray AK, Nandakumar R. Simultaneous determination of size and wavelength-dependent refractive indices of thin-layered droplets from optical resonances. Applied optics. 1995;34(33):7759–7770. doi:10.1364/AO.34.007759

138. Rheims J, Köser J, Wriedt T. Refractive-index measurements in the near-IR using an Abbe refractometer. Measurement Science and Technology. 1999;8(6):601–605. doi:10.1088/0957-0233/8/6/003

139. Cai C, Stewart DJ, Reid JP, Zhang Y, Ohm P, Dutcher CS, Clegg SL. Organic Component Vapor Pressures and Hygroscopicities of Aqueous Aerosol Measured by Optical Tweezers. The Journal of Physical Chemistry A. 2015;119(4):704–718. doi:10.1021/jp510525r

140. Dubey GP, Tripathi N, Bhatia SC. Refractive index of ternary liquid systems of squalane (+ hexane + benzene; + cyclohexane + benzene and + hexane + cyclohexane). Indian Journal of Pure and Applied Physics. 2005;43(3):175–179.

141. Tong H-J, Reid JP, Bones DL, Luo BP, Krieger UK. Measurements of the timescales for the mass transfer of water in glassy aerosol at low relative humidity and ambient temperature. Atmospheric Chemistry and Physics. 2011;11(10):4739–4754. doi:10.5194/acp-11-4739-2011

142. Hulst HC. Light scattering by small particles. New York: John Wiley & Sons; 1981.

143. Haddrell AE, Miles REH, Bzdek BR, Reid JP, Hopkins RJ, Walker JS. Coalescence Sampling and Analysis of Aerosols using Aerosol Optical Tweezers. Analytical Chemistry. 2017;89(4):2345–2352. doi:10.1021/acs.analchem.6b03979

144. Bzdek BR, Collard L, Sprittles JE, Hudson AJ, Reid JP. Dynamic measurements and simulations of airborne picolitre-droplet coalescence in holographic optical

tweezers. The Journal of Chemical Physics. 2016;145(5):54502. doi:10.1063/1.4959901

145. Power RM, Reid JP. Probing the micro-rheological properties of aerosol particles using optical tweezers. Reports on Progress in Physics. 2014;77(7):74601. doi:10.1088/0034-4885/77/7/074601

146. Miles REH, Walker JS, Burnham DR, Reid JP. Retrieval of the complex refractive index of aerosol droplets from optical tweezers measurements. Physical Chemistry Chemical Physics. 2012;14(9):3037. doi:10.1039/c2cp23999j

147. Walker JS, Wills JB, Reid JP, Wang L, Topping DO, Butler JR, Zhang Y-H. Direct comparison of the hygroscopic properties of ammonium sulfate and sodium chloride aerosol at relative humidities approaching saturation. The journal of physical chemistry. A. 2010;114(48):12682–12691. doi:10.1021/jp107802y

148. Mason BJ, King S-J, Miles REH, Manfred KM, Rickards AMJ, Kim J, Reid JP, Orr-Ewing AJ. Comparison of the accuracy of aerosol refractive index measurements from single particle and ensemble techniques. The journal of physical chemistry. A. 2012;116(33):8547–56. doi:10.1021/jp3049668

149. Davies JF, Haddrell AE, Rickards AMJ, Reid JP. Simultaneous analysis of the equilibrium hygroscopicity and water transport kinetics of liquid aerosol. Analytical chemistry. 2013;85(12):5819–26. doi:10.1021/ac4005502

150. Dennis-Smither BJ, Marshall FH, Miles REH, Preston TC, Reid JP. Volatility and Oxidative Ageing of Aqueous Maleic Acid Aerosol Droplets and the Dependence on Relative Humidity. The journal of physical chemistry. A. 2014. doi:10.1021/jp504823j

151. Cotterell MI, Willoughby RE, Bzdek BR, Orr-Ewing AJ, Reid JP. A Complete Parameterization of the Relative Humidity and Wavelength Dependence of the Refractive Index of Hygroscopic Inorganic Aerosol Particles. Atmospheric Chemistry and Physics Discussions. 2017;(April):1–27. doi:10.5194/acp-2017-276

152. Zuend A, Seinfeld JH. A practical method for the calculation of liquid-liquid equilibria in multicomponent organic-water-electrolyte systems using physicochemical constraints. Fluid Phase Equilibria. 2013;337:201–213. doi:10.1016/j.fluid.2012.09.034

153. Ovadnevaite J, Zuend A, Laaksonen A, Sanchez KJ, Roberts G, Ceburnis D, Decesari S, Rinaldi M, Hodas N, Facchini MC, et al. Surface tension prevails over solute effect in organic-influenced cloud droplet activation. Nature. 2017;546(7660):637–641. doi:10.1038/nature22806

154. Zuend A, Seinfeld JH. Modeling the gas-particle partitioning of secondary organic aerosol: The importance of liquid-liquid phase separation. Atmospheric Chemistry and Physics. 2012;12(9):3857–3882. doi:10.5194/acp-12-3857-2012

155. Zuend A, Marcolli C, Booth AM, Lienhard DM, Soonsin V, Krieger UK, Topping DO, McFiggans G, Peter T, Seinfeld JH. New and extended parameterization of the thermodynamic model AIOMFAC: Calculation of activity coefficients for organic-inorganic mixtures containing carboxyl, hydroxyl, carbonyl, ether, ester, alkenyl, alkyl, and aromatic functional groups. Atmospheric Chemistry and Physics. 2011;11(17):9155–9206. doi:10.5194/acp-11-9155-2011

156. Toon OB, Ackerman TP. Algorithms for the calculation of scattering by stratified spheres. Applied Optics. 1981;20(20):3657–3660. doi:10.1364/AO.20.003657

157. Snow JB, Qian SX, Chang RK. Stimulated Raman scattering from individual water and ethanol droplets at morphology-dependent resonances. Optics letters. 1985;10(1):37–39. doi:10.1364/OL.10.000037

158. Popp J, Lankers M, Schaschek K, Kiefer W, Hodges JT. Observation of sudden temperature jumps in optically levitated microdroplets due to morphology-dependent input resonances. Applied optics. 1995;34(13):2380–6. doi:10.1364/AO.34.002380

159. Owen JF, Barber PW, Messinger BJ, Chang RK. Determination of optical-fiber diameter from resonances in the elastic scattering spectrum. Optics Letters. 1981;6(6):272. doi:10.1364/OL.6.000272

160. Ilchenko VS, Savchenkov A a, Matsko AB, Maleki L. Dispersion compensation in whispering gallery modes. J. Opt. Soc. Am. A. 2003;20(1):157–162.

161. Hill SC, Rushforth CK, Benner RE, Conwell PR. Sizing dielectric spheres and cylinders by aligning measured and computed resonance locations: algorithm for multiple orders. Applied Optics. 1985;24(15):2380. doi:10.1364/AO.24.002380

162. Hightower RL, Richardson CB. Resonant Mie scattering from a layered sphere. Applied optics. 1988;27(23):4850–5. doi:10.1364/AO.27.004850

163. Bohren CF, Huffman DR. Absorption and Scattering of Light by Small Particles. Bohren CF, Huffman DR, editors. Weinheim, Germany: Wiley-VCH Verlag GmbH; 1998. doi:10.1002/9783527618156

164. Conwell PR, Rushforth CK, Benner RE, Hill SC. Efficient automated algorithm for the sizing of dielectric microspheres using the resonance spectrum. Journal of the Optical Society of America A. 1984;1(12):1181. doi:10.1364/JOSAA.1.001181

165. Haynes W. M. CRC Handbook of Chemistry and Physics, 97th Edition. 2017.

166. Bilde M, Barsanti K, Booth M, Cappa CD, Donahue NM, Emanuelsson EU, McFiggans G, Krieger UK, Marcolli C, Topping D, et al. Saturation Vapor Pressures and Transition Enthalpies of Low-Volatility Organic Molecules of Atmospheric Relevance: From Dicarboxylic Acids to Complex Mixtures. Chemical Reviews. 2015;115(10):4115–4156. doi:10.1021/cr5005502

167. Clarke AD. Size distributions and mixtures of dust and black carbon aerosol in Asian outflow: Physiochemistry and optical properties. Journal of Geophysical Research. 2004;109(D15S09):1–20. doi:10.1029/2003JD004378

168. Liu Y, Daum PH. Relationship of refractive index to mass density and self-consistency of mixing rules for multicomponent mixtures like ambient aerosols. Journal of Aerosol Science. 2008;39(11):974–986. doi:10.1016/j.jaerosci.2008.06.006

169. Bond TC, Bergstrom RW. Light Absorption by Carbonaceous Particles: An Investigative Review. Aerosol Science and Technology. 2006;40(1):27–67. doi:10.1080/02786820500421521

170. Altaf MB, Freedman MA. Effect of Drying Rate on Aerosol Particle Morphology. The Journal of Physical Chemistry Letters. 2017;8(15):3613–3618. doi:10.1021/acs.jpclett.7b01327

171. Altaf MB, Zuend A, Freedman MA. Role of nucleation mechanism on the size dependent morphology of organic aerosol. Chem. Commun. 2016;52(59):9220–9223. doi:10.1039/C6CC03826C

172. Meresman H, Hudson AJ, Reid JP. Spectroscopic characterization of aqueous microdroplets containing inorganic salts. The Analyst. 2011;136(17):3487–95. doi:10.1039/c0an00843e

173. Davis RD, Lance S, Gordon JA, Ushijima SB, Tolbert MA. Contact efflorescence as a pathway for crystallization of atmospherically relevant particles. Proceedings of the National Academy of Sciences. 2015;112(52):15815–15820. doi:10.1073/pnas.1522860113

174. Presto AA, Donahue NM. Investigation of α-Pinene + Ozone Secondary Organic Aerosol Formation at Low Total Aerosol Mass. Environmental Science & Technology. 2006;40(11):3536–3543. doi:10.1021/es052203z

175. Donahue NM, Robinson AL, Trump ER, Riipinen I, Kroll JH. Volatility and Aging of Atmospheric Organic Aerosol. In: McNeill VF, Ariya PA, editors. Atmospheric and Aerosol Chemistry. Berlin, Heidelberg: Springer Berlin Heidelberg; 2014. p. 97–143. doi:10.1007/128_2012_355

176. Mishchenko MI, Liu L, Mackowski DW. Morphology-dependent resonances of spherical droplets with numerous microscopic inclusions. Optics Letters. 2014;39(6):1701. doi:10.1364/OL.39.001701

177. Voorhees PW. The theory of Ostwald ripening. Journal of Statistical Physics. 1985;38(1–2):231–252. doi:10.1007/BF01017860

178. Nakayama T, Sato K, Matsumi Y, Imamura T, Yamazaki A, Uchiyama A. Wavelength Dependence of Refractive Index of Secondary Organic Aerosols Generated during the Ozonolysis and Photooxidation of alpha-Pinene. Scientific Online Letters on the Atmosphere. 2012;8(0):119–123. doi:10.2151/sola.2012-030

179. Kim H, Liu S, Russell LM, Paulson SE. Dependence of Real Refractive Indices on O:C, H:C and Mass Fragments of Secondary Organic Aerosol Generated from Ozonolysis and Photooxidation of Limonene and α-Pinene. Aerosol Science and Technology. 2014;48(5):498–507. doi:10.1080/02786826.2014.893278

180. Kim H, Barkey B, Paulson SE. Real refractive indices of α- And β-pinene and toluene secondary organic aerosols generated from ozonolysis and photo-oxidation. Journal of Geophysical Research Atmospheres. 2010;115(23):1–10. doi:10.1029/2010JD014549

181. Kim H, Paulson SE. Real refractive indices and volatility of secondary organic aerosol generated from photooxidation and ozonolysis of limonene, alpha-pinene and toluene. Atmospheric Chemistry and Physics. 2013;13(15):7711–7723. doi:10.5194/acp-13-7711-2013

182. Redmond H, Thompson JE. Evaluation of a quantitative structure-property relationship (QSPR) for predicting mid-visible refractive index of secondary organic aerosol (SOA). Physical Chemistry Chemical Physics. 2011;13(15):6872–6882. doi:10.1039/c0cp02270e

183. Wexler AS. Atmospheric aerosol models for systems including the ions H+, NH4+, Na+, SO 4 2-, NO3, Cl- , Br- , and H2O. Journal of Geophysical Research. 2002;107(D14):4207. doi:10.1029/2001JD000451

184. Tröstl J, Chuang WK, Gordon H, Heinritzi M, Yan C, Molteni U, Ahlm L, Frege C, Bianchi F, Wagner R, et al. The role of low-volatility organic compounds in initial particle growth in the atmosphere. Nature. 2016;533(7604):527–531. doi:10.1038/nature18271

185. Dommen J, Metzger A, Duplissy J, Kalberer M, Alfarra MR, Gascho A, Weingartner E, Prevot ASH, Verheggen B, Baltensperger U. Laboratory observation of oligomers in the aerosol from isoprene/NO x photooxidation. Geophysical Research Letters. 2006;33(13):1–5. doi:10.1029/2006GL026523

186. Ray AK, Davis EJ, Ravindran P. Determination of ultra-low vapor pressures by submicron droplet evaporation. The Journal of Chemical Physics. 1979;71(2):582–587. doi:10.1063/1.438408

187. Yli-Juuti T, Pajunoja A, Tikkanen O-P, Buchholz A, Faiola C, V?is?nen O, Hao L, Kari E, Per?kyl? O, Garmash O, et al. Factors controlling the evaporation of secondary organic aerosol from alpha-pinene ozonolysis. Geophysical Research Letters. 2017;44(5):1–9. doi:10.1002/2016GL072364

188. Kampf CJ, Waxman EM, Slowik JG, Dommen J, Pfaffenberger L, Praplan AP, Prévôt ASH, Baltensperger U, Hoffmann T, Volkamer R. Effective Henry's Law Partitioning and the Salting Constant of Glyoxal in Aerosols Containing Sulfate. Environmental Science & Technology. 2013;47(9):4236–4244. doi:10.1021/es400083d

189. EPA U. Estimation Programs Interface Suite™ for Microsoft® Windows. 2012.

190. Kroll JH, Lim CY, Kessler SH, Wilson KR. Heterogeneous Oxidation of Atmospheric Organic Aerosol: Kinetics of Changes to the Amount and Oxidation State of Particle-Phase Organic Carbon. The Journal of Physical Chemistry A. 2015;119(44):10767–10783. doi:10.1021/acs.jpca.5b06946

191. Bateman AP, Nizkorodov S a, Laskin J, Laskin A. High-Resolution Electrospray Ionization Mass Spectrometry Analysis of Water-Soluble Organic Aerosols Collected with a Particle into Liquid Sampler. Analytical Chemistry. 2010;82(19):8010–8016. doi:10.1021/ac1014386

192. Zhang X, Dalleska NF, Huang DD, Bates KH, Sorooshian A, Flagan RC, Seinfeld JH. Time-resolved molecular characterization of organic aerosols by PILS + UPLC/ESI-Q-TOFMS. Atmospheric Environment. 2016;130:180–189. doi:10.1016/j.atmosenv.2015.08.049

193. Xu L, Guo H, Weber RJ, Ng NL. Chemical Characterization of Water-Soluble Organic Aerosol in Contrasting Rural and Urban Environments in the Southeastern United States. Environmental Science & Technology. 2017;51(1):78–88. doi:10.1021/acs.est.6b05002

194. Rothfuss NE, Petters MD. Influence of Functional Groups on the Viscosity of Organic Aerosol. Environmental Science & Technology. 2017;51(1):271–279. doi:10.1021/acs.est.6b04478

195. Herrmann H, Schaefer T, Tilgner A, Styler SA, Weller C, Teich M, Otto T. Tropospheric Aqueous-Phase Chemistry: Kinetics, Mechanisms, and Its Coupling to a Changing Gas Phase. Chemical Reviews. 2015;115(10):4259–4334. doi:10.1021/cr500447k

196. Tsigaridis K, Daskalakis N, Kanakidou M, Adams PJ, Artaxo P, Bahadur R, Balkanski Y, Bauer SE, Bellouin N, Benedetti A, et al. The AeroCom evaluation and intercomparison of organic aerosol in global models. Atmospheric Chemistry and Physics. 2014;14(19):10845–10895. doi:10.5194/acp-14-10845-2014

197. Ye Q, Robinson ES, Ding X, Ye P, Sullivan RC, Donahue NM. Mixing of secondary organic aerosols versus relative humidity. Proceedings of the National Academy of Sciences. 2016;113(45):12649–12654. doi:10.1073/pnas.1604536113

198. Gilardoni S, Massoli P, Paglione M, Giulianelli L, Carbone C, Rinaldi M, Decesari S, Sandrini S, Costabile F, Gobbi GP, et al. Direct observation of aqueous secondary organic aerosol from biomass-burning emissions. Proceedings of the National Academy of Sciences. 2016;113(36):10013–10018. doi:10.1073/pnas.1602212113

199. Gorkowski K, Donahue NM, Sullivan RC. Emulsified and liquid-liquid phase separated states of α-pinene secondary organic aerosol determined using aerosol optical tweezers. Environmental Science & Technology. 2017:in preparation.

200. Davies JF, Miles REH, Haddrell AE, Reid JP. Influence of organic films on the evaporation and condensation of water in aerosol. Proceedings of the National Academy of Sciences of the United States of America. 2013;110(22):8807–12. doi:10.1073/pnas.1305277110

201. Korosi G, Kovats ES. Density and surface tension of 83 organic liquids. Journal of Chemical & Engineering Data. 1981;26(3):323–332. doi:10.1021/je00025a032

202. Girifalco L a., Good RJ. A Theory for the Estimation of Surface and Interfacial Energies. I. Derivation and Application to Interfacial Tension. The Journal of Physical Chemistry. 1957;61(7):904–909. doi:10.1021/j150553a013

203. Shahid MZ, Usman MR, Akram MS, Khawaja SY, Afzal W. Initial Interfacial Tension for Various Organic-Water Systems and Study of the Effect of Solute Concentration and Temperature. Journal of Chemical and Engineering Data. 2017;62(4):1198–1203. doi:10.1021/acs.jced.6b00703

204. Canagaratna MR, Jimenez JL, Kroll JH, Chen Q, Kessler SH, Massoli P, Hildebrandt Ruiz L, Fortner E, Williams LR, Wilson KR, et al. Elemental ratio measurements of organic compounds using aerosol mass spectrometry: Characterization, improved calibration, and implications. Atmospheric Chemistry and Physics. 2015;15(1):253–272. doi:10.5194/acp-15-253-2015

205. Donahue NM, Trump ER, Pierce JR, Riipinen I. Theoretical constraints on pure vapor-pressure driven condensation of organics to ultrafine particles. Geophysical Research Letters. 2011;38(16):3–7. doi:10.1029/2011GL048115

206. Hritz AD, Raymond TM, Dutcher DD. A method for the direct measurement of surface tension of collected atmospherically relevant aerosol particles using atomic force microscopy. Atmospheric Chemistry and Physics. 2016;16(15):9761–9769. doi:10.5194/acp-16-9761-2016

207. Boyer HC, Bzdek BR, Reid JP, Dutcher CS. Statistical Thermodynamic Model for Surface Tension of Organic and Inorganic Aqueous Mixtures. The Journal of Physical Chemistry A. 2017;121(1):198–205. doi:10.1021/acs.jpca.6b10057

208. Boyer HC, Dutcher CS. Atmospheric Aqueous Aerosol Surface Tensions: Isotherm-Based Modeling and Biphasic Microfluidic Measurements. The Journal of Physical Chemistry A. 2017;121(25):4733–4742. doi:10.1021/acs.jpca.7b03189

209. Buades A, Coll B, Morel JM. A Review of Image Denoising Algorithms, with a New One. Multiscale Modeling & Simulation. 2005;4(2):490–530. doi:10.1137/040616024

210. Manjon-Herrera J V. Non-Local Means Filter. MATLAB. 2006 [accessed 2013 Jan 1]. http://www.mathworks.com/matlabcentral/fileexchange/13176-non-local-means-filter

211. Buades A, Coll B, Morel J-M. A Non-Local Algorithm for Image Denoising. Vol. 2. IEEE; 2005. p. 60–65. doi:10.1109/CVPR.2005.38

212. Schiller S. Asymptotic expansion of morphological resonance frequencies in Mie scattering. Applied optics. 1993;32(12):2181–2185. doi:10.1364/AO.32.002181

213. Ray A, Devakottai B, Souyri A, Huckaby J. Evaporation characteristics of droplets coated with immiscible layers of nonvolatile liquids. Langmuir. 1991;7(3):525–531.

214. Ray AK, Tu H. Evaporation dynamics of microdroplets coated with nonvolatile liquid layers. In: Chemical Engineering Transactions. Vol. 32. 2013. p. 1933–1938. doi:10.3303/CET1332323

215. Ray AK, Johnson RD, Souyri A. Dynamic behavior of single glycerol droplets in humid air streams. Langmuir. 1989;5(1):133–140. doi:10.1021/la00085a024